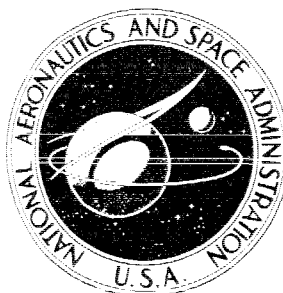


NASA TECHNICAL
MEMORANDUM



NASA TM X-2504

NASA TM X-2504

FLIGHT TEST OF CARBON-PHENOLIC
ON A SPACECRAFT LAUNCHED BY
THE PACEMAKER VEHICLE SYSTEM

by Thomas E. Walton, Jr., and William G. Witte
Langley Research Center
Hampton, Va. 23365

NATIONAL AERONAUTICS AND SPACE ADMINISTRATION • WASHINGTON, D. C. • MARCH 1972

1. Report No. NASA TM X-2504	2. Government Accession No.	3. Recipient's Catalog No.	
4. Title and Subtitle FLIGHT TEST OF CARBON-PHENOLIC ON A SPACECRAFT LAUNCHED BY THE PACEMAKER VEHICLE SYSTEM		5. Report Date March 1972	
		6. Performing Organization Code	
7. Author(s) Thomas E. Walton, Jr., and William G. Witte		8. Performing Organization Report No. L-8098	
		10. Work Unit No. 117-07-04-02	
9. Performing Organization Name and Address NASA Langley Research Center Hampton, Va. 23365		11. Contract or Grant No.	
		13. Type of Report and Period Covered Technical Memorandum	
12. Sponsoring Agency Name and Address National Aeronautics and Space Administration Washington, D.C. 20546		14. Sponsoring Agency Code	
15. Supplementary Notes			
16. Abstract <p>Carbon-phenolic material consisting of 50 percent carbon fibers and 50 percent phenolic resin was flight tested on a recoverable spacecraft launched by the Pacemaker vehicle system. The heat shield of the spacecraft was fabricated so that the carbon fibers in the ablator material had different orientations over several areas of the spacecraft. The environment in which the spacecraft was tested produced heating rates on the hemispherical nose up to 13.6 MW/m^2 ($1200 \text{ Btu/ft}^2\text{-sec}$) and stagnation-point pressures up to 1.27 MN/m^2 (12.5 atm). The experimental results are presented. Due to high heating rates and possible spallation and mechanical char removal the greatest mass loss occurred in the nose region. Essentially uniform surface recession and char thickness were observed on the conical section of the spacecraft.</p> <p>A comparison of measured heating rates with computed turbulent and laminar heating rates, as well as measurements of sound-pressure fluctuations in the boundary layer obtained with acoustic sensors, indicated that the boundary layer underwent transition. The acoustic sensor provides an interesting new data form for the general study of boundary-layer transition for free-flight investigations.</p>			
17. Key Words (Suggested by Author(s)) Ablation performance Carbon-phenolic		18. Distribution Statement Unclassified - Unlimited	
19. Security Classif. (of this report) Unclassified	20. Security Classif. (of this page) Unclassified	21. No. of Pages 87	22. Price* \$3.00

FLIGHT TEST OF CARBON-PHENOLIC ON A SPACECRAFT LAUNCHED BY THE PACEMAKER VEHICLE SYSTEM

By Thomas E. Walton, Jr., and William G. Witte
Langley Research Center

SUMMARY

Carbon-phenolic material consisting of 50 percent carbon fibers and 50 percent phenolic resin was flight tested on a recoverable spacecraft launched by the Pacemaker vehicle system. The heat shield of the spacecraft was fabricated so that the carbon fibers in the ablator material had different orientations over several areas of the spacecraft. The environment in which the spacecraft was tested produced heating rates on the hemispherical nose up to 13.6 MW/m^2 ($1200 \text{ Btu/ft}^2\text{-sec}$) and stagnation-point pressures up to 1.27 MN/m^2 (12.5 atm). The experimental results are presented. Due to high heating rates and possible spallation and mechanical char removal the greatest mass loss occurred in the nose region. Essentially uniform surface recession and char thickness were observed on the conical section of the spacecraft.

A comparison of measured heating rates with computed turbulent and laminar heating rates, as well as measurements of sound-pressure fluctuations in the boundary layer obtained with acoustic sensors, indicated that the boundary layer underwent transition. The acoustic sensor provides an interesting new data form for the general study of boundary-layer transition for free-flight investigations.

INTRODUCTION

At present, there is a great interest in developing heat-shield materials which are capable of withstanding the environment produced by velocities which would be encountered on return from an interplanetary mission. Carbon-phenolic appears to be one of the more promising ablative materials for this application since it is capable of forming and retaining a high-strength, high-temperature char layer. Retaining a high-temperature char layer contributes to the efficiency of a heat shield by: (1) reradiating large quantities of heat, (2) reducing the convective heat transfer by lowering the temperature difference across the boundary layer, (3) maintaining a nearly constant geometry, and (4) in very high heating environments, subliming and thereby absorbing additional heat. These characteristics suggest that carbon-phenolic is an attractive ablative material for missions of high heating and high aerodynamic shear flow.

Carbon-phenolic has been the subject of several studies conducted in ground test facilities (e.g., refs. 1 and 2). As a result of considerable interest in obtaining flight data on this material, the present flight test (one in a series of materials technology experiments) was conducted. The spacecraft containing the experiment was launched by a Pacemaker vehicle from NASA Wallops Station. At the end of the flight the spacecraft was recovered from the ocean.

The primary purpose of the test was to obtain ablation performance data on the carbon-phenolic material. The heat shield was fabricated with carbon-phenolic material having different fiber-plane orientations over several areas of the spacecraft in order to detect a preferred fiber-plane orientation, if such exists for these test conditions. Recession and temperature measurements obtained from the experiment are presented herein. The recession measurements were obtained with radioactive ablation sensors and by post-flight profile-change measurements.

In addition to these ablation measurements, the spacecraft was instrumented to measure boundary-layer transition. This was accomplished with acoustic sensors and thin-foil calorimeters. The measurements obtained from these instruments are presented. Also, comparisons are made between measured and predicted heating rates.

SYMBOLS

Values are given in both SI and U.S. Customary Units. The measurements and calculations were made in U.S. Customary Units.

M_∞	free-stream Mach number
p_e	local surface pressure, N/m^2 (lb/ft ²)
p_{SL}	standard pressure at sea level, N/m^2 (lb/ft ²)
$p_{t,2}$	total pressure behind a normal shock, N/m^2 (lb/ft ²)
r_n	nose radius, cm (in.)
s	distance along surface measured from stagnation point, cm (in.)
ρ_{SL}	standard density at sea level, kg/m^3 (slugs/ft ³)
θ	circumferential station, deg

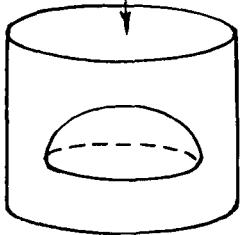
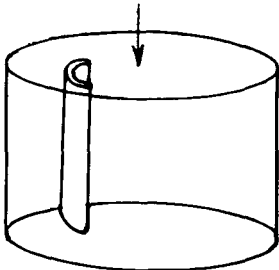
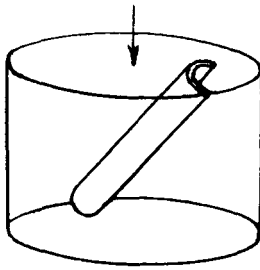
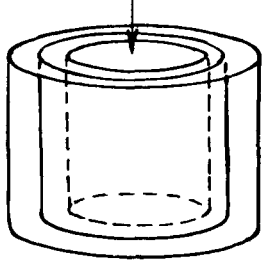
SPACECRAFT

The spacecraft, which consisted of heat-shield materials bonded to a primary substructure, was similar to previous Pacemaker spacecraft (ref. 3). Figure 1 shows a sketch of the spacecraft heat shield. It was a hemispherically blunted cone with a cylindrical afterbody. The forward portions of the heat shield were made of carbon-phenolic. The aft cylindrical portions were made of low-density ablators bonded to a layer of cork. These ablators are not discussed in this paper. The overall dimensions of the spacecraft were a length of 83.19 cm (32.75 in.) and a diameter of 25.4 cm (10.0 in.). The initial nose radius was 6.35 cm (2.5 in.) and the half-angle of the cone was 12.5° . Cylindrical sections aft of the spacecraft housed a recovery parachute and the spacecraft telemetry.

The carbon-phenolic material had a specific gravity of 1.38. It consisted of equal parts by weight of carbon fibers approximately 0.63 cm (0.25 in.) long and phenolic resin. The material was molded at the Langley Research Center into cylindrical billets 30.48 cm (12.0 in.) in diameter and 15.24 cm (6.0 in.) thick. Upon molding, the carbon fibers in the billets lay in planes perpendicular to the applied molding force, but randomly oriented within these planes. The carbon-phenolic parts of the heat shield consisted of 10 separate pieces machined from these billets. Figure 2 shows the pieces of the heat shield and notes the fiber-plane orientation of each one. Table I shows the locations of the pieces in the molded billets before machining. The pieces were machined in this manner to obtain the desired fiber-plane orientation in the different areas of the spacecraft. On the hemispherical nose, the fiber planes ranged from parallel to the surface at the stagnation point to 77.5° at the hemisphere-cone tangent point. The fiber-plane orientation on two opposed quadrants of the conical section was normal to the surface and on the other two remaining quadrants the fiber planes were swept backwards 45° to the surface. The fiber planes in the cylindrical section were oriented normal to the surface around the entire periphery. The size of the molded billets required the conical quadrants to be machined in two pieces rather than in one piece.

Photographs of the spacecraft are shown in figure 3. The assembled spacecraft before flight is shown in figure 3(a). The nine pieces of carbon-phenolic on the cone and hemisphere were hard bonded to the primary substructure with a supported film epoxy-phenolic adhesive. The bond line was roughly 0.254 mm (0.010 in.) thick. At the junctures between the hemisphere and the cone, and between the forward cone quadrants and the aft cone quadrants, additional support for the pieces was obtained by two embedded mild steel circular rings, 0.159 by 0.635 cm (0.0625 by 0.25 in.) in cross section, keyed to grooves machined into the interface surfaces between these pieces (see fig. 3(b)). Similarly, the cone quadrants were reinforced longitudinally by straight splines of mild steel embedded into grooves machined into the interface surfaces along the longitudinal seams

TABLE I. - FIBER-PLANE ORIENTATION^a

Part	Fiber-plane orientation	Location of part in billet
Nose cap	Varies from parallel to surface at stagnation point to 77.5° to the surface at hemisphere-cone tangent point	
Cone	Perpendicular to surface	
Cone	45° to surface	
Cylinder	Perpendicular to surface	

^a The carbon fibers lie in planes perpendicular to the axis of rotation of the cylindrical billets but are randomly oriented within these planes.

of the cone. The interface surfaces of these nine pieces were bonded with an elastomeric silicone rubber adhesive. Also, the cylindrical piece of carbon-phenolic was bonded to the primary substructure with an elastomeric silicone rubber adhesive.

INSTRUMENTATION

The instrumentation located in the carbon-phenolic heat shield consisted of the following: two 7-element radioactive ablation sensors, 14 surface thermocouples, six 3-element in-depth thermocouple assemblies, one 2-element in-depth thermocouple assembly, three acoustic sensors, and three calorimeters. Figure 4 shows the stations where instrumentation was located. Table II presents the locations on the spacecraft of the sensors and their sensing depths.

The radioactive ablation sensors (ref. 4) consisted of seven minute particles of radioactive material (tantalum 182) encapsulated in pyrolytic-carbon sleeves and then embedded in removable carbon-phenolic plugs, as shown in figure 5. These particles of tantalum 182 were in the form of wires 0.1270 mm (0.005 in.) in diameter by 0.381 to 2.54 mm (0.015 to 0.100 in.) long. Tapered plugs, machined from commercially available high-density graphite, were forced into the ends of the pyrolytic-carbon sleeve, and any excess removed. As the carbon-phenolic heat shield receded due to ablation and the radioactive particles were removed, sensing instrumentation, located within the spacecraft, monitored the loss of the minute particles and indicated the location of the heat-shield surface. The sensing instrumentation included two Geiger-Muller tubes. These tubes were protected with shielding material so that each tube monitored only one plug.

The surface thermocouples were a ribbon type similar to the thermocouples described in references 3 and 5. The in-depth thermocouples were a wire type. Figure 6 is a sketch of a typical 3-element in-depth thermocouple assembly. Thermocouples constructed of various materials were available. The selections made were based on the expected maximum temperature at the thermocouple location. Tungsten and tungsten with 26 percent rhenium, suitable for temperatures up to 3031 K (5000° F), were selected for the surface thermocouples on the hemispherical nose and cone. Platinum and platinum with 13 percent rhodium, suitable for temperatures up to 1922 K (3000° F), were selected for the surface thermocouples on the cylinder. The three kinds of in-depth thermocouples selected were: tungsten with 5 percent rhenium and tungsten with 26 percent rhenium for expected maximum temperature over 1366 K (2000° F); chromel and alumel for 811 K to 1366 K (1000° F to 2000° F); and chromel and constantan for up to 811 K (1000° F).

The acoustic sensor (ref. 6) consisted of a small crystal microphone located within the spacecraft and communicating with the spacecraft boundary layer via a small-diameter port. The acoustic sensor array on the spacecraft was designed to measure the location

TABLE II - SENSOR LOCATIONS

Sensor type	Number	Station		Sensing depth		Fiber-plane orientation (a)
		Axial	Circumferential	cm	in.	
Radioactive ↓	R1-1	0°	0°	0.038	0.015	0°
	R1-2	↓	↓	.089	.035	↓
	R1-3			.152	.060	
	R1-4			.216	.085	
	R1-5			.292	.115	
	R1-6			.368	.145	
	R1-7	↓	↓	.457	.180	↓
	R2-1	45°	0°	0.076	0.030	45°
	R2-2	↓	↓	.178	.070	↓
	R2-3			.305	.120	
	R2-4			.445	.175	
	R2-5			.559	.220	
	R2-6	↓	↓	.673	.265	↓
	R2-7			.851	.335	
Surface thermocouple ↓	N1	45°	90°	0.0	0.0	45°
	N2	67.5°	270°	↓	↓	67.5°
	N3	B-B	30°			90°
	N4	↓	120°			45°
	N5		210°			90°
	N6	↓	300°			45°
	N7	D-D	75°			45°
	N8	↓	165°			90°
	N9		255°			45°
	N10	↓	345°			90°
	N11	F-F	55°			↓
	N12	↓	125°			
	N13		235°			
	N14	↓	305°			
In-depth thermocouple ↓	P1-1	0°	0°	0.381	0.150	0°
	P1-2	↓	↓	.635	.250	↓
	P1-3			1.016	.400	
	P2-1	45°	180°	0.508	0.200	45°
	P2-2	↓	↓	.762	.300	↓
	P2-3			1.016	.400	
	P3-1	C-C	22.5°	0.025	0.010	90°
	P3-2	↓	↓	.356	.140	↓
	P3-3			.711	.280	
	P4-1		112.5°	0.025	0.010	45°
	P4-2		↓	.356	.140	↓
	P4-3			.711	.280	
	P5-1		202.5°	0.178	0.070	90°
	P5-2		↓	.533	.210	↓
	P5-3			.889	.350	
	P6-1		292.5°	0.178	0.070	45°
	P6-2		↓	.533	.210	↓
	P6-3			.889	.350	
	P7-1	E-E	275°	0.127	0.050	90°
	P7-2	E-E	275°	.254	.100	90°
Acoustic ↓	A1	B-B	80°			
	A2	D-D	100°			
	A3	F-F	265°			
Calorimeter ↓	C1	B-B	260°	0.025	0.010	
	C2	D-D	280°	.025	.010	
	C3	F-F	85°	.000	.000	

^a Fiber-plane orientation is with respect to the local surface.

and level of the boundary-layer sound-pressure fluctuation. Boundary-layer flow transition from laminar to turbulent is accompanied by a sudden increase in the boundary-layer sound-pressure fluctuations. Reference 7 illustrates transition detection by use of this type of instrument.

The calorimeters were of the thin-foil type described in references 3 and 8.

A standard 12-channel Inter-Range Instrumentation Group (IRIG) FM/FM telemetry system transmitted the following data: recession, temperature, heating rate, boundary-layer noise, and spacecraft accelerations. The thermocouple and calorimeter data were commutated. Calorimeter C1 data were continuous, also, in order to compare continuous and commutated data. All the other data were continuous.

LAUNCH VEHICLE AND OPERATIONS

The Pacemaker launch vehicle and spacecraft in launch position are shown in figure 7. The vehicle was launched July 10, 1969, from the NASA Wallops Station launch facility. It was launched at a nominal elevation angle of 70° on an azimuth of 135° with impact and recovery 104 km (56 n. mi.) from Wallops Island.

The propulsion system of the Pacemaker launch vehicle consisted of four stages of solid-propellant rocket motors: Honest John, Nike, TX-77, and Recruit. The first and second stages were ignited during vehicle ascent. The third and fourth stages were ignited during vehicle descent. In other details of the launch and recovery, the flight was similar to that described in reference 3.

A plot of the trajectory and the sequence of events are shown in figure 8. The variations of flight velocity and altitude during the data period are shown in figure 9. These trajectory data were obtained from the AN/FPQ-6 tracking radar. Telemetered normal and transverse accelerometer data showed no abnormal body motions during the data period. The total angle of attack during the data period was less than 2.5° . The roll rate at third-stage burnout, obtained from a gyro, was 86.1 deg/sec. After the data period the spacecraft with fourth stage attached coasted to an altitude of 3048 m (10 000 ft). At this altitude (Time = 148 sec) the fourth stage was separated from the spacecraft by a pyrotechnic device initiated by a barometric switch. A parachute was deployed and the spacecraft was lowered to the water at a velocity of about 18.3 m/sec (60 ft/sec).

TEST ENVIRONMENT

A rawinsonde launched just prior to flight measured ambient pressure and temperature. Nondimensionalized values of pressure and computed ambient density as functions of altitude are shown in figure 10(a). Figure 10(b) shows the temperature variation with altitude.

Computed pressure distributions over the initial spacecraft configuration are shown in figure 11 for several free-stream Mach numbers. The distributions for the hemisphere and cone were obtained from reference 9, and the distribution for the cylinder was obtained by a flow-field solution using the method of characteristics (ref. 10).

Computed histories of heating rate, pressure, shear stress, and Reynolds number based on wetted distance from the stagnation point for several stations on the spacecraft are presented in figures 12 to 15. All computations were made by utilizing the methods described in reference 11. The heating rates for locations away from the stagnation point were calculated by Eckert's reference-enthalpy method where a local enthalpy and local pressure were used to determine all other reference thermodynamic properties. The local heat-transfer coefficients as functions of a skin-friction factor were calculated by using Reynolds' analogy and a Stanton number based on the enthalpy difference. The turbulent incompressible skin-friction factor was given by the Schultz-Grunow relationship. Turbulent aerodynamic shears were obtained by use of incompressible skin-friction coefficients obtained from flow properties at reference conditions.

RESULTS AND DISCUSSION

Spacecraft Appearance

Photographs of the recovered spacecraft are shown in figure 16. As can be seen in these photographs the contours of the spacecraft surface were somewhat irregular. In several areas of the spacecraft, splitting of the heat shield occurred along planes parallel to the carbon-fiber-plane orientation. The most severe split was observed at about the 70° station on the hemispherical nose and can be seen in figure 16(b). Indentations or pitting and other surface irregularities occur only on the hemispherical nose. These irregularities are possibly due to spallation or mechanical char removal.

On the hemispherical nose, where surface recession occurred to the greatest extent, ribbons from the surface thermocouples and wires from the in-depth thermocouples were protruding from the surface. Some of these protrusions can be seen in the closeup photograph of figure 16(c). Also, note in figure 16(c) that the radioactive ablation sensor plug at the stagnation point is missing.

Surface-Recession Results

Figure 17 shows the histories of surface recession obtained from the radioactive ablation sensors at the stagnation point and at the 45° station on the hemisphere. The data at the stagnation point indicate that the missing plug noted in figure 16(c) was in place during the data period. It is possible that the plug was shaken loose from the spacecraft at the time of parachute deployment.

In addition to the radioactive-ablation-sensor data, preflight and postflight measurements of the spacecraft contour were made by means of a dial gage and measuring fixture described in reference 12. From these measurements the final postflight heat-shield surface position relative to the preflight surface position was determined. The differences between these measurements are presented in figure 18 as a surface recession or expansion. Measurements were made for several longitudinal locations at 30° intervals circumferentially. Essentially uniform surface recession and char thickness were observed on the conical section of the spacecraft. In figure 18(b) several points indicate expansion of the heat shield. Expansion can be caused by either swelling of the heat-shield material with no appreciable material removal, or by separating and raising of the heat shield from the substructure. Separation of the heat shield was not evident. However swelling or expanding of this material is possible under certain test conditions. In reference 2 over the entire range of those test conditions, there was a measurable expansion of the material which offset recession. An attempt, by the author of reference 2, to correlate the expansion with various parameters was unsuccessful.

Thermocouple Results

Experimental temperature histories of the surface and in-depth thermocouples are presented in figures 19 and 20, respectively. Hand faired plots of these temperature histories are presented in figures 21 and 22 for the surface and in-depth thermocouples, respectively.

As pointed out in reference 5, the design of the surface thermocouples is such that serious errors in the measured temperatures due to conduction of heat along the leads can occur and no method for providing a temperature correction was devised. Furthermore, the thermocouples at the 45° and 67½° stations did not recede with the ablating heat-shield surface and therefore protruded above the surface into the boundary layer, probably producing unknown effects on the measured temperatures obtained at these stations.

A malfunctioning of three surface thermocouples (N7, N11, and N13) occurred during the flight. Both N11 and N13 malfunctioned at the beginning of the data period and as a result are not shown. The temperature reading from N7 became erratic at roughly 77 sec. Therefore, in figure 21(c) N7 is not plotted beyond this time.

A number of the in-depth thermocouples malfunctioned during the data period. The heat-shield surface receded past the hot junctures of the two outermost thermocouples at the stagnation point (P1-1 and P1-2) and of all three thermocouples at the 45° station (P2-1, P2-2, and P2-3). The hot junctures of the thermocouples were destroyed upon being exposed to the hot airstream in the boundary layer. Consequently, no measurements are available beyond the exposure times. See figures 22(a) and 22(b). Thermo-

couples P1-3 and P5-2 went out of order during the data period even though they were not exposed to the boundary layer. It is possible that the expansion of the char layer broke the thermocouple junctures or lead wires.

Calorimeter Results

The measured heating-rate histories at two locations on the conical section (forward and aft) and one location on the cylindrical section of the spacecraft are presented in figure 23. Initially the heating rates increased until 75.7 sec when maximum heating rates for all three locations occur. Beyond this point the heating rates gradually decline, with the exception of a brief rise at about 80 sec at calorimeter C1. These data are compared with heating-rate calculations and the differences between the two are pointed out subsequently.

Acoustic-Sensor Results

Sound-pressure fluctuations in the boundary layer, obtained from the acoustic sensors, are qualitatively shown in figure 24. These sensors were located at the same axial locations as the calorimeters but rotated 180° around the periphery of the spacecraft (see table II for exact locations of the sensors). The thrust acceleration of the spacecraft is shown in the figure also, as a time reference.

A determination of the range of sound-pressure fluctuations in the boundary layer was made by the methods described in reference 6 so that the sensitivity of each instrument could be set. The most sensitive system, A1, was located at the forward cone station. It exhibits some high-amplitude sound-pressure fluctuations starting about half-way into the coast period after second-stage burnout (about 44 sec) and continuing up to 66.75 sec. These high-amplitude pressure fluctuations can be attributed to unsteady flow over the spacecraft during this transonic period of the flight and should not be construed as boundary-layer transition. The next instrument, A2, located at the rearward cone station, was set to be less sensitive than A1. The least sensitive system, A3, was located on the cylindrical section.

Figure 24 also shows the rocket motor starting shocks at the third- and fourth-stage ignitions. The third-stage motor-starting shock at 66 sec shows a high-amplitude response of the three acoustic sensors, and A2 and A3 clearly illustrate rapid damping. Fine frequency details of these signals, not apparent in figure 24, show characteristic low frequencies in the damping wave, presumably related to spacecraft structural vibrations induced by the starting shock and burning. Similar low frequencies also exist in the A1-sensor data, although partially obscured by high acoustic levels from other sources at that time. Similar low-frequency damping signals can be seen for a half second or so after fourth-stage motor ignition. It is noteworthy that these sensors were not disabled

or grossly affected by rocket-motor burning, and operated essentially normally after recovery from the ignition-starting shock, although there is a minor increase in sensor-output signal level during burning.

It is also of interest to note that the total spacecraft velocity became subsonic during the latter part of the upward coasting portion of the flight, after second-stage motor burnout, prior to third-stage ignition. Then, shortly after third-stage thrust buildup, the vehicle velocity again became supersonic. Figure 24 shows a pronounced decrease in acoustic-sensor signal level about a half second after third-stage thrust buildup. Presumably, this sensor signal-level decrease is indicative of flow transition from subsonic to supersonic associated with increasing velocity.

Also in figure 24, at about 67.25 sec the acoustic-sensor data are marked, apparently by the occurrence of a chug during third-stage motor ignition.

Except for sensor A3, the acoustic-sensors signal levels remained essentially as seen after 74 sec for the duration of the data transmission portion of the flight. The signal from sensor A3 continued to build after 77 sec achieving a final level about twice that shown in figure 24.

Heat Transfer and Boundary-Layer Transition Results

Comparisons of calorimeter and predicted heating rates.- The calorimeter heating rates of figure 23 are reshowed in figure 25. Also, the predicted laminar and turbulent heating rates computed by the methods in reference 11 have been superimposed on the figure for comparison. Choosing as the time of transition the first sharp deviation of the calorimeter trace above the calculated laminar heating rate, the time of transition for the three calorimeters C1, C2, and C3 observed from figure 25 are 71.25, 70.25, and 70.0 sec, respectively.

There are several unexpected variations in the measured heating rates. The most pronounced difference between the measurements and predicted turbulent values occurs at 79 sec for calorimeter C1 (station B-B). At this time, the measured heating rate is 30 percent less than theory, and then for 2 sec the heating rate increases, whereas the calculated values and the other measured values at C2 and C3 decrease steadily from the peak condition. There is good agreement between the measured and computed peak values at stations B-B and D-D. However, at station F-F the measured peak value is 20 percent less than the calculated one.

Comparisons of calorimeter data and acoustic-sensor data.- A comparison between the calorimeter measurements and the acoustic measurements is presented in the following table:

Sensor	Time of transition, sec	Sensor	Time of transition, sec
C1	71.25	A1	70.49
C2	70.25	A2	70.34
C3	70.00	A3	69.95

Although there is a favorable comparison between the times of transition for the two systems, it should be pointed out that the respective systems (C1 and A1, C2 and A2, and C3 and A3) are not located adjacent to each other but are rotated 180° around the spacecraft from each other. It should be recognized that transition may not occur at the same axial station on opposite sides of the spacecraft at the same time.

Results from the acoustic sensors do not agree with the results from the calorimeter data. In general, the acoustic data lead the calorimeter data and by larger intervals at higher heating rates, or at more forward locations. An explanation for this disagreement is the much faster response time of the acoustic sensors as compared to the calorimeter sensors. The acoustic sensors have the capability of responding to rapidly fluctuating, intermittent, and unsteady flow conditions, even during developing transitional flow conditions. There are several such signal signatures in the acoustic data of figure 24. Calorimeters, or other heat-sensing, flow-measuring devices would, in general, not be capable of identifying such intermittent flow conditions, due to their inherently much slower response time.

During the flight test the local Mach number along the cone and cylinder was roughly 3. As shown in reference 13, the approximate range of transition Reynolds number based on wetted length for this local Mach number is 1.5×10^6 to 5×10^6 . The computed Reynolds numbers at the above indicated times of transition are 0.6×10^6 and 1.3×10^6 on the cone and 1.5×10^6 on the cylinder. These values were obtained using the computed pressure distributions shown in figure 11 and the computed values of local surface pressure shown in figure 13. Transition occurred at lower Reynolds numbers on the spacecraft than indicated in reference 13, possibly due to surface roughness and mass transfer.

CONCLUDING REMARKS

Carbon-phenolic material was flight tested on a recoverable spacecraft launched by the Pacemaker vehicle system. The experimental results are presented. Due to high heating rates and possible spallation and mechanical char removal the greatest mass loss occurred in the nose region. Essentially uniform surface recession and char thickness were observed on the conical section of the spacecraft.

A comparison of measured heating rates with computed turbulent and laminar heating rates, as well as measurements of sound-pressure fluctuations in the boundary layer obtained with acoustic sensors, indicated that the boundary layer underwent transition. The acoustic sensor provides an interesting new data form for the general study of boundary-layer transition for free-flight investigations.

Langley Research Center,
National Aeronautics and Space Administration,
Hampton, Va., February 8, 1972.

REFERENCES

1. O'Hare, Brian J.: An Analysis of the Spallation of Carbon Phenolic Ablators. M.S. Thesis, Virginia Polytech. Inst., June 1967.
2. Sutton, Kenneth: An Experimental Study of Carbon-Phenolic Ablation Material. NASA TN D-5930, 1970.
3. Witte, William G.: Flight Test of High-Density Phenolic-Nylon on a Spacecraft Launched by the Pacemaker Vehicle System. NASA TM X-1910, 1969.
4. Chase, George T.; and Galbiati, Louis J.: Ablation Rate Measurement by Means of a Radioactive Tracer Technique. Preprint No. 17.18-4-65, Instrum. Soc. Amer., Oct. 1965.
5. Witte, William G.: Analysis of the Thermal Response of High-Density Phenolic-Nylon on a Spacecraft Launched by the Pacemaker Vehicle System. NASA TN D-6293, 1971.
6. Blanchard, Byron E.; Johnson, David E.; Kleinschmidt, Klaus; and Starr, Edward A.: Fabrication and Testing of Acoustic Sensors for Boundary Layer Flow Transition Detection. Rep. No. 1816 (Contract No. NAS 1-8472), Bolt Beranek and Newman, Inc., Aug. 1969. (Available as NASA CR-66 801.)
7. Trimble, W. J.; Quint, P. B.; and Wilson, R. W.: Endoatmospheric Decoy Technology Program Postflight Data Report - Payload D-4 White Sands Missile Range. AVSD-0278-69-CR, July 16, 1969.
8. Malone, Erle W.: Design and Calibration of Thin Foil Heat Flux Sensors. Preprint No. P6-2-PHYMMID-67, Instrum. Soc. Amer., 1967.
9. Arnold, John W.; Simmons, Harmon L.; and Miller, William T.: An Investigation of the Aerodynamic Characteristics of a 25° Sphere-Cone Including a Pressure Distribution Analysis at Angles of Attack, and a Trajectory Analysis During a Typical Reentry Trajectory. Rep. No. NASA CR-66037, LTV Aerospace Corp., [1966].
10. Lomax, Harvard; and Inouye, Mamoru: Numerical Analysis of Flow Properties About Blunt Bodies Moving at Supersonic Speeds in an Equilibrium Gas. NASA TR R-204, 1964.
11. Graves, Randolph A., Jr.; and Witte, William G.: Flight-Test Analysis of Apollo Heat-Shield Material Using the Pacemaker Vehicle System. NASA TN D-4713, 1968.
12. Walton, Thomas E., Jr.; Witte, William G.; and O'Hare, Brian J.: Flight Investigation of the Effects of Apollo Heat-Shield Singularities on Ablator Performance. NASA TN D-4791, 1968.
13. Sherman, M. M.: Entry Gasdynamic Heating. NASA SP-8062, 1971.

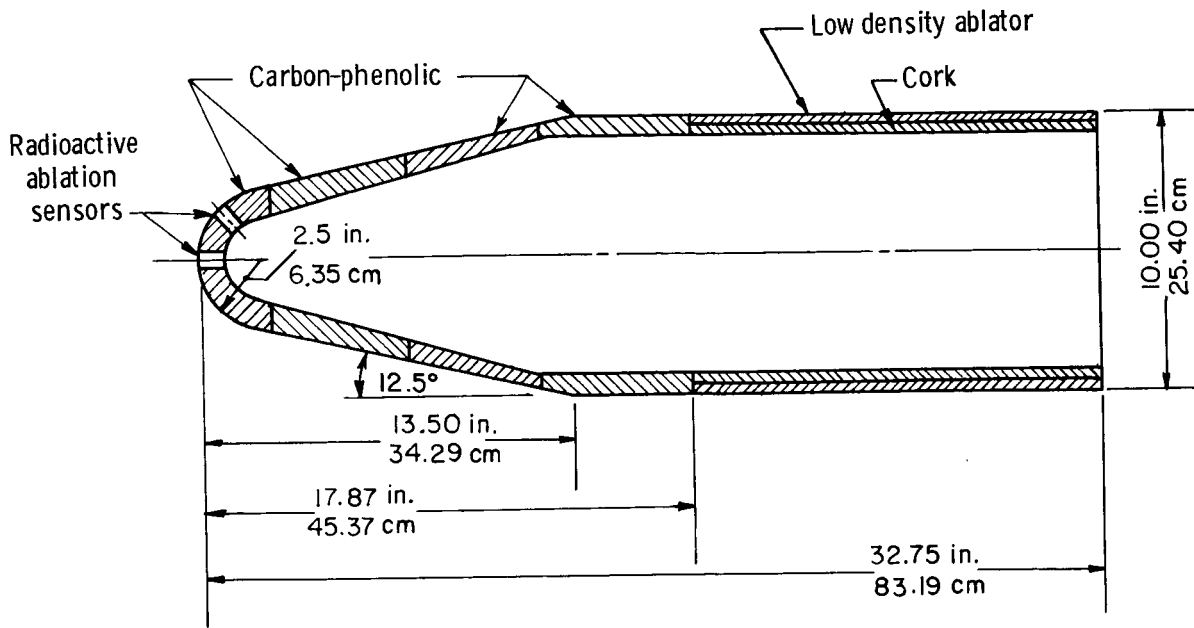


Figure 1. - Sketch of spacecraft heat shield.

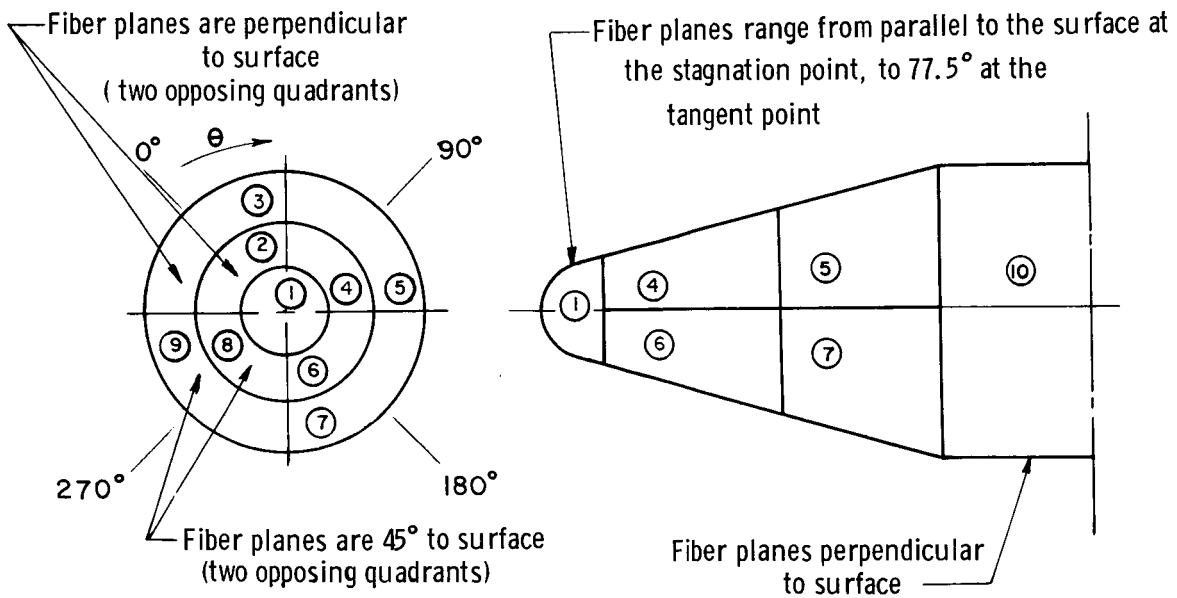
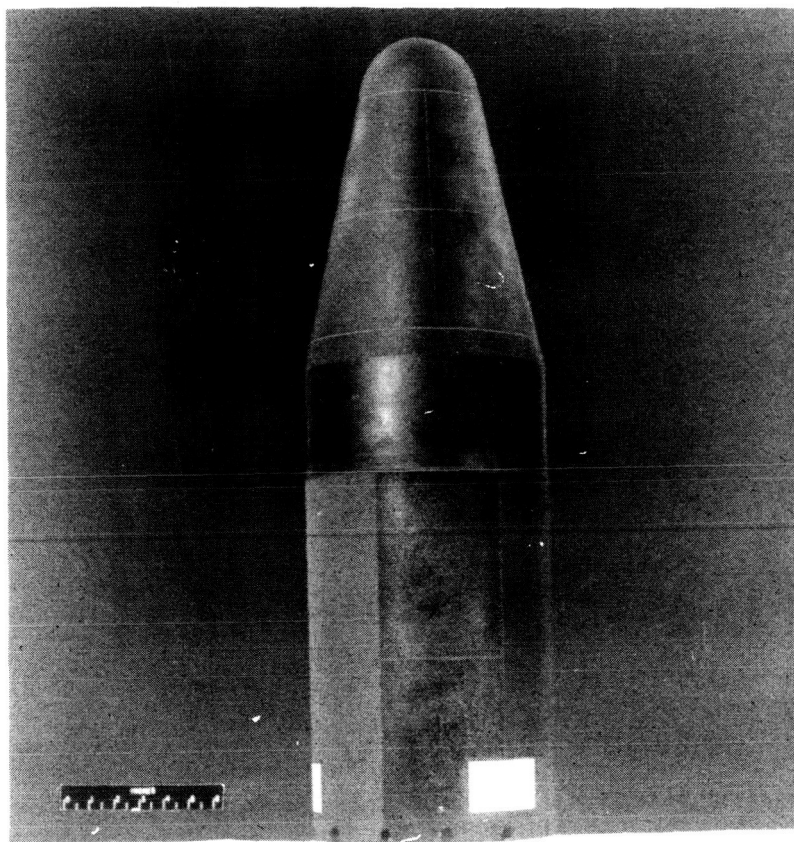


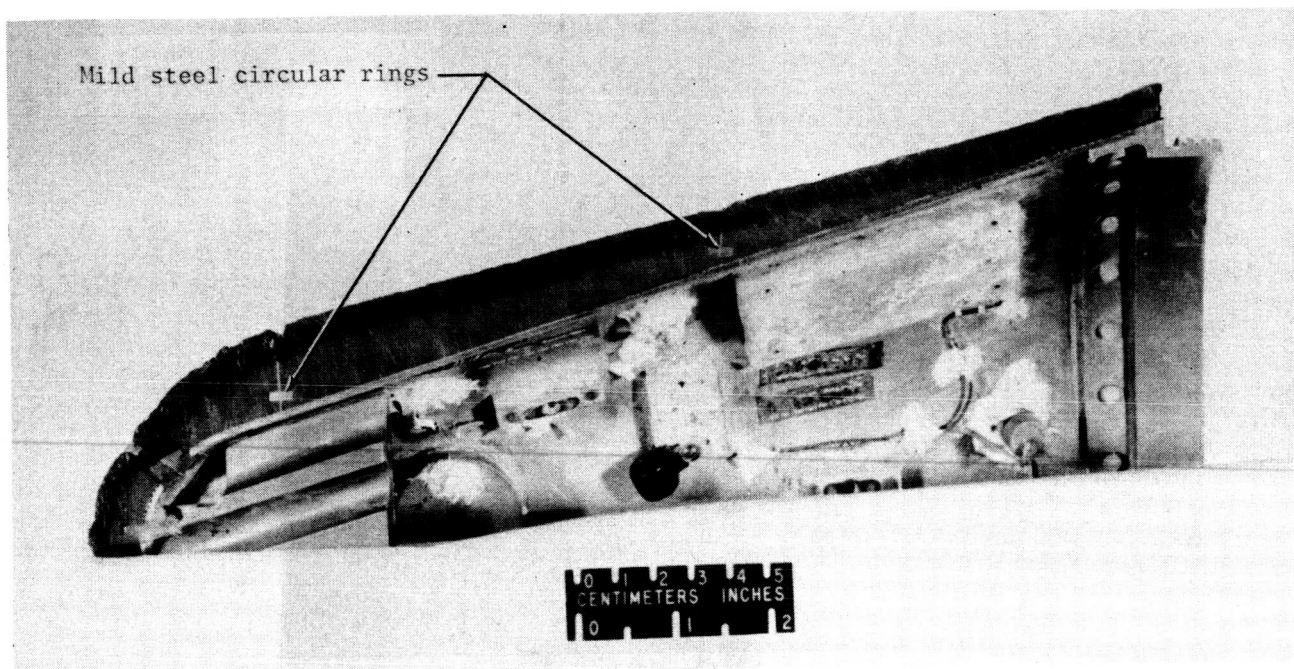
Figure 2. - Sketch showing 10 pieces which make up heat shield and fiber-plane orientation of each.



L-69-3495

(a) Spacecraft before flight.

Figure 3.- Photographs of the spacecraft.



L-70-1299.1

(b) Cross section of the recovered hemispherical nose cone.

Figure 3.- Concluded.

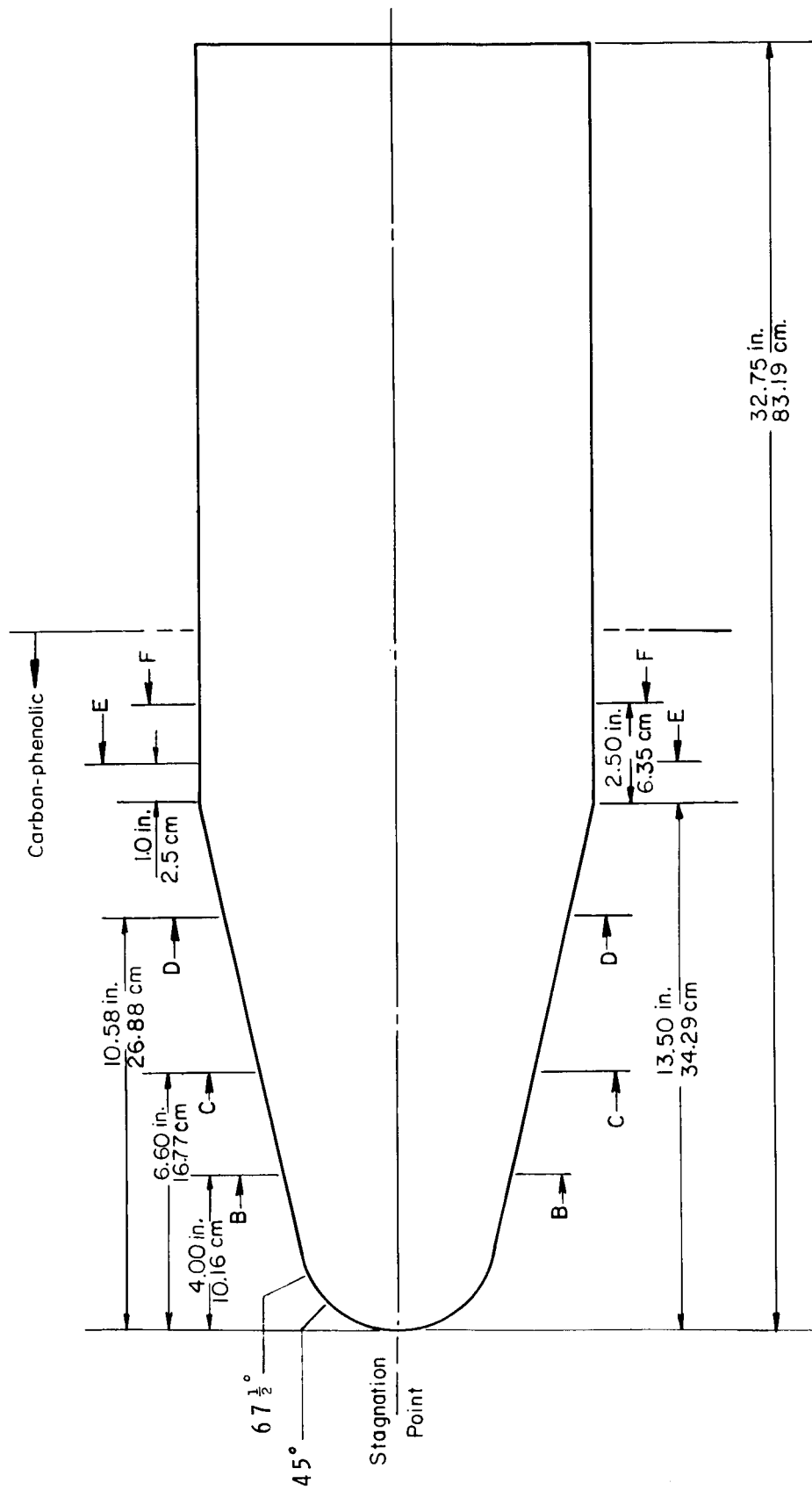


Figure 4. - Sketch showing stations where instrumentation is located.

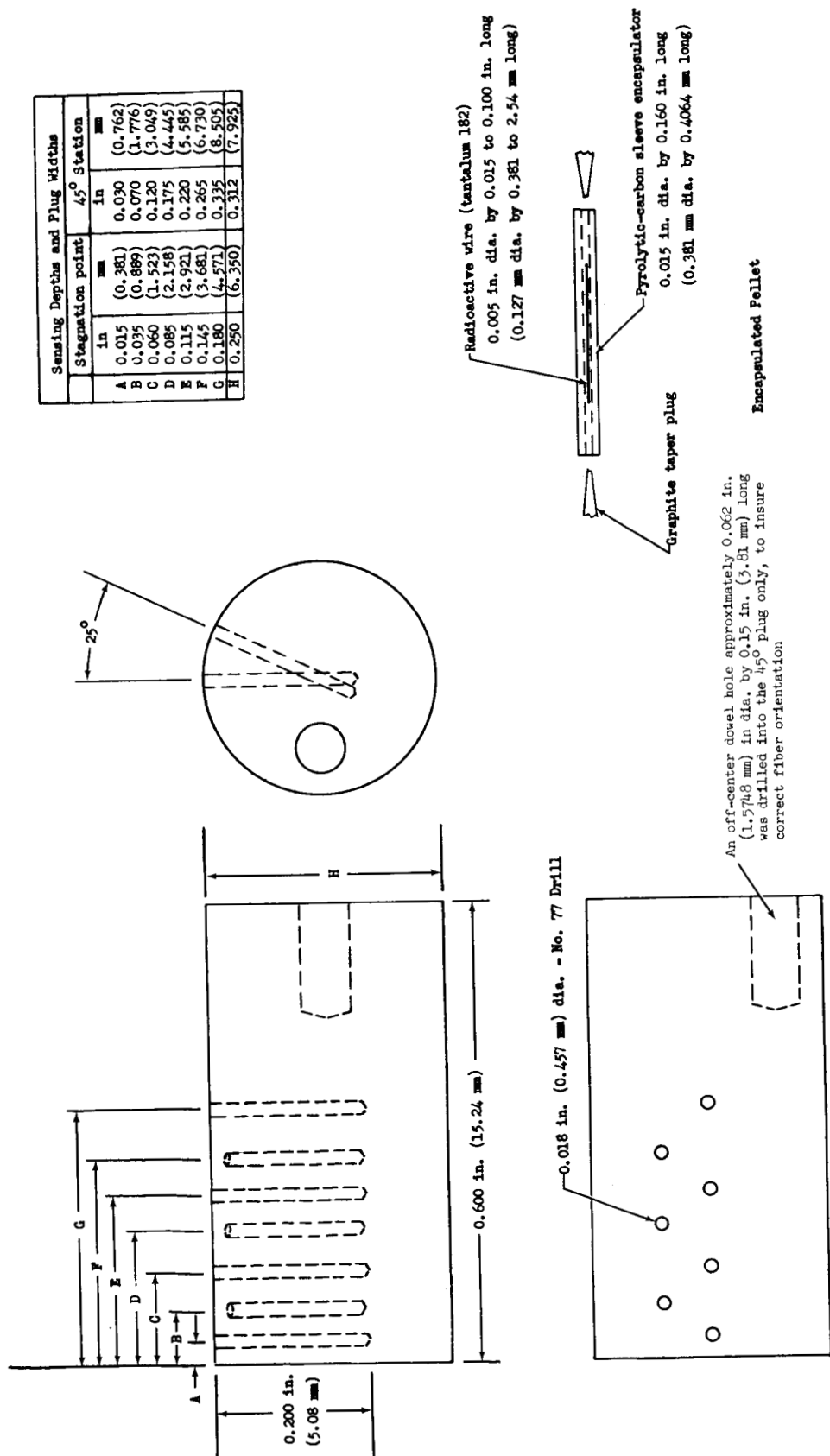


Figure 5.- Sketch of the radioactive sensor plugs.

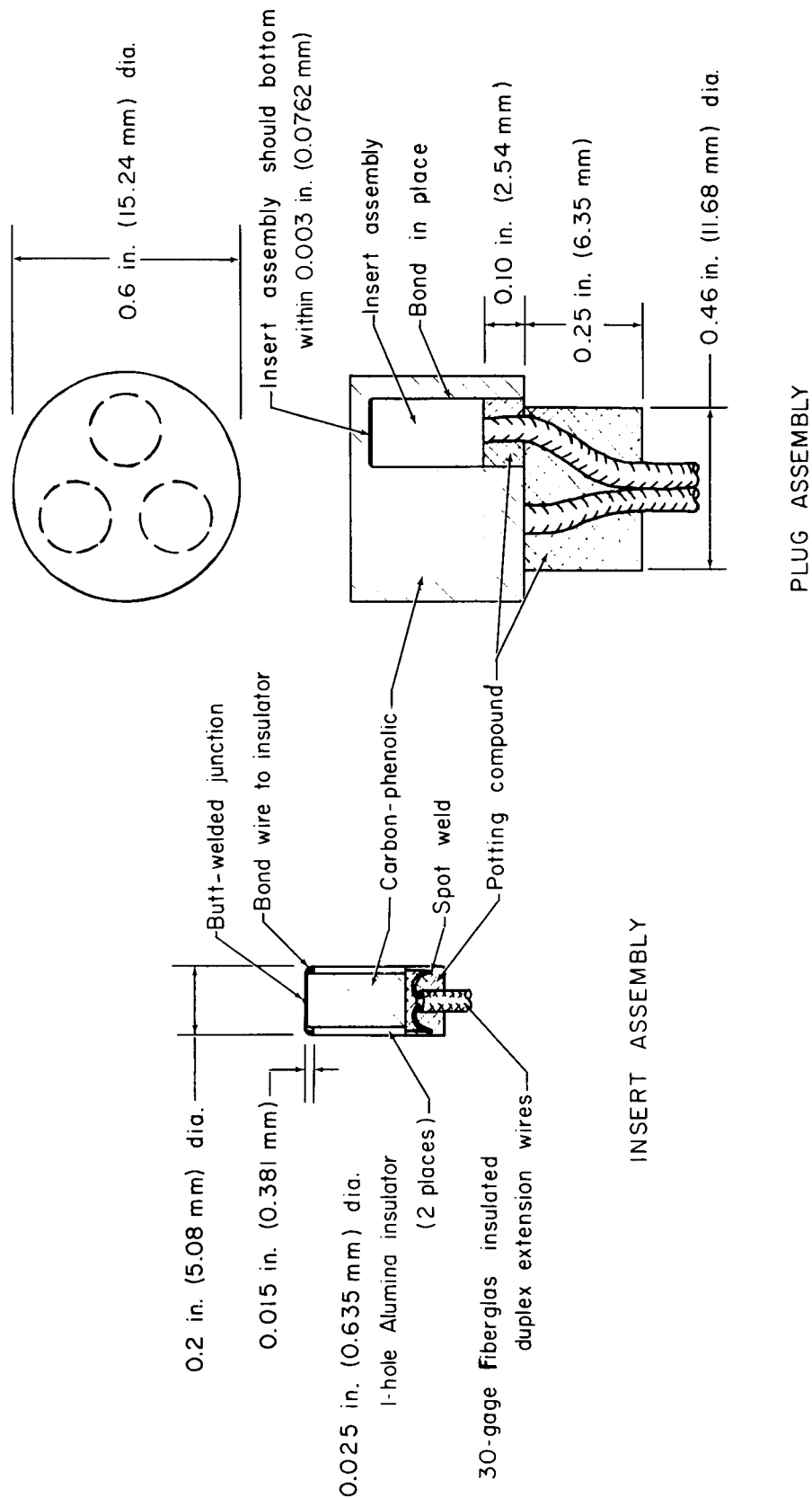
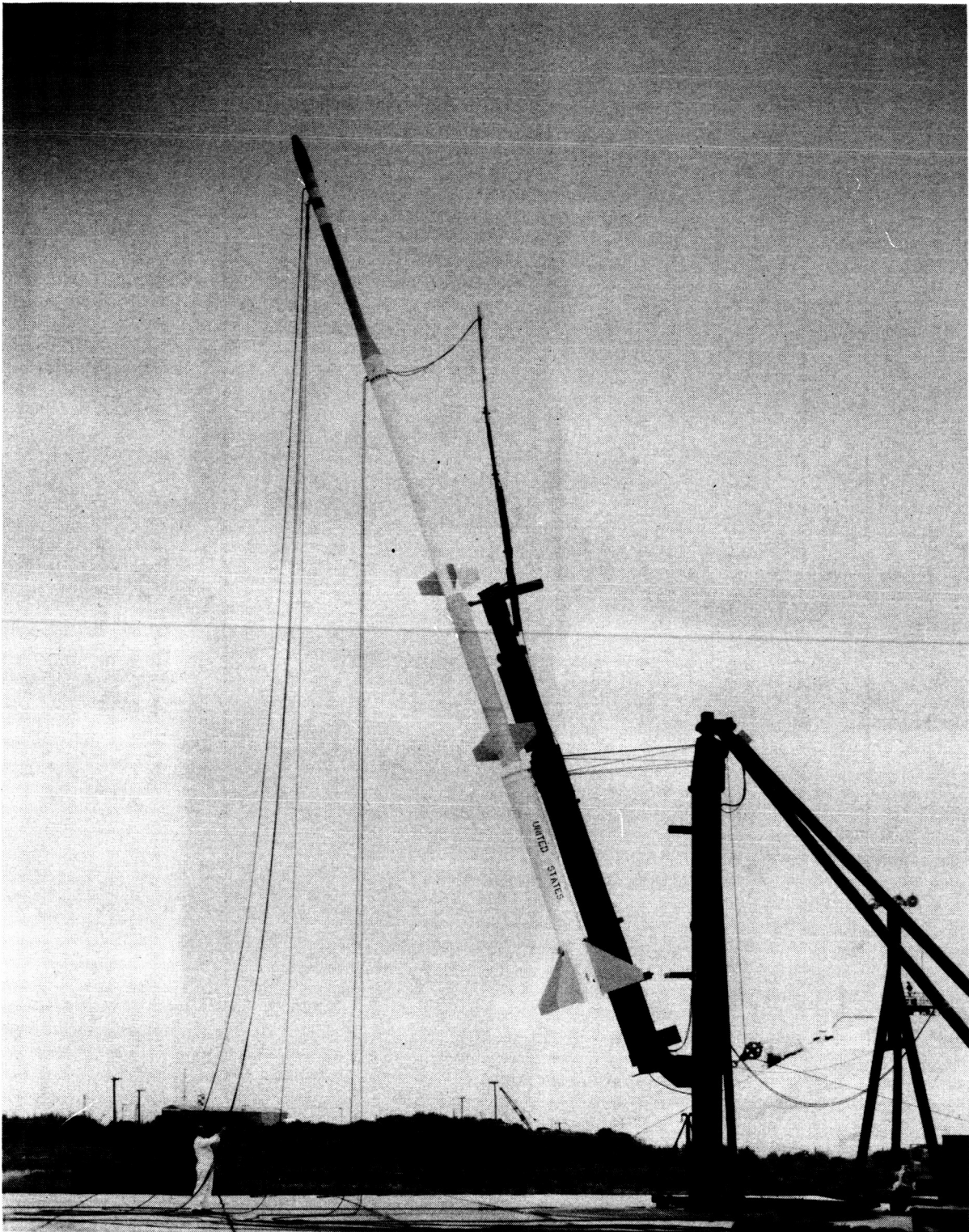


Figure 6. - Typical three-element in-depth thermocouple assembly.



L-69-330

Figure 7.- Photograph of spacecraft and Pacemaker launch vehicle.

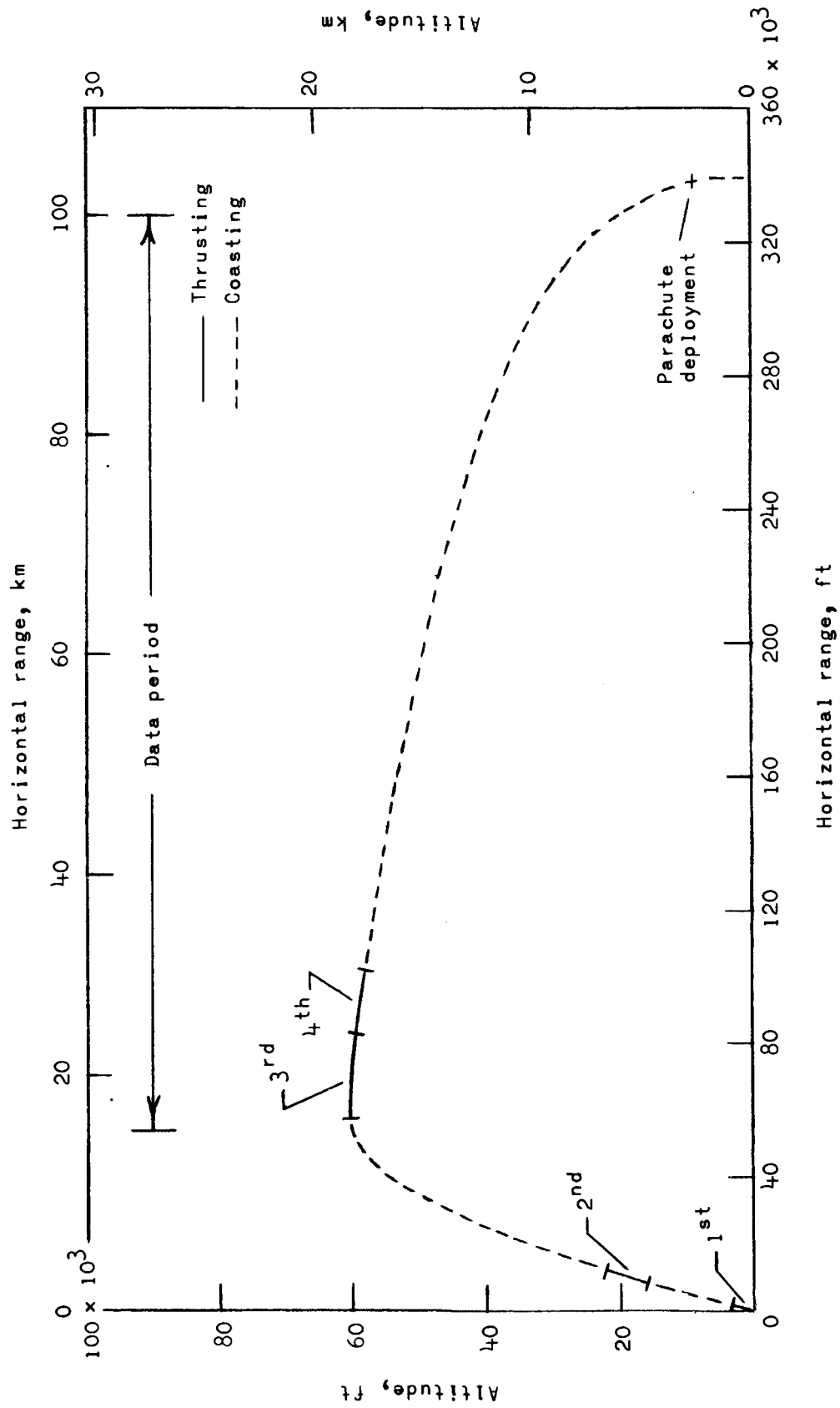


Figure 8.- Flight trajectory showing sequence of events.

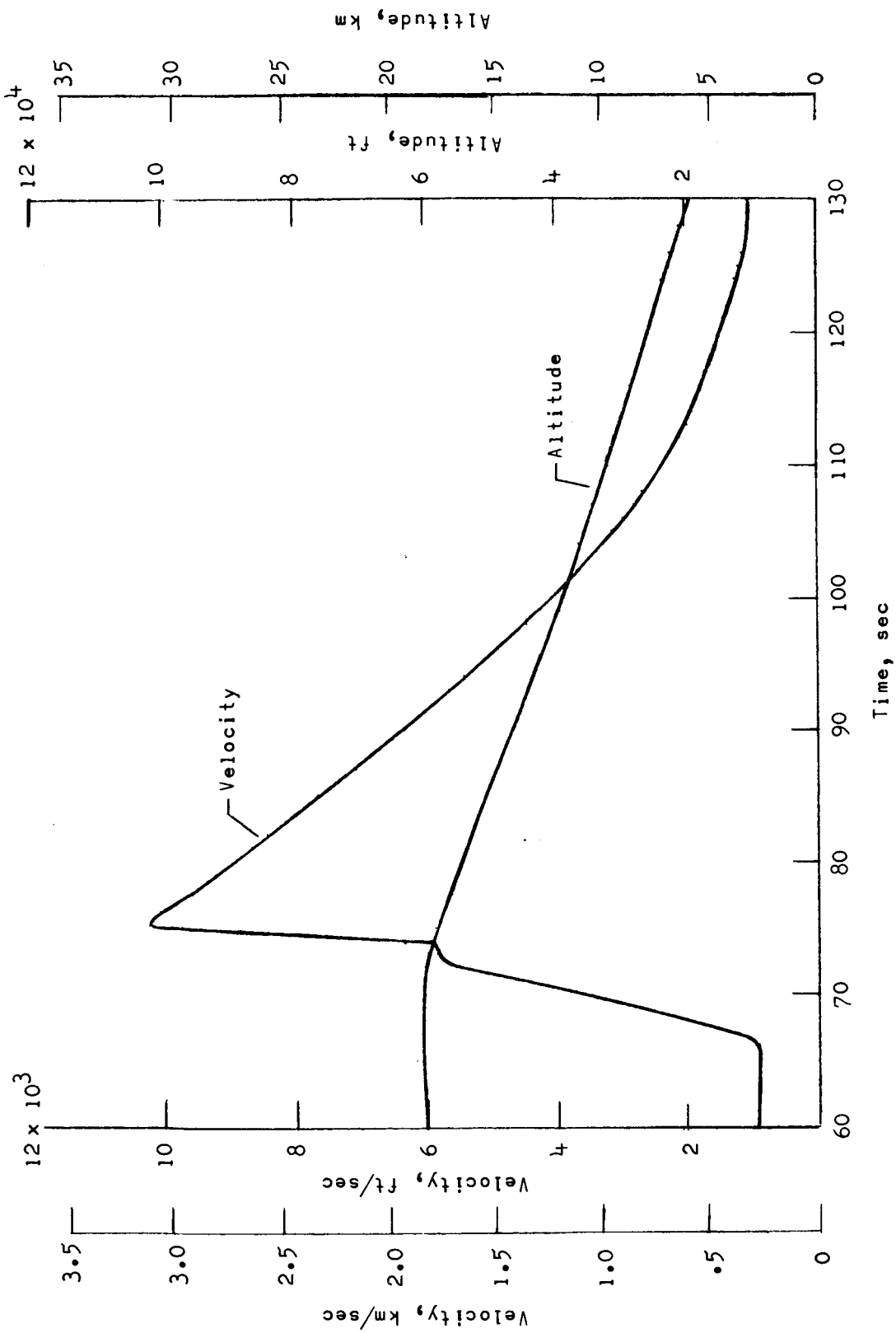
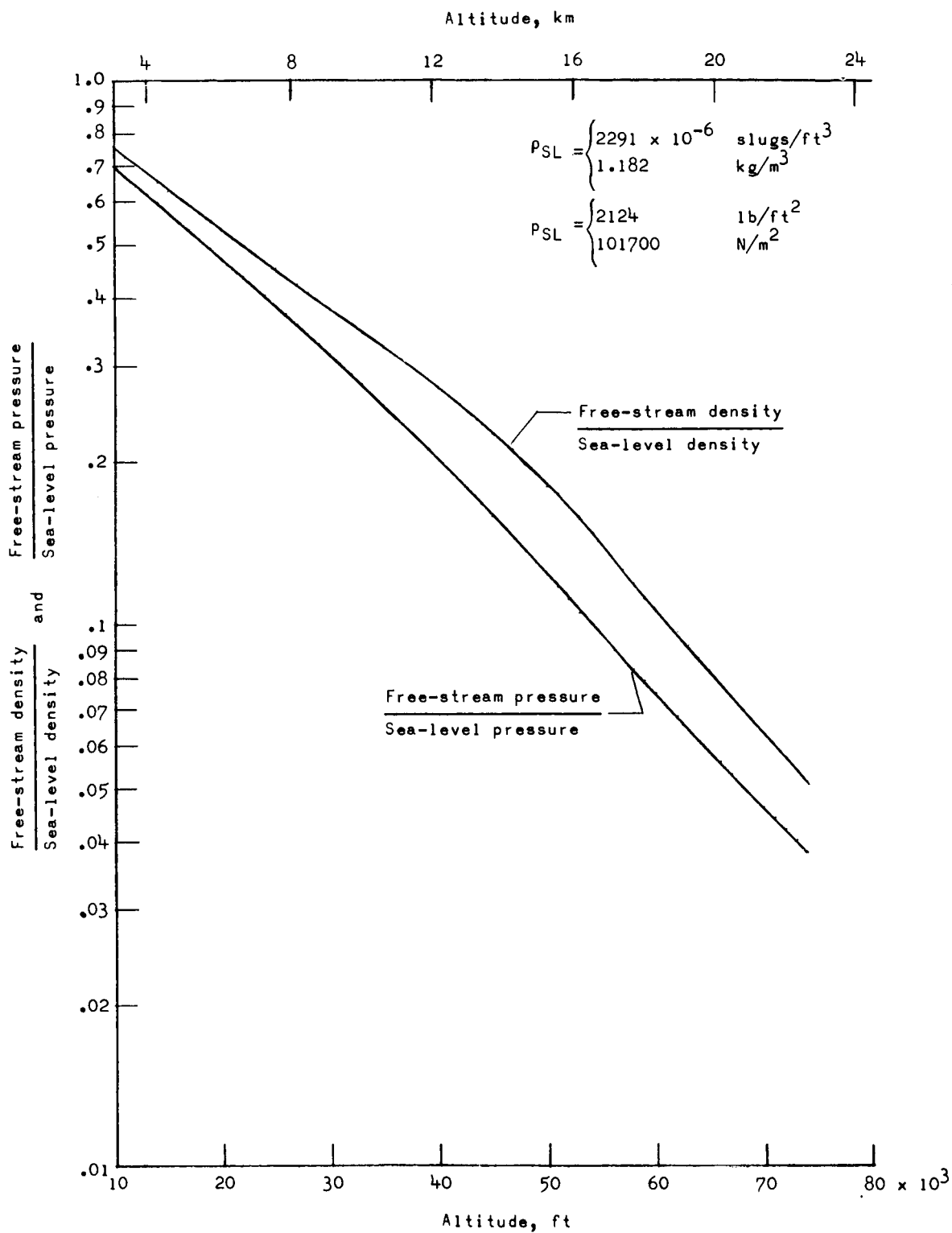
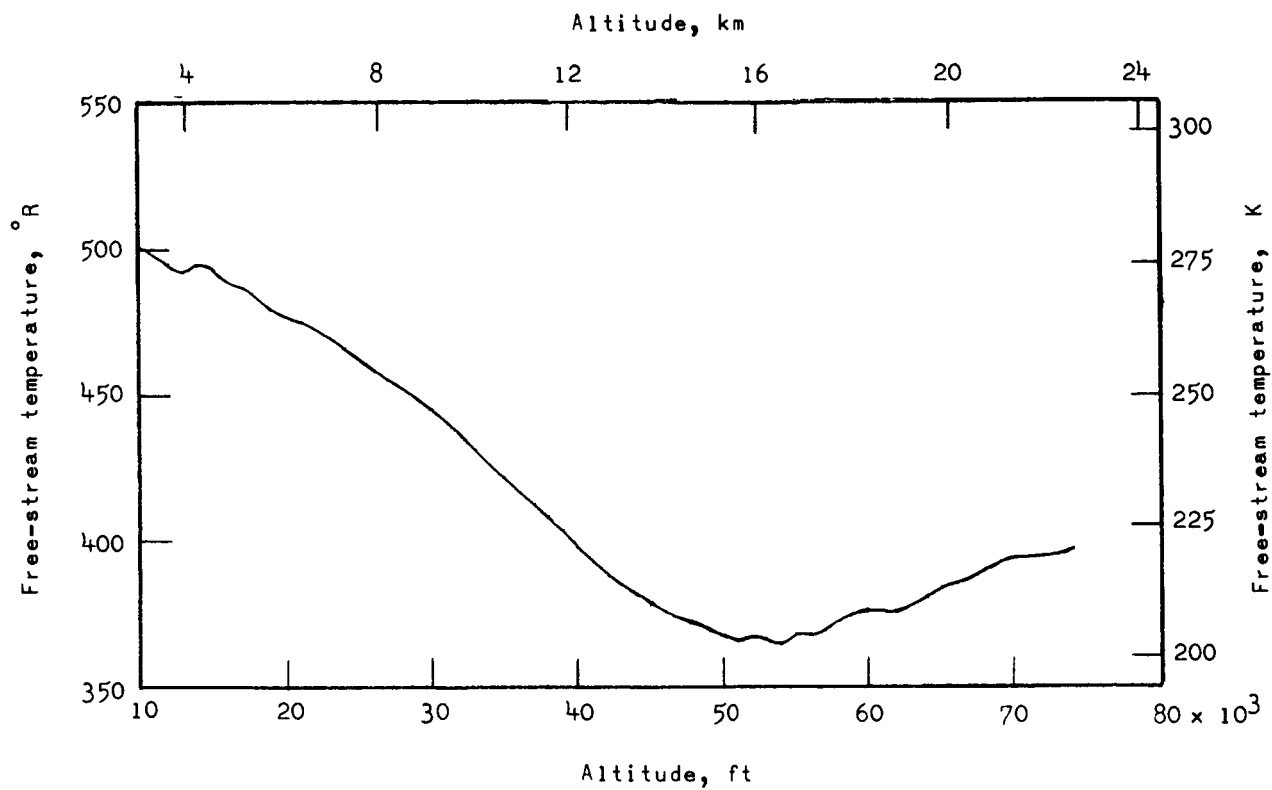


Figure 9.- Time history of velocity and altitude during data period.



(a) Nondimensional pressure and density variation with altitude.

Figure 10.- Atmospheric data obtained from rawinsonde data.



(b) Temperature variation with altitude.

Figure 10.- Concluded.

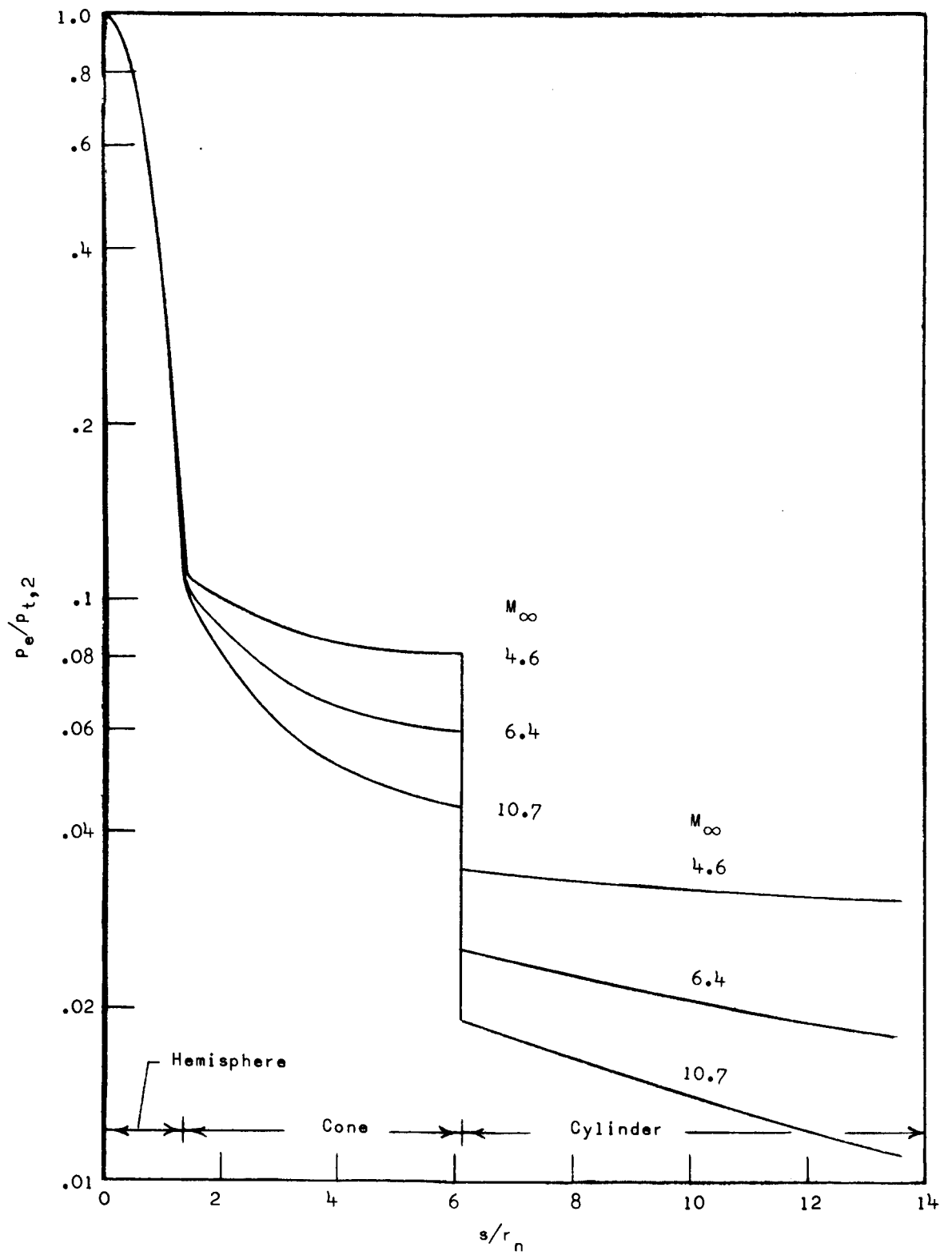
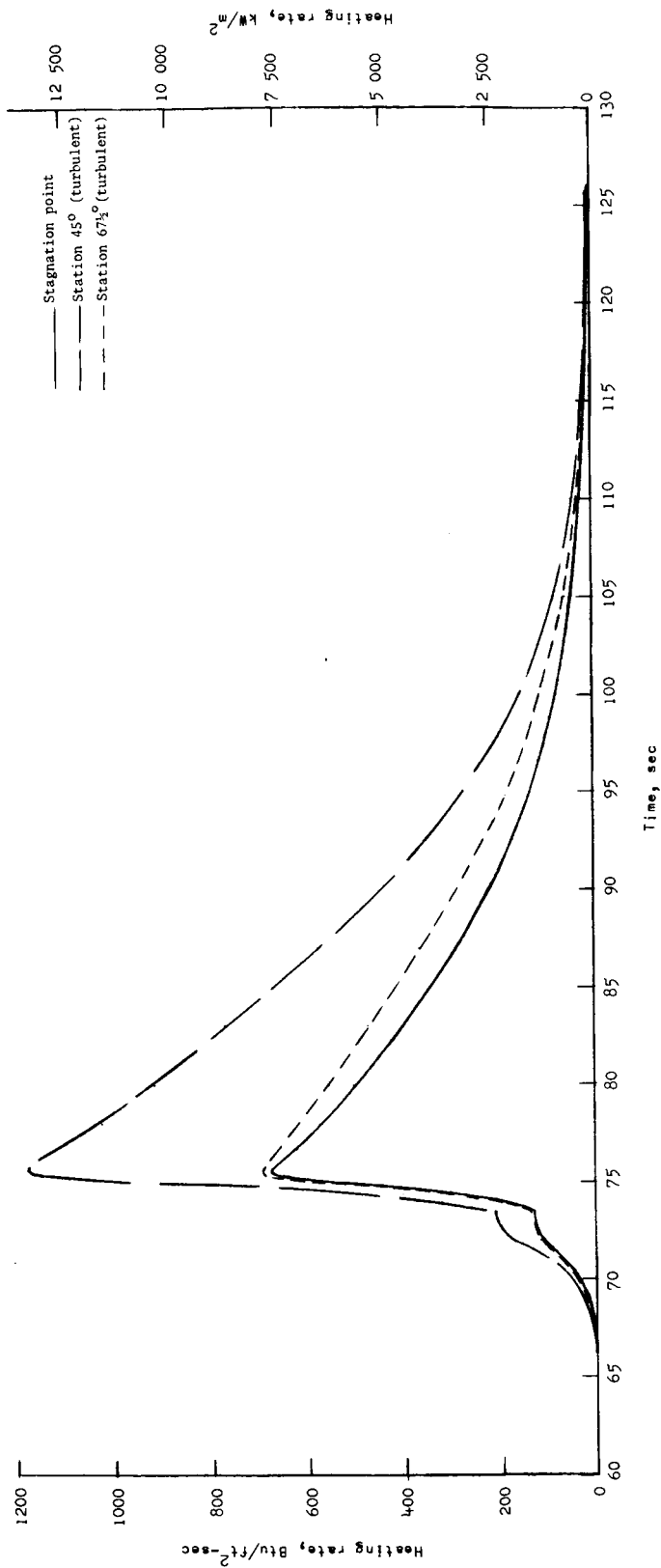
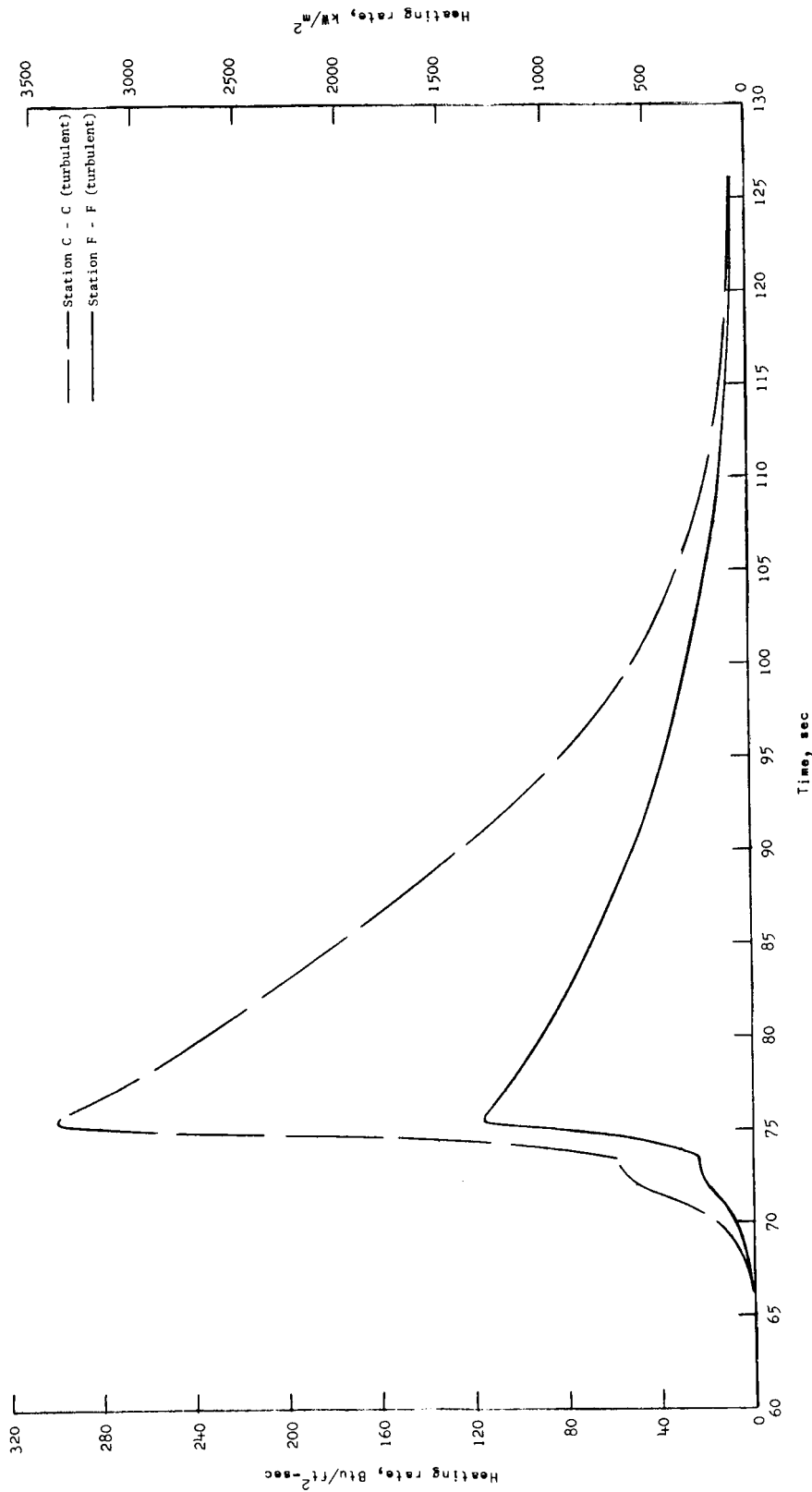


Figure 11.- Computed pressure distributions over the spacecraft.



(a) Stations on hemisphere.

Figure 12. - Computed time histories of cold-wall heating rates.



(b) Stations on cone and cylinder.

Figure 12.- Concluded.

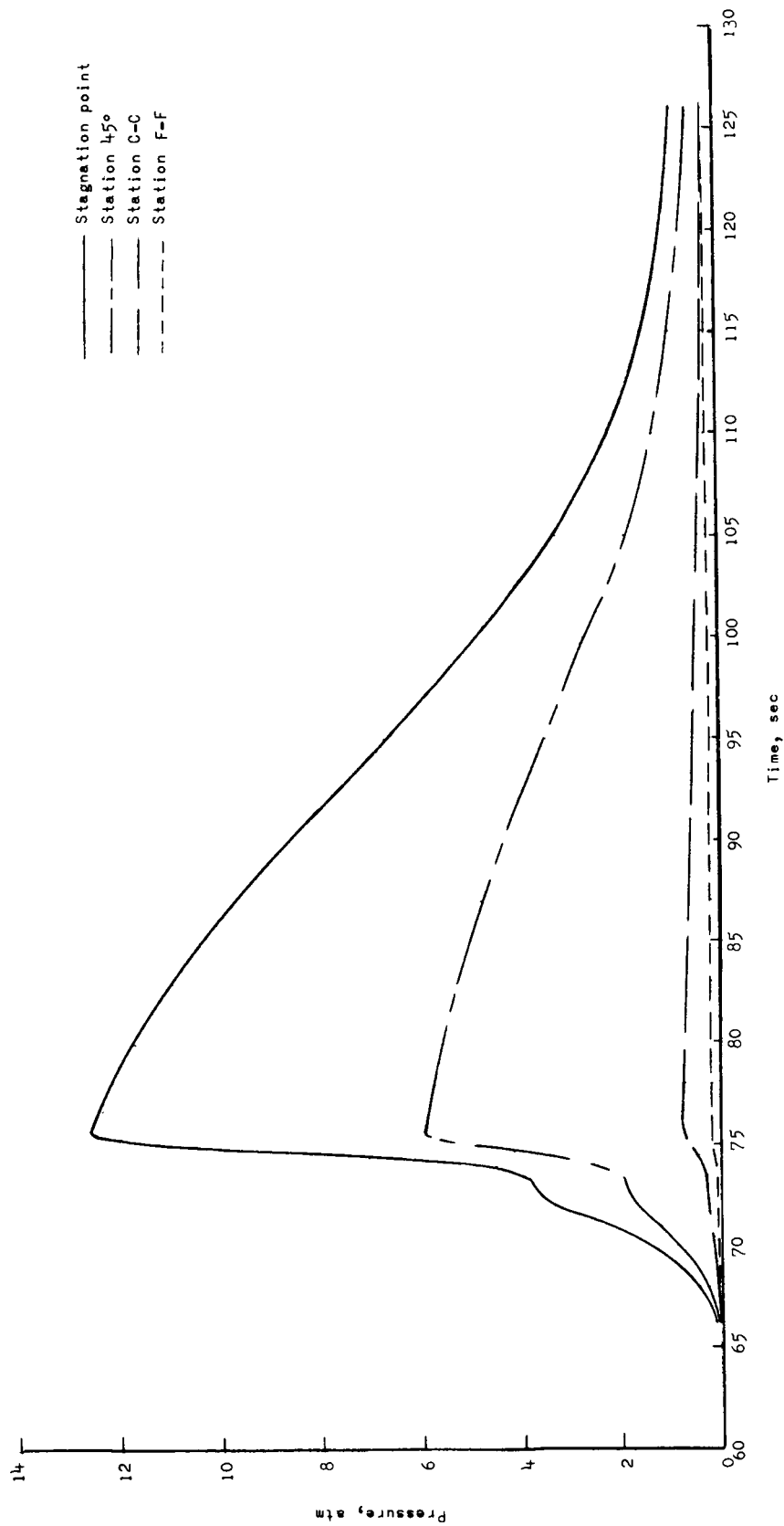


Figure 13.- Computed time histories of local surface pressure.

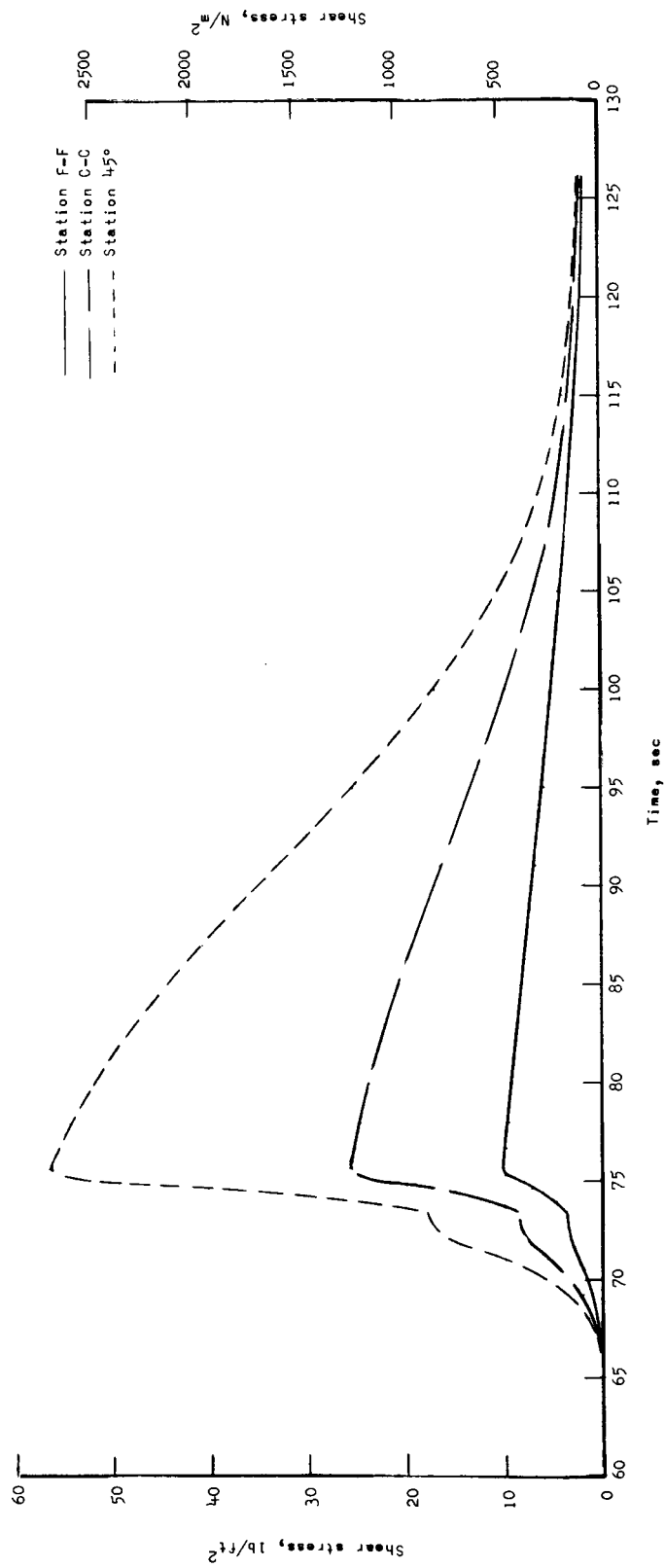


Figure 14. - Computed time histories of shear stress for turbulent flow.

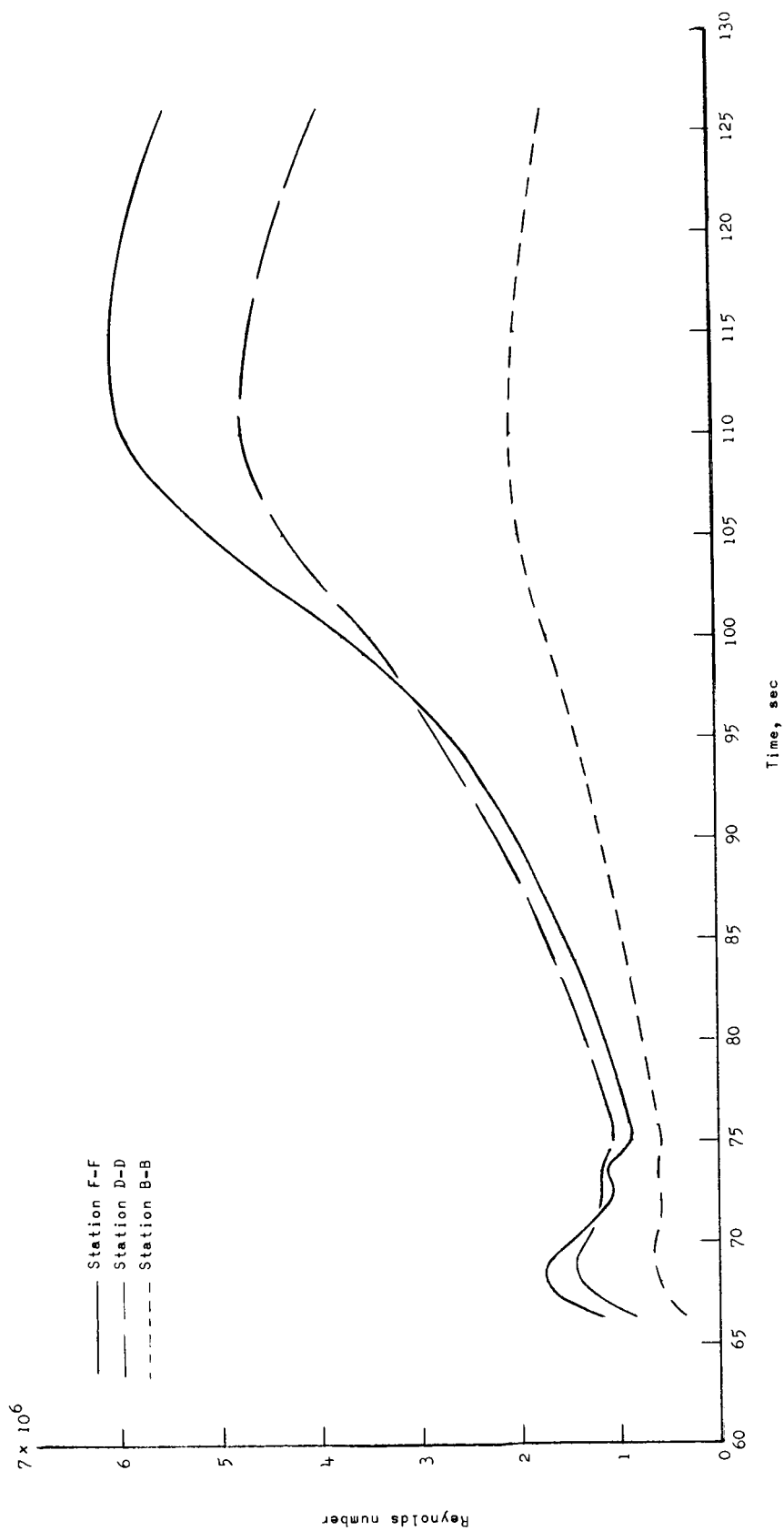
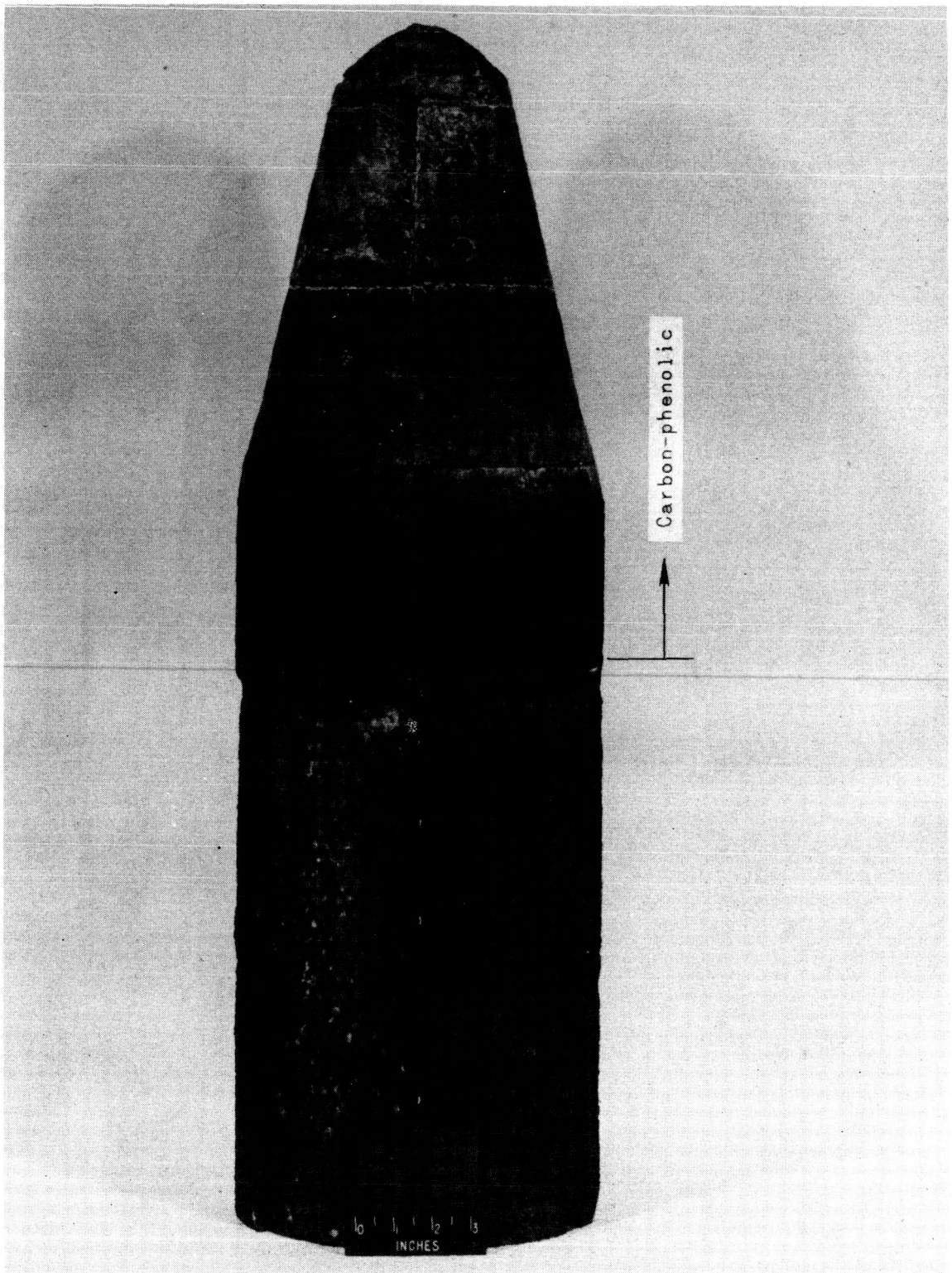


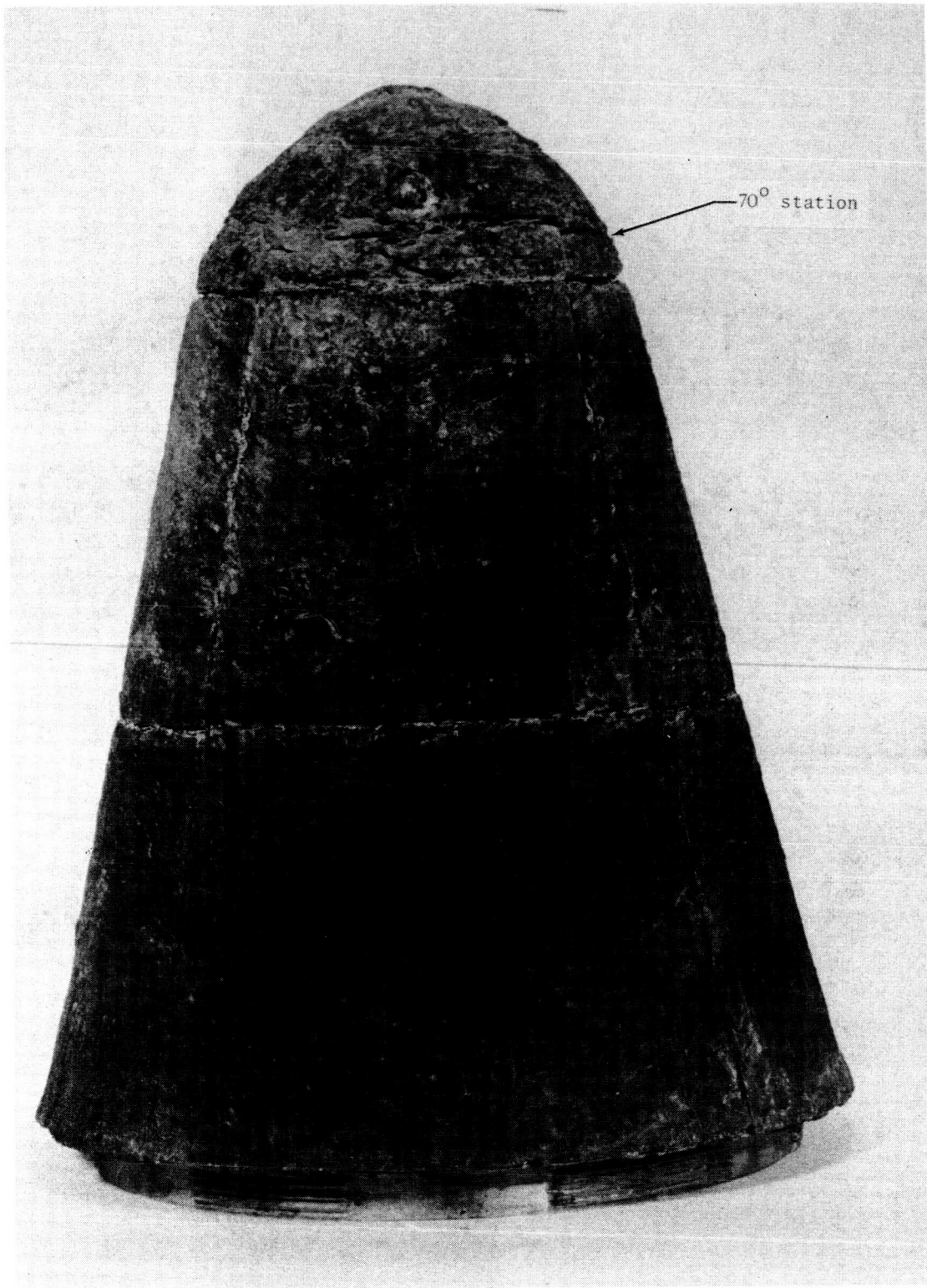
Figure 15.- Computed time histories of Reynolds numbers based on wetted length.



L-69-5424.1

(a) View of the entire spacecraft.

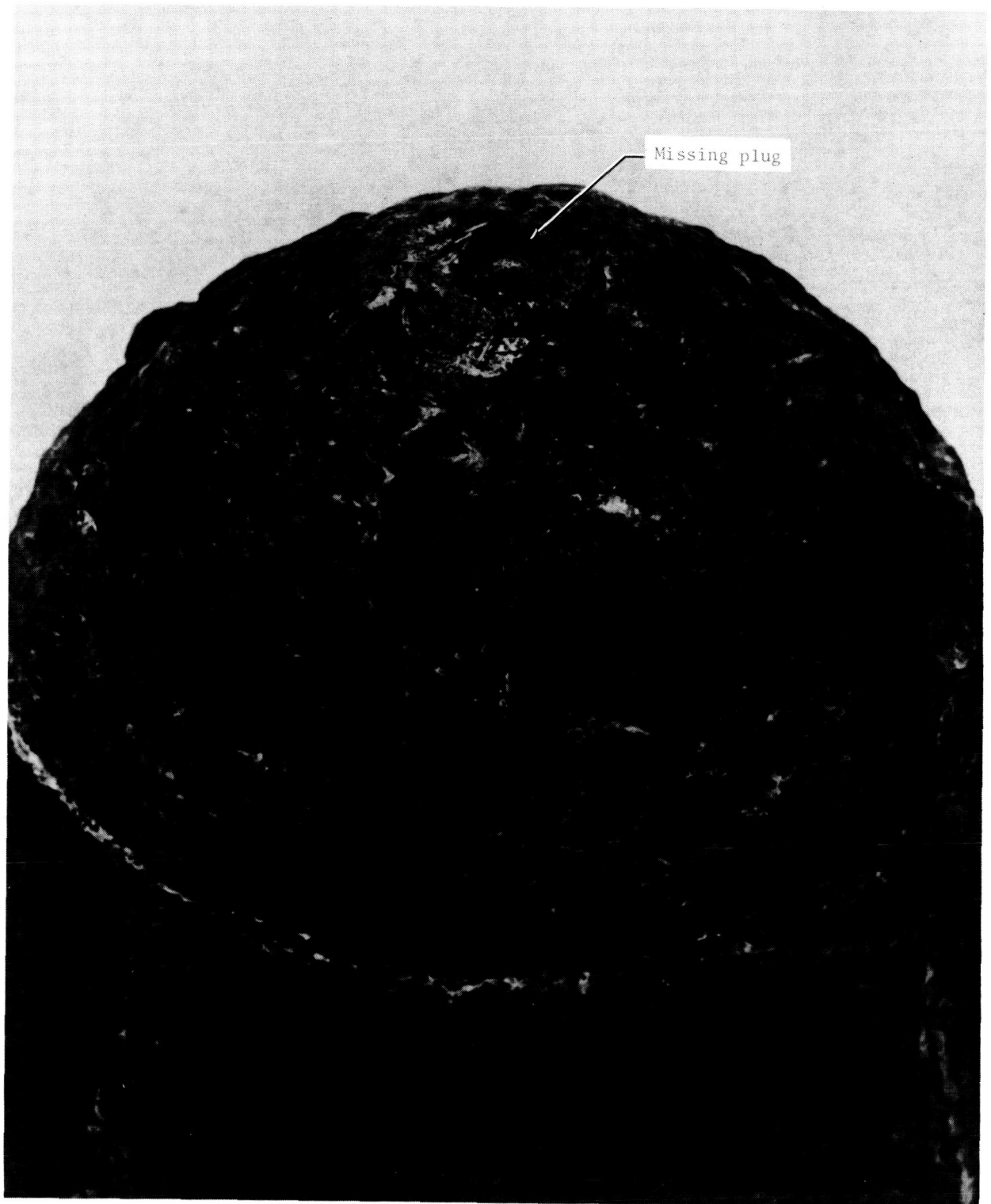
Figure 16.- Photographs of the recovered spacecraft.



L-69-5407.1

(b) View of the hemispherical and conical portion of the spacecraft.

Figure 16.- Continued.



L-69-5402.1

(c) Closeup of the hemispherical nose.

Figure 16.- Concluded.

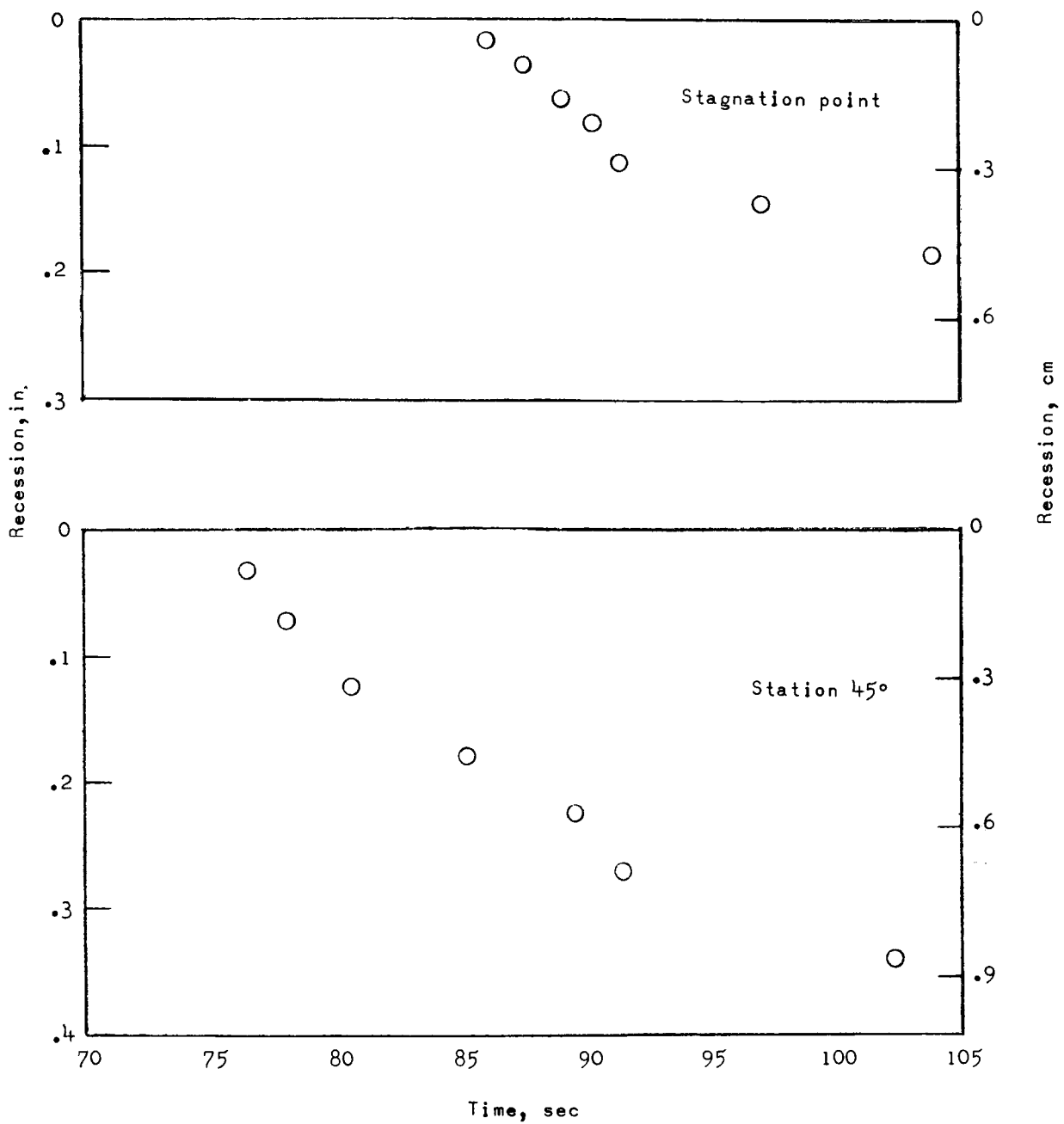
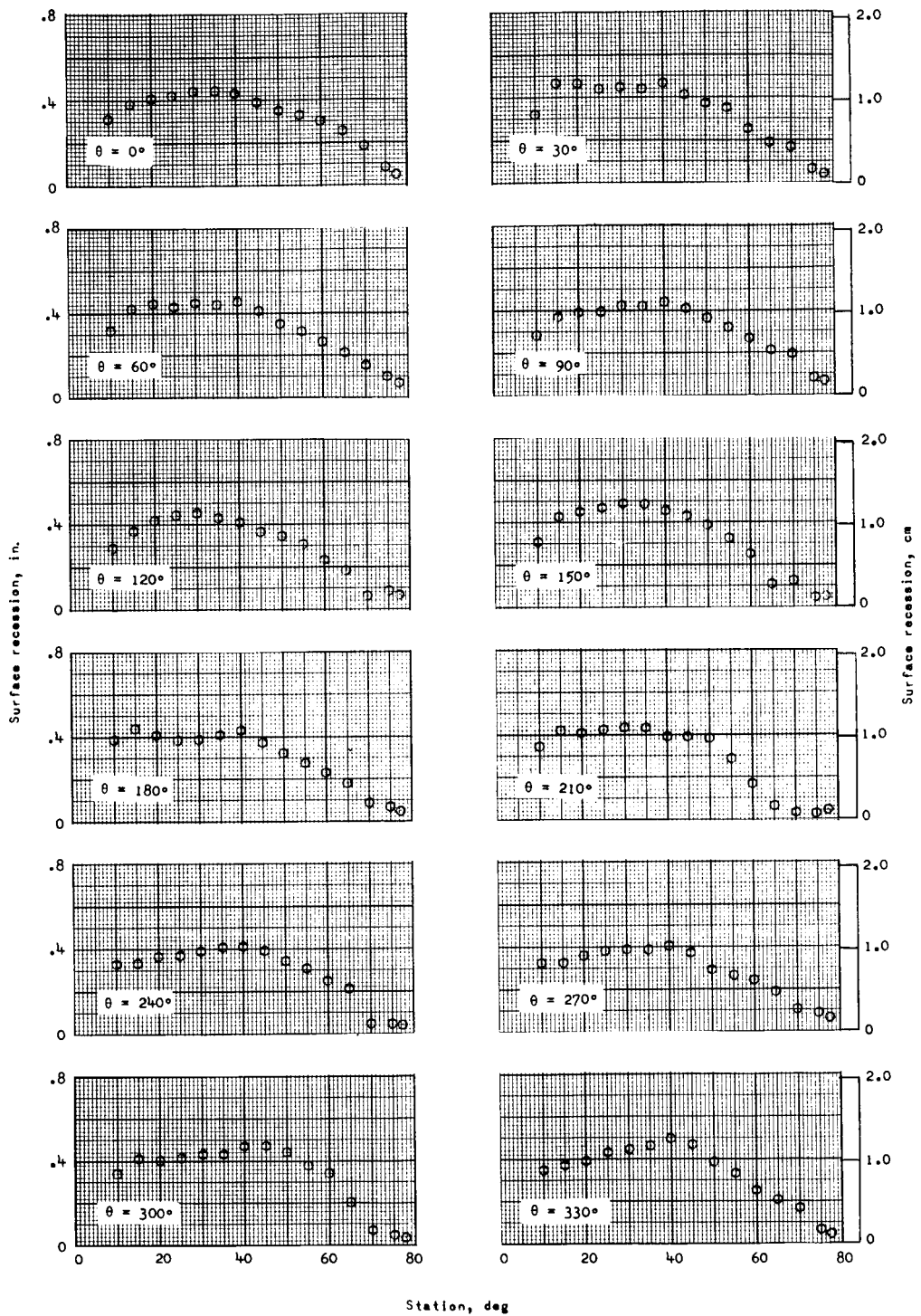
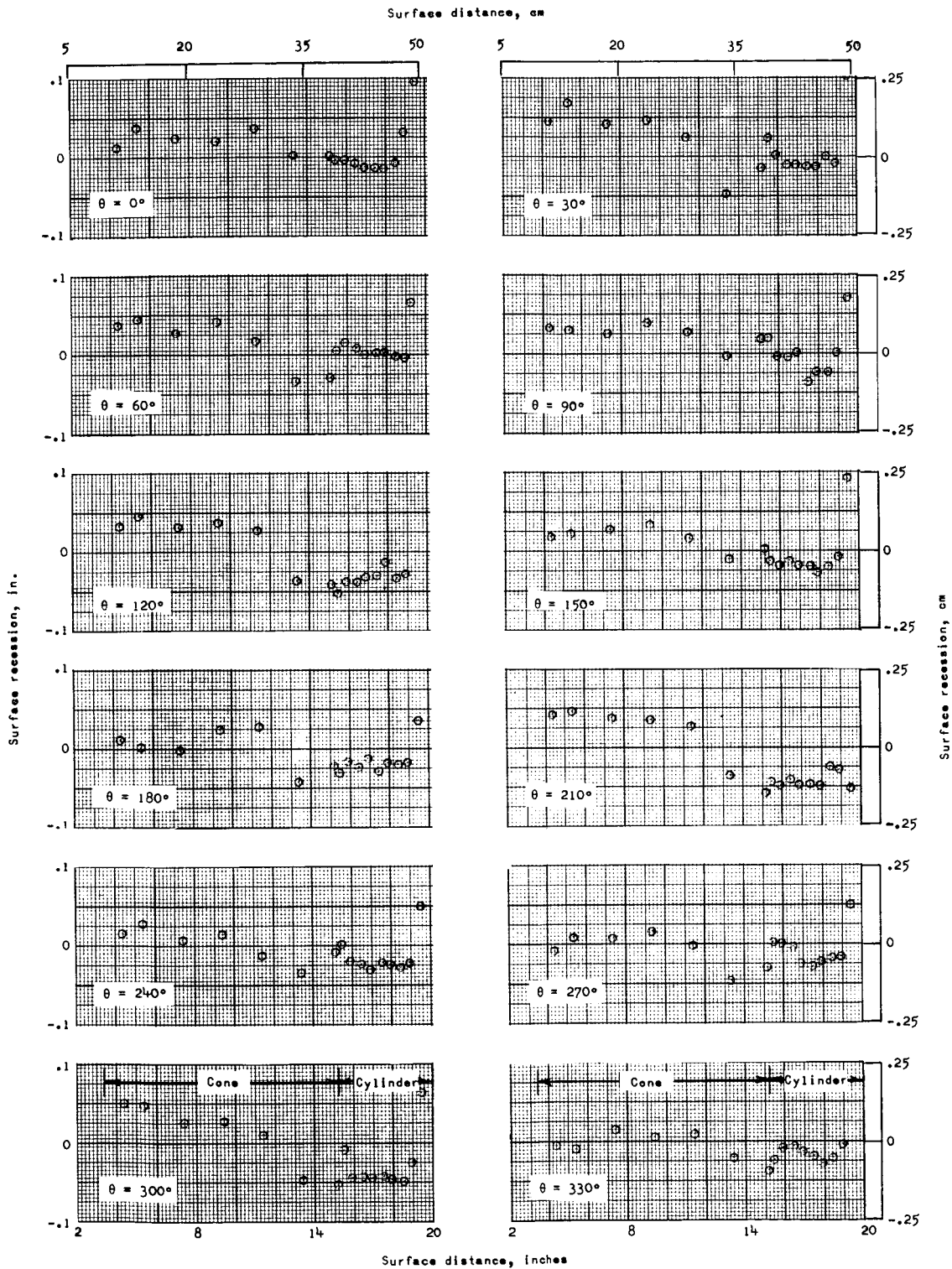


Figure 17.- Time histories of surface recession obtained from radioactive ablation sensors.



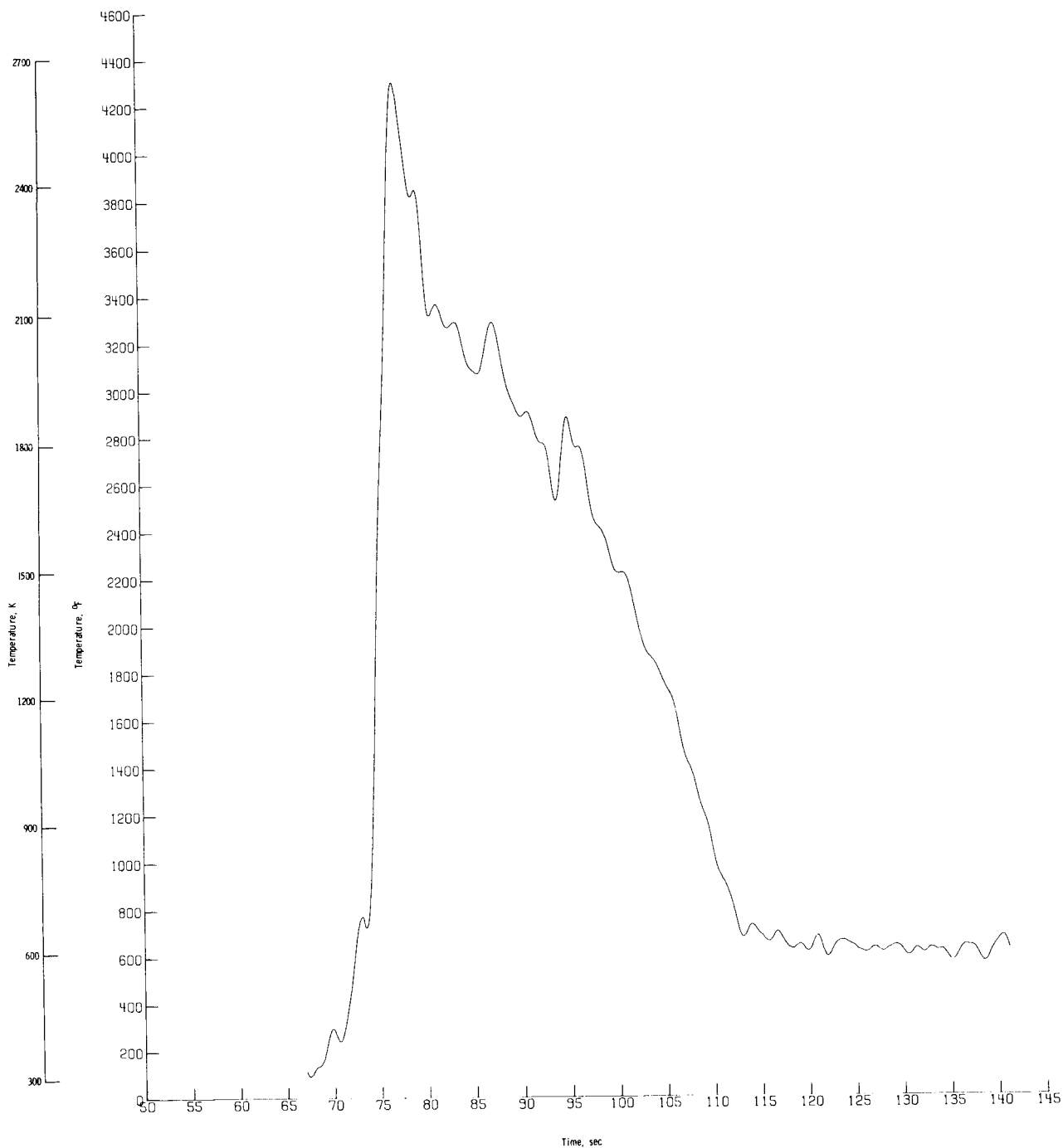
(a) Hemisphere.

Figure 18.- Recession or expansion distances of the spacecraft surface.



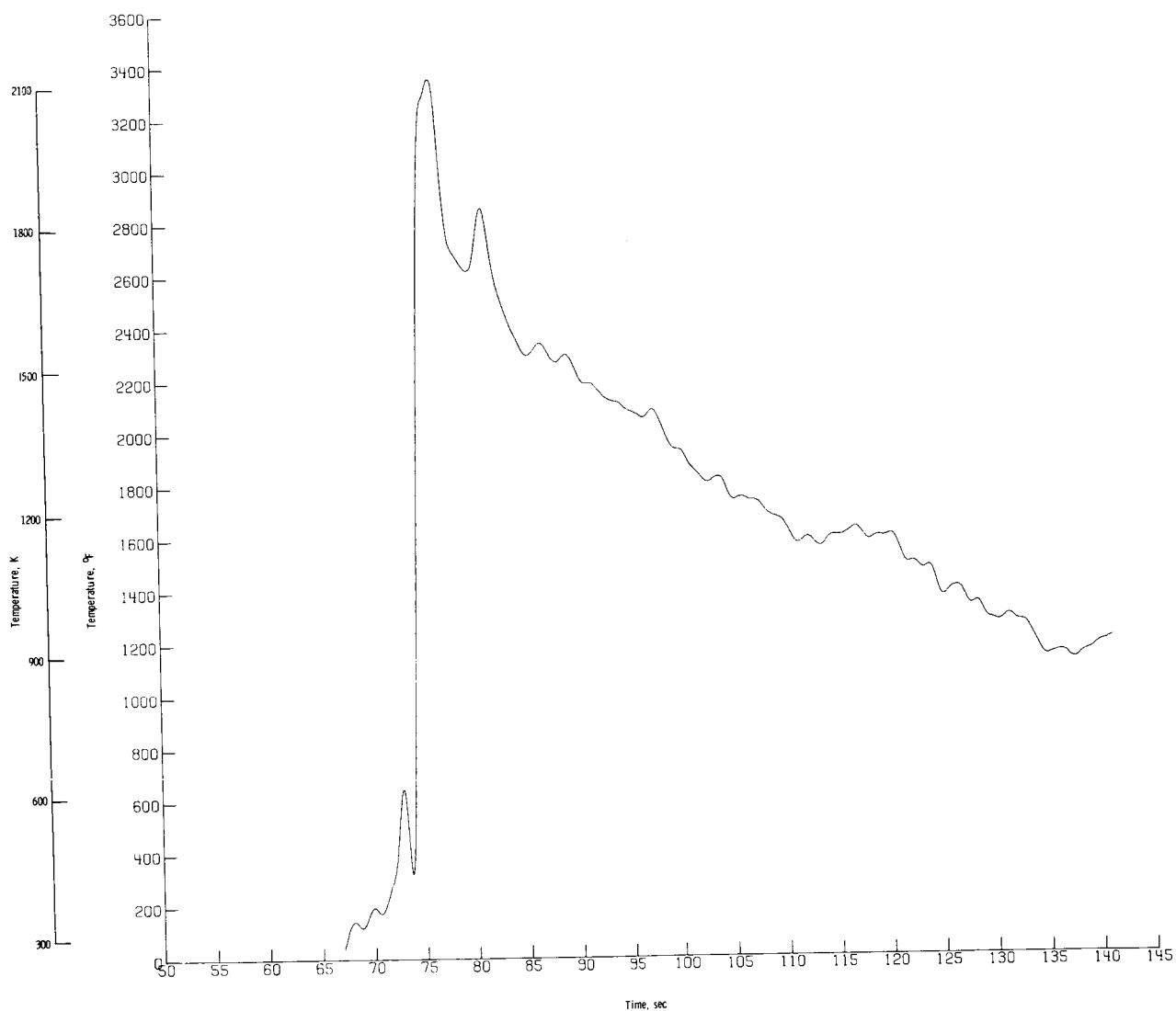
(b) Cone and cylinder. Negative recession is an indication of either swelling of the char layer or separation of the ablator material from the substructure.

Figure 18.- Concluded.



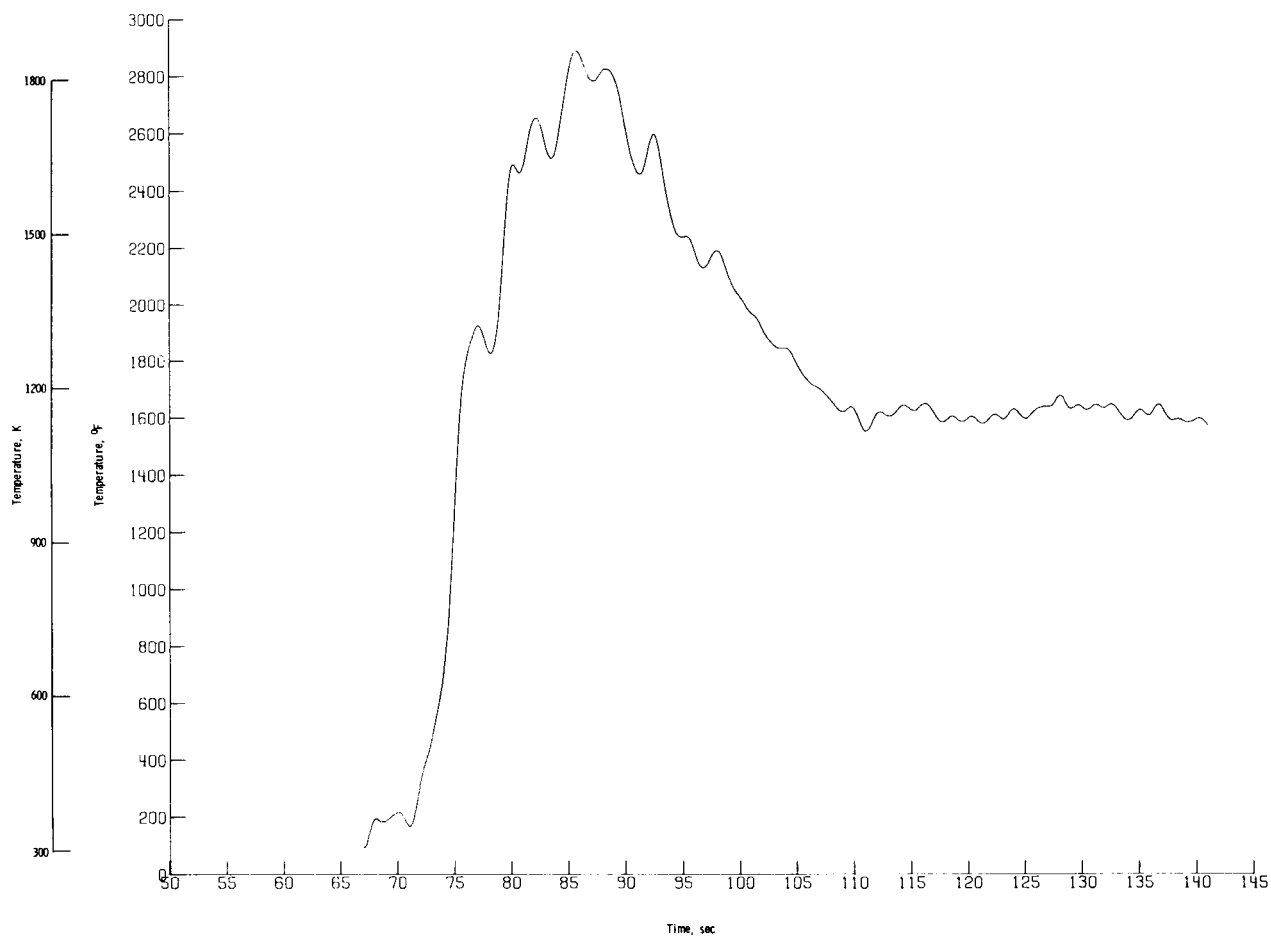
(a) Thermocouple N1.

Figure 19.- Measured surface temperature histories.



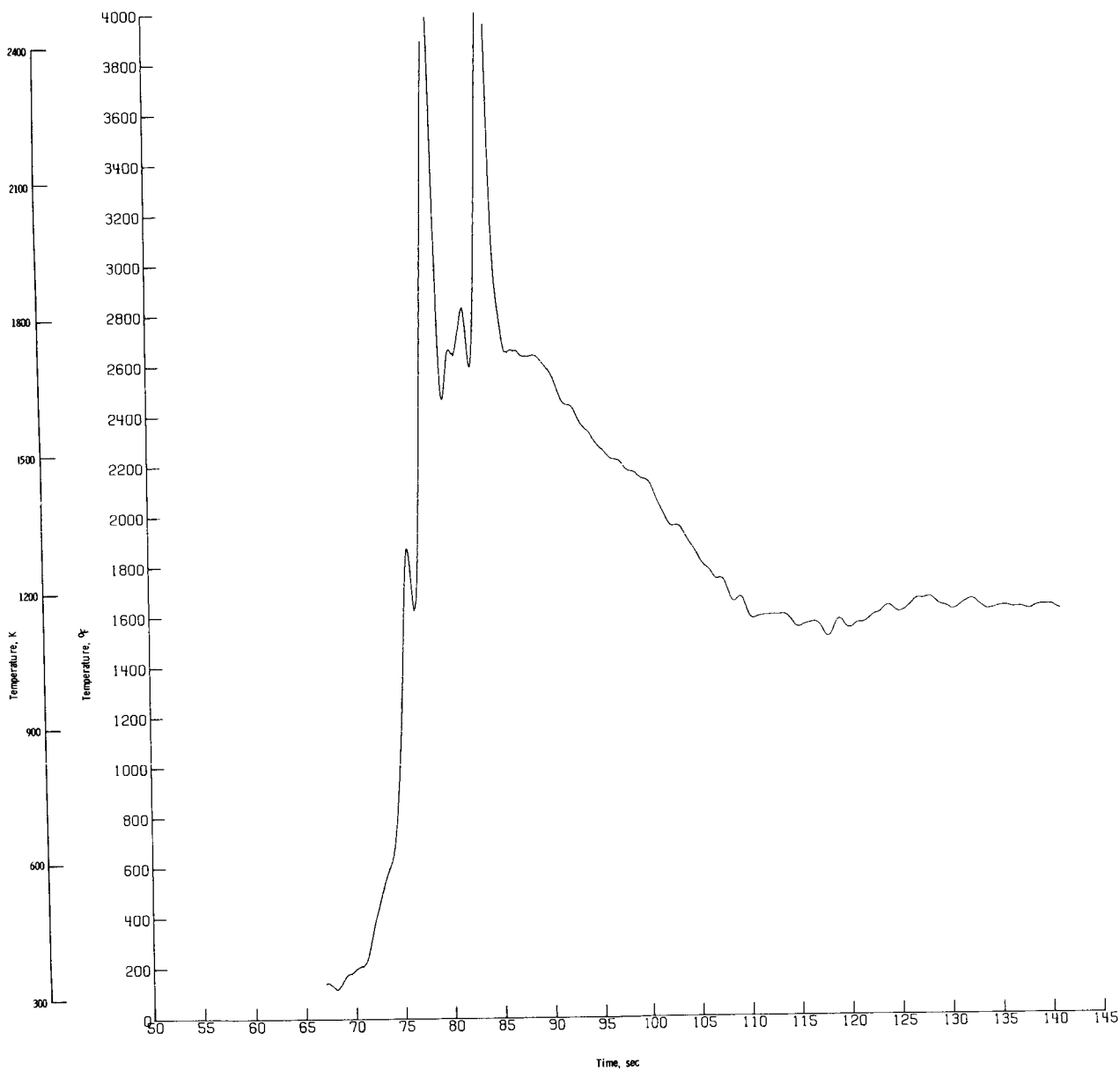
(b) Thermocouple N2.

Figure 19. - Continued.



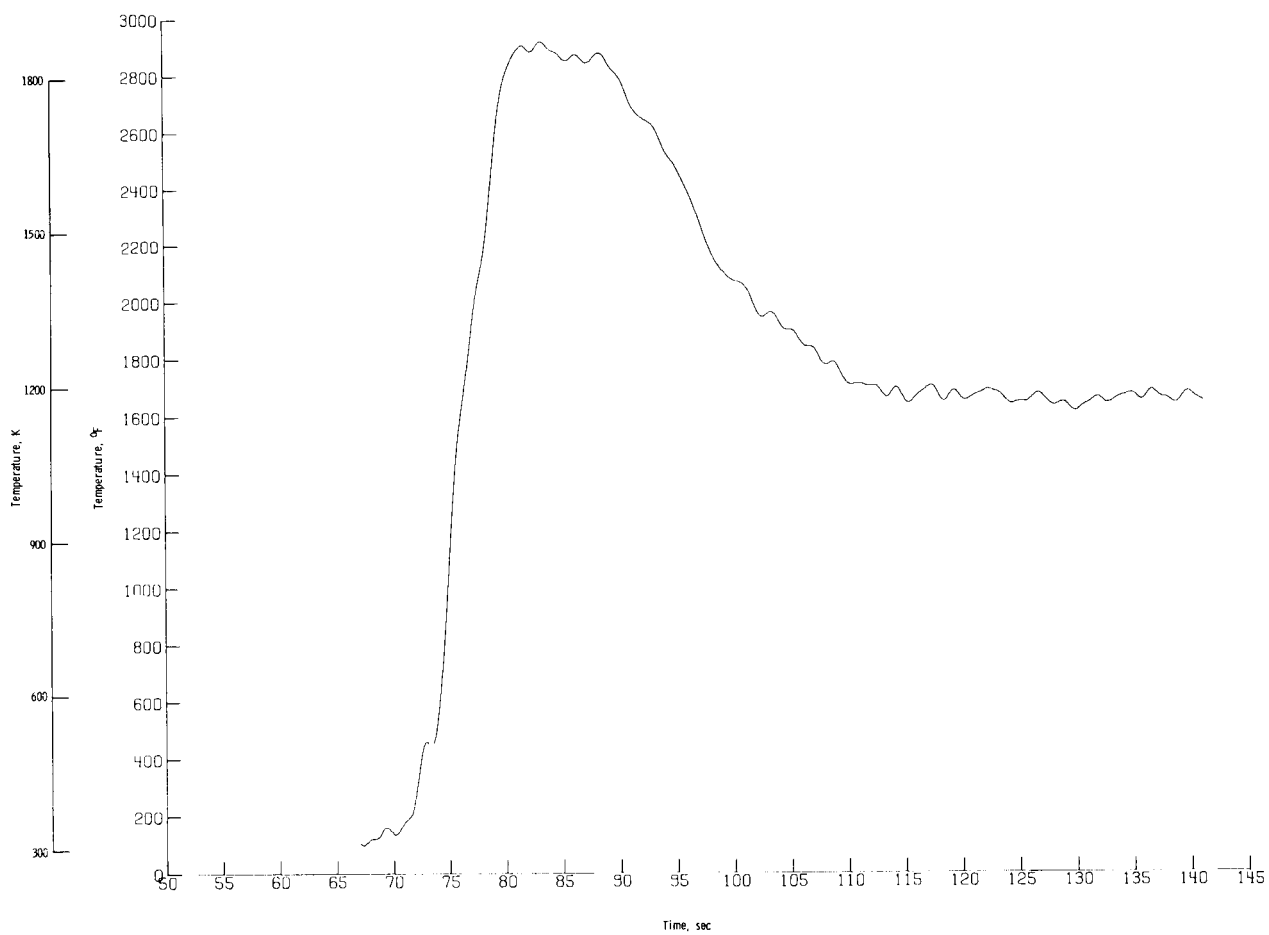
(c) Thermocouple N3.

Figure 19.- Continued.



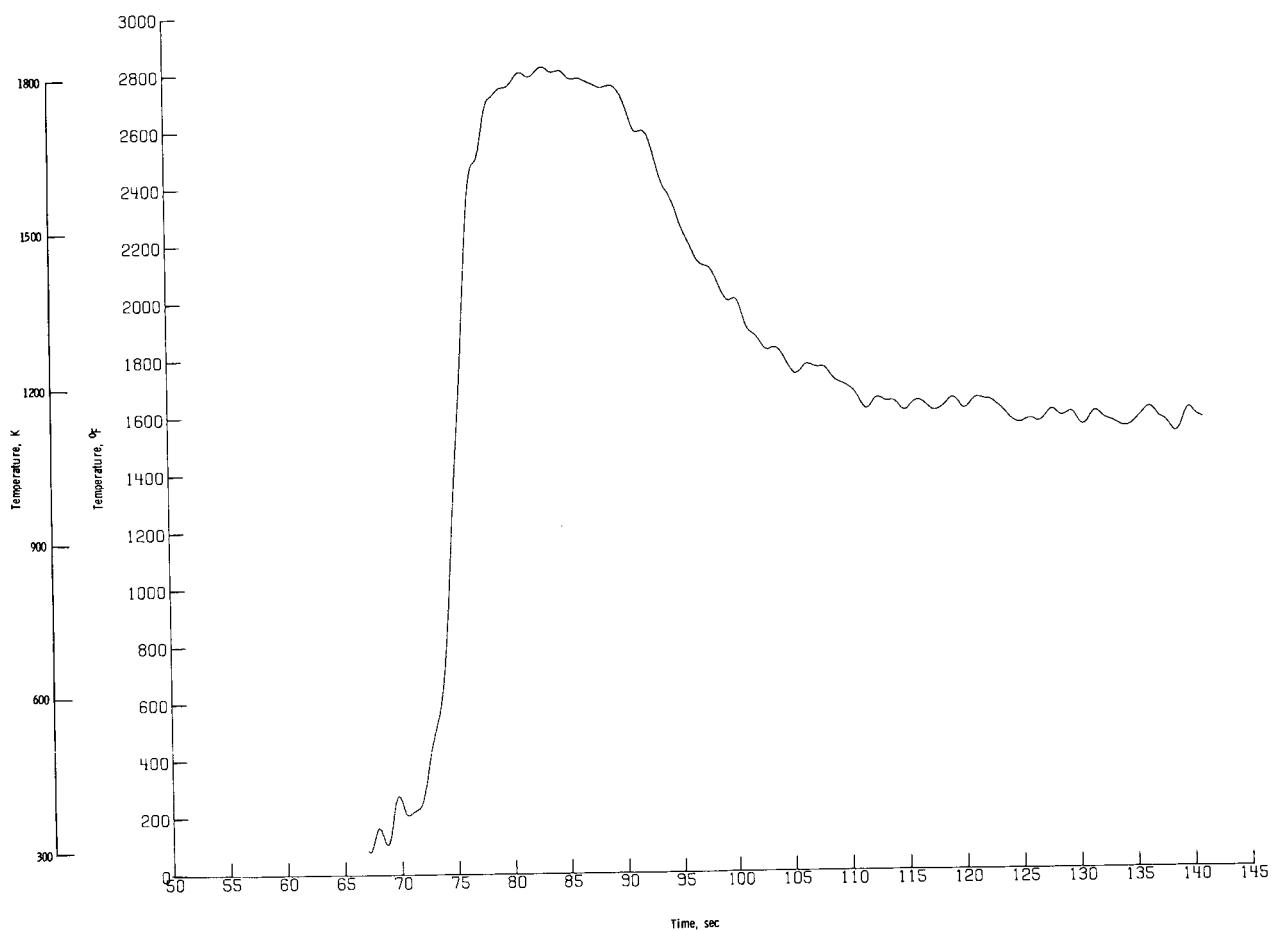
(d) Thermocouple N4.

Figure 19.- Continued.



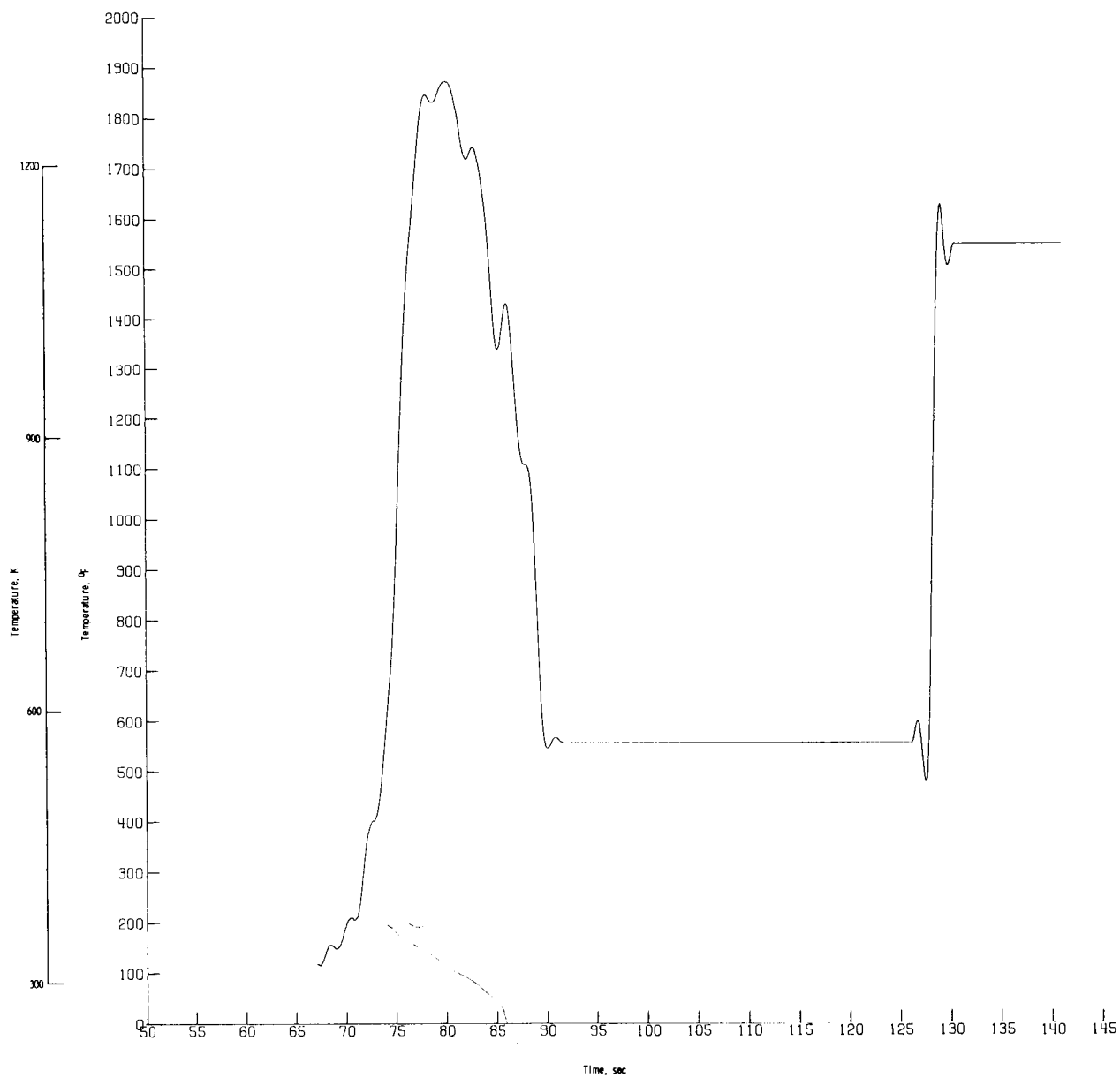
(e) Thermocouple N5.

Figure 19.- Continued.



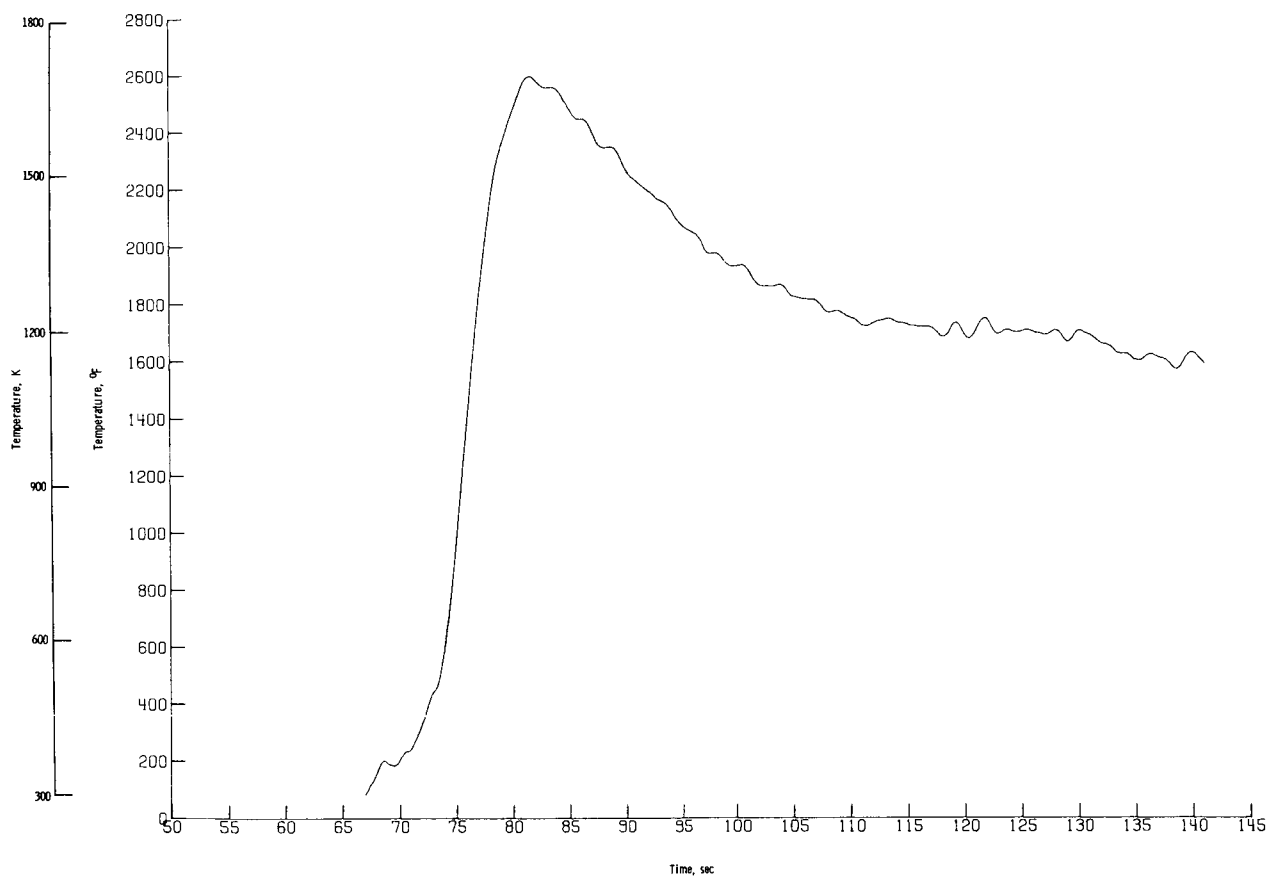
(f) Thermocouple N6.

Figure 19.- Continued.



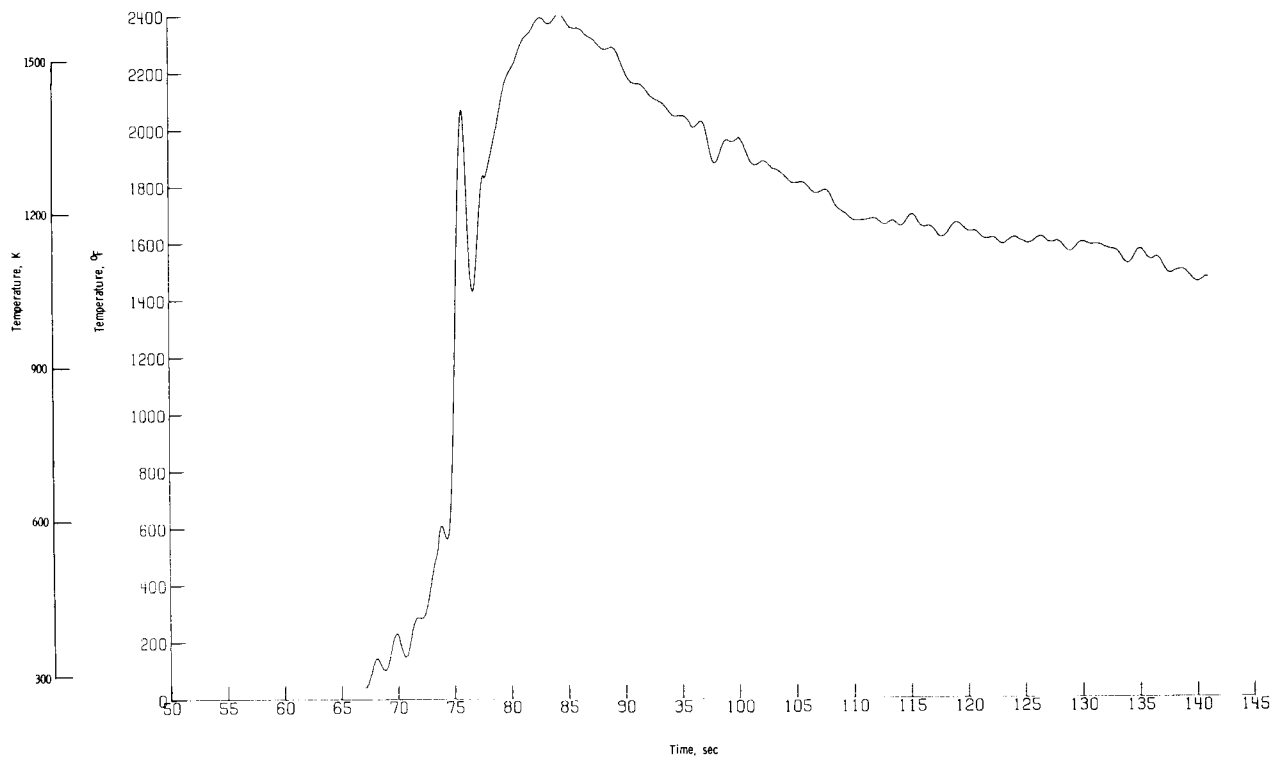
(g) Thermocouple N7.

Figure 19.- Continued.



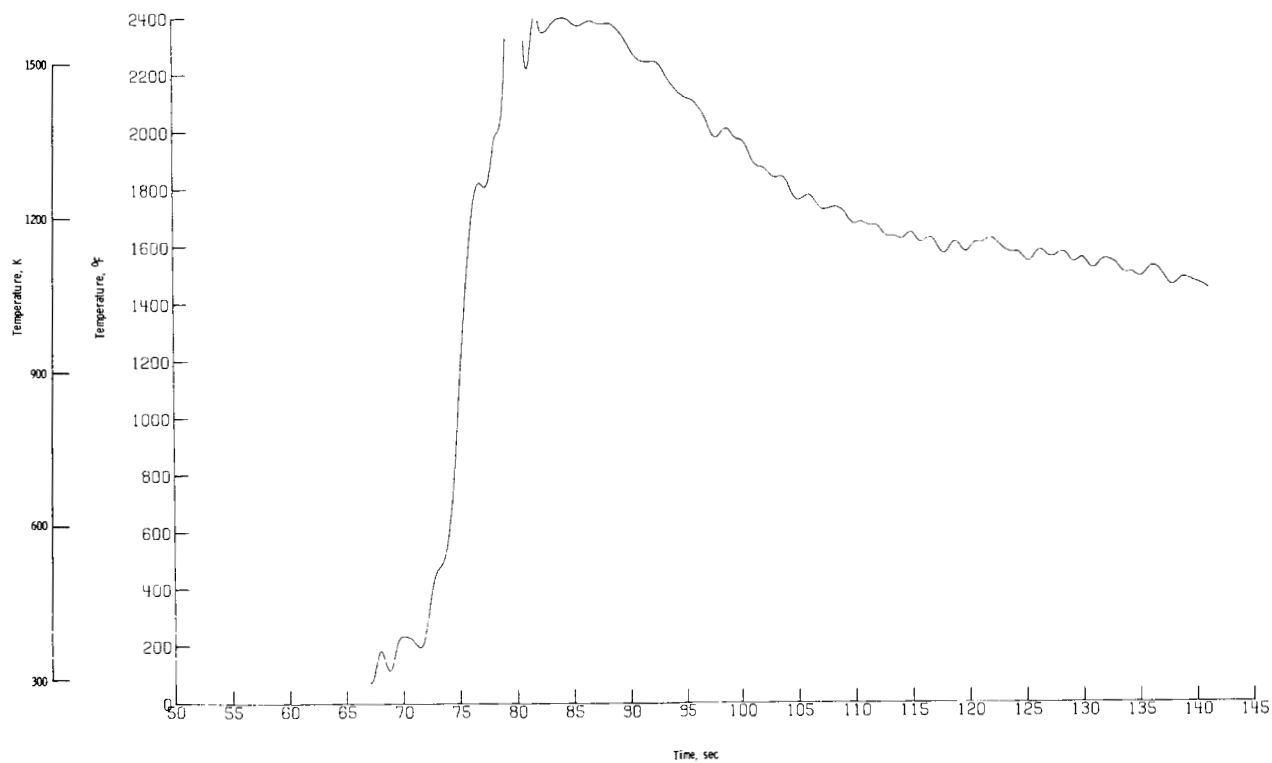
(h) Thermocouple N8.

Figure 19.- Continued.



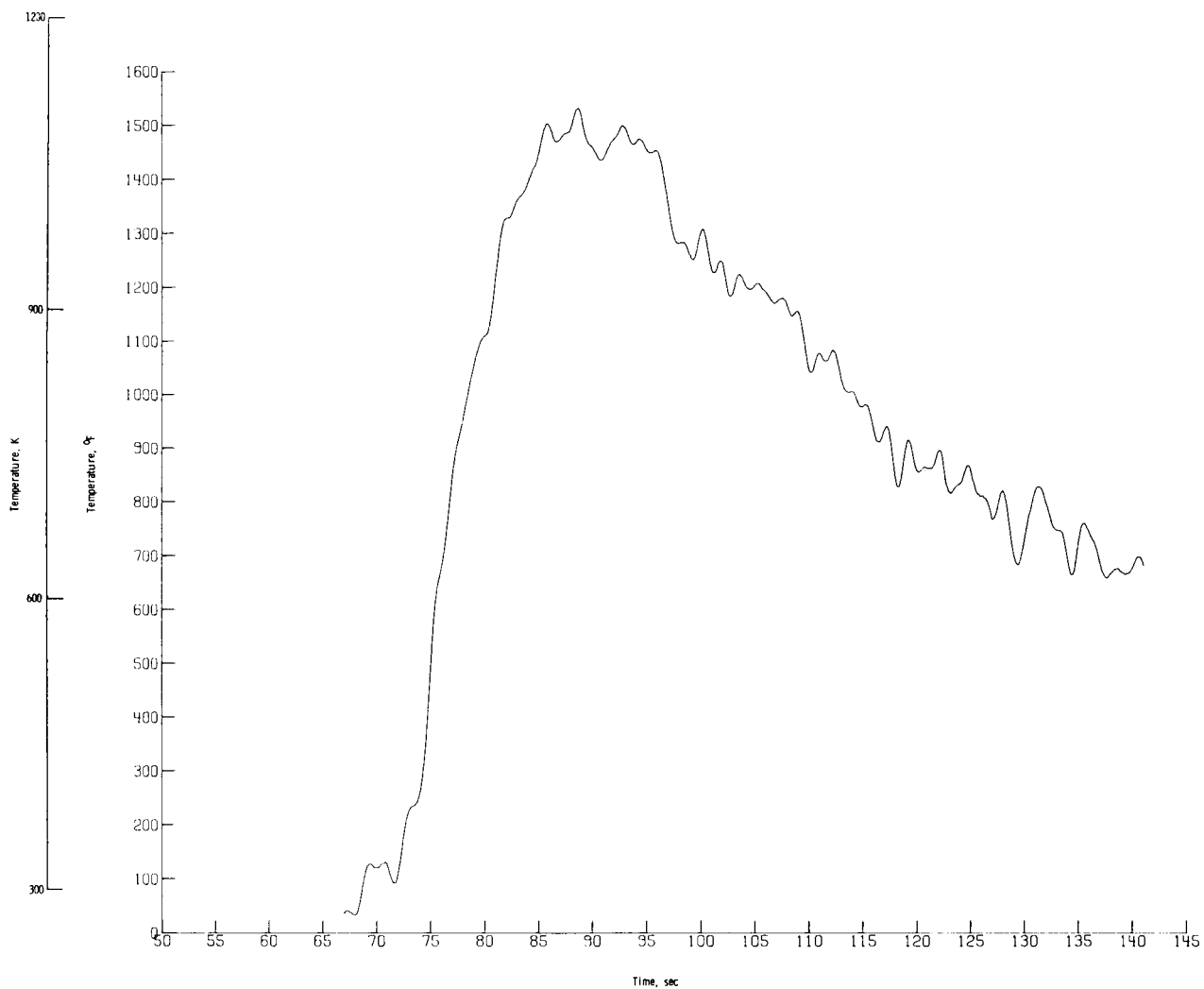
(i) Thermocouple N9.

Figure 19.- Continued.



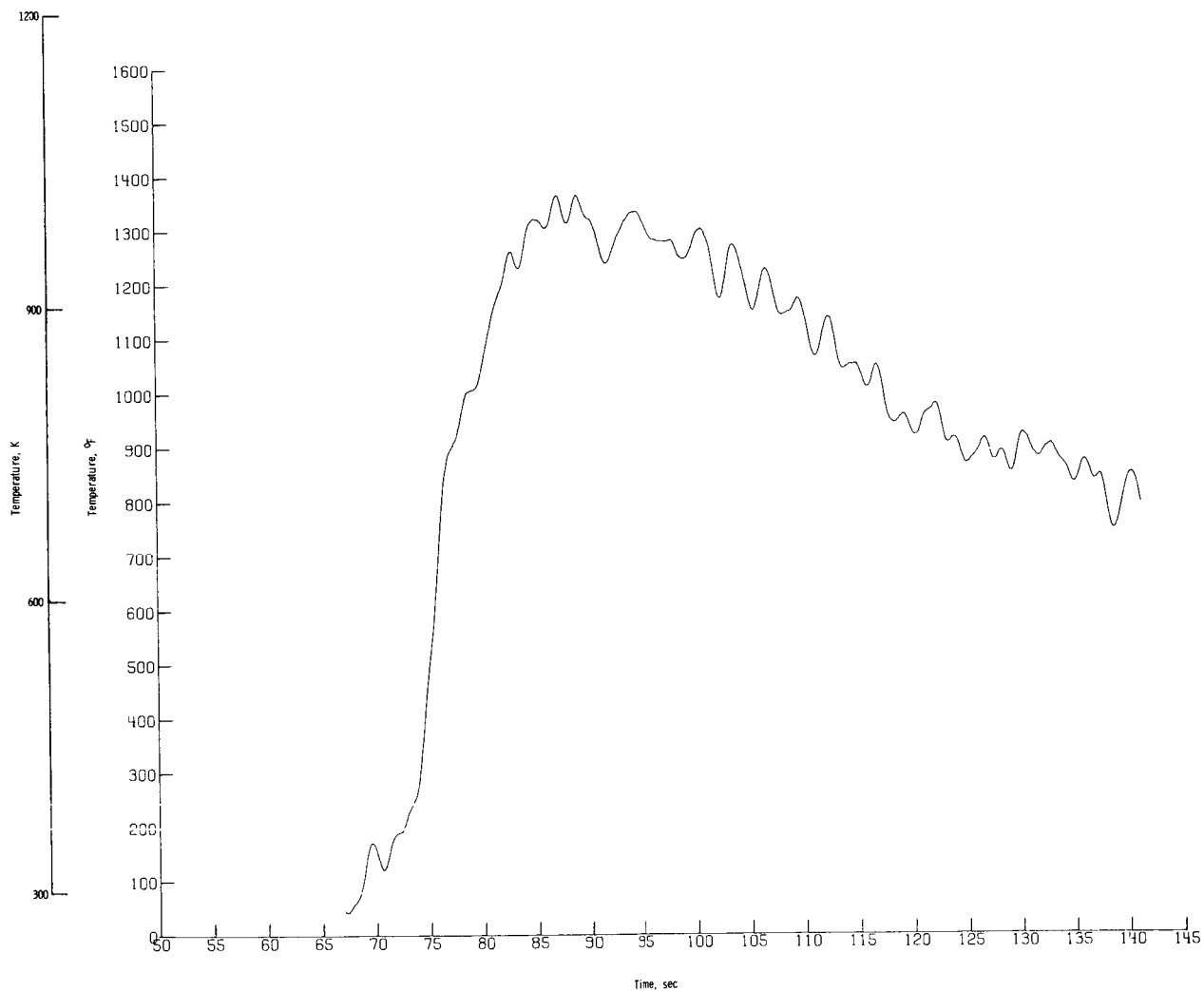
(j) Thermocouple N10.

Figure 19.- Continued.



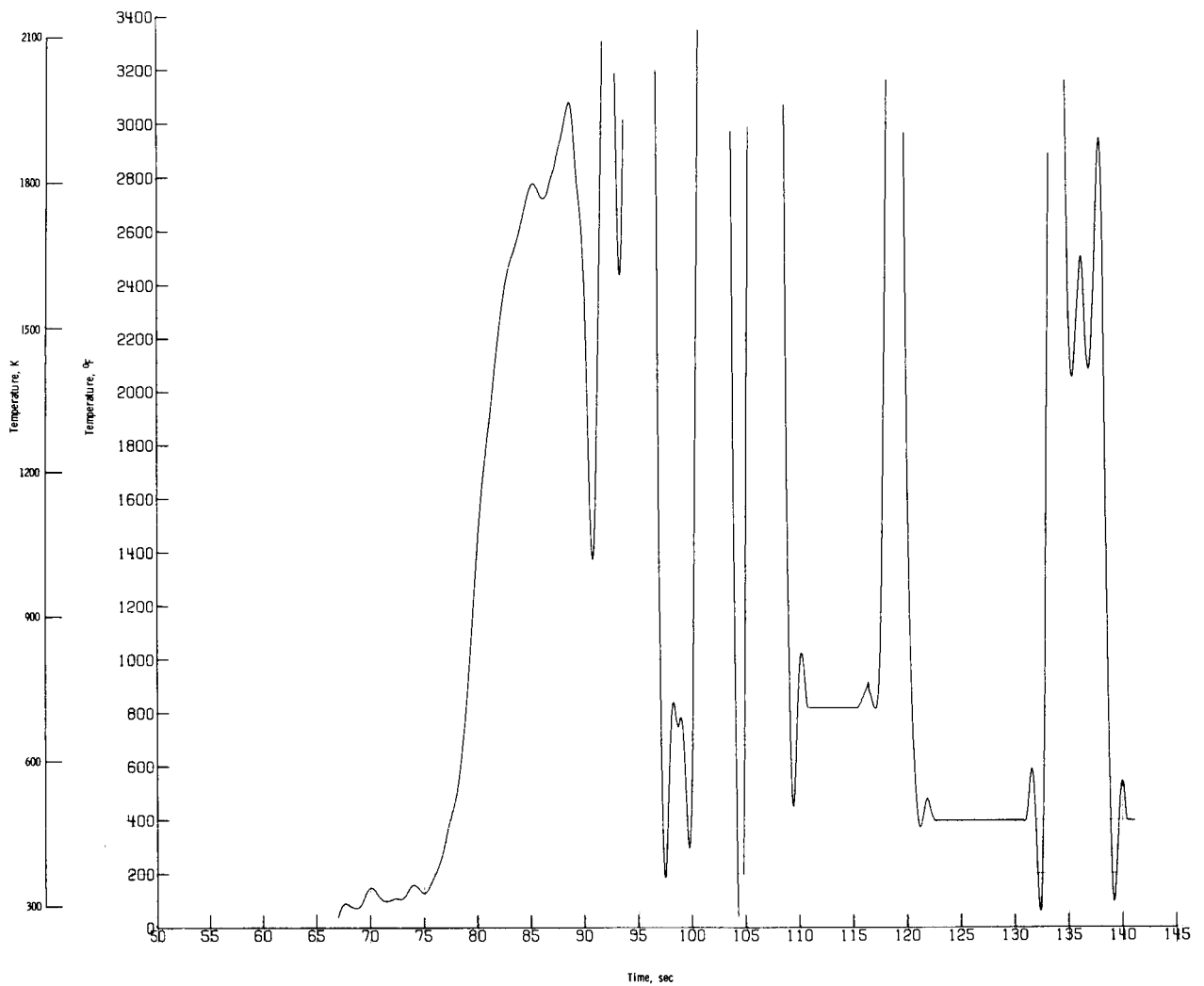
(k) Thermocouple N12.

Figure 19.- Continued.



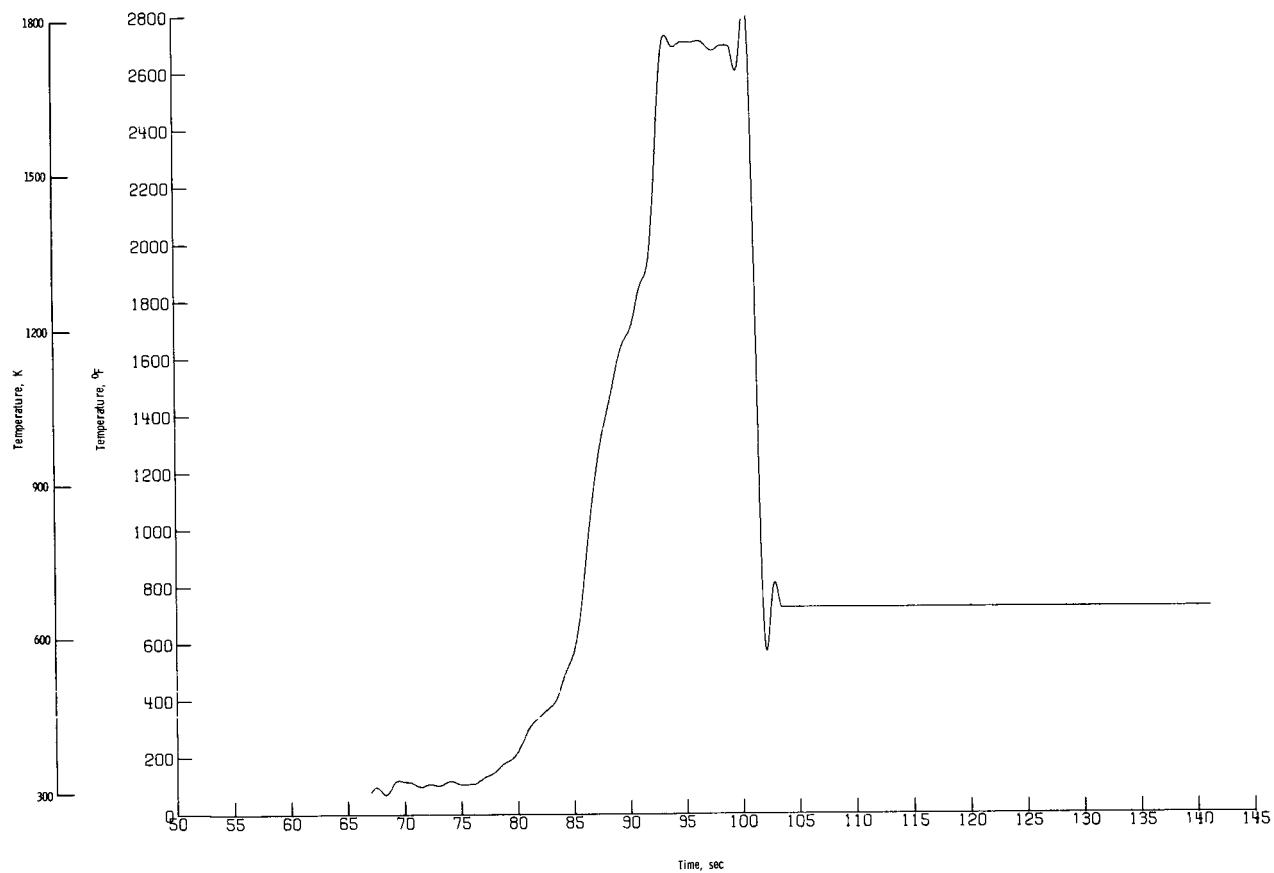
(1) Thermocouple N14.

Figure 19.- Concluded.



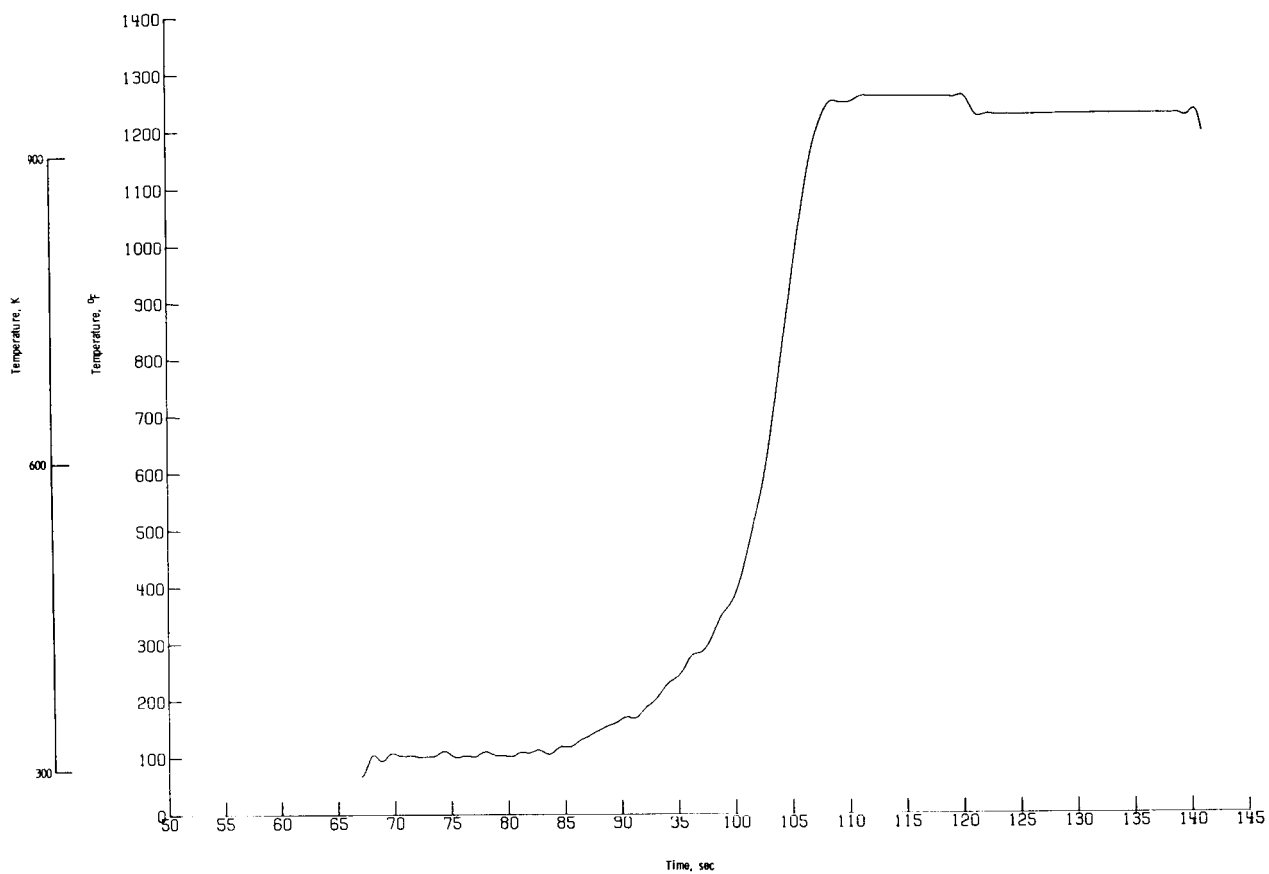
(a) Thermocouple P1-1.

Figure 20.- Measured temperature histories obtained from in-depth thermocouples.



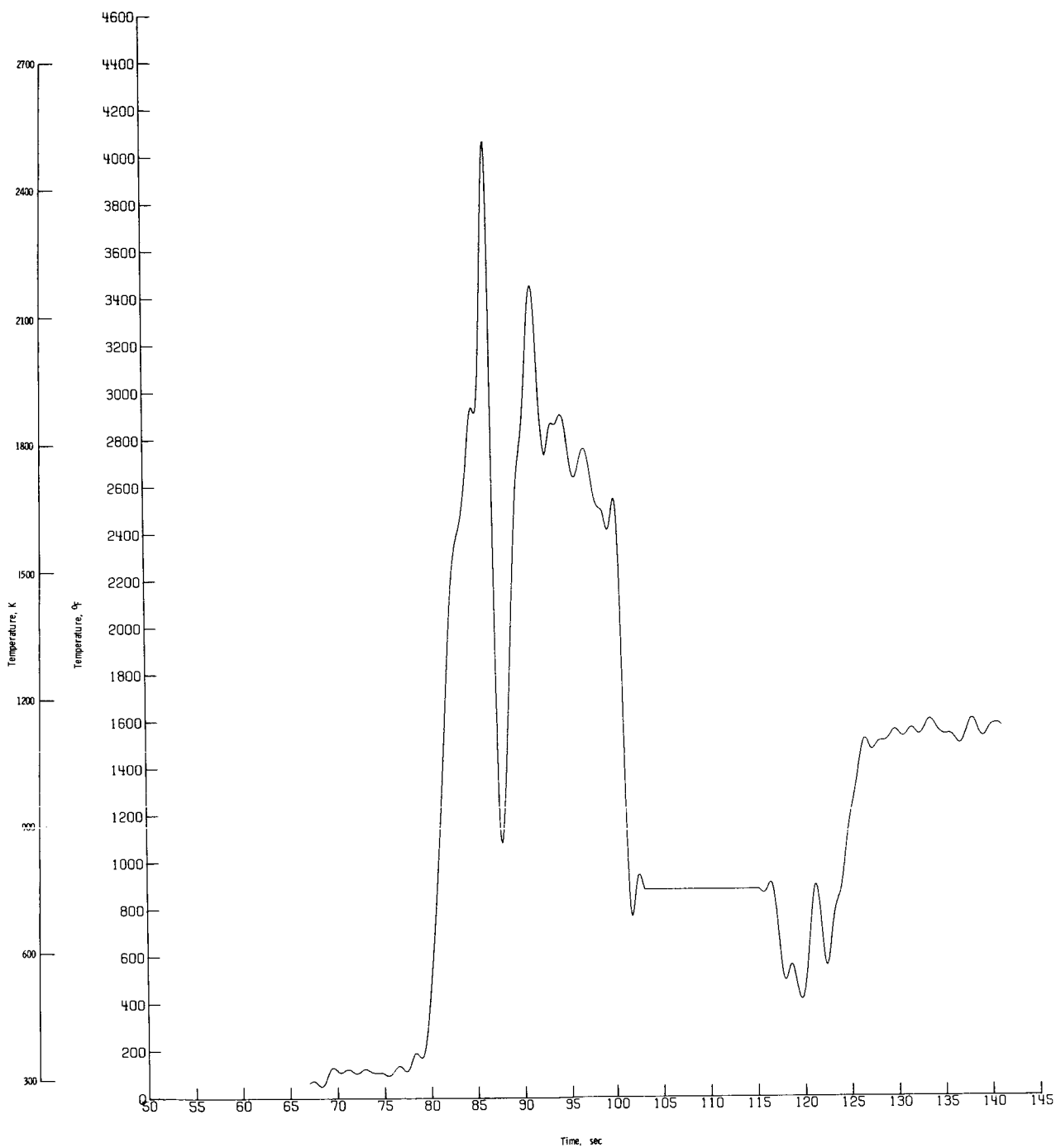
(b) Thermocouple P1-2.

Figure 20.- Continued.



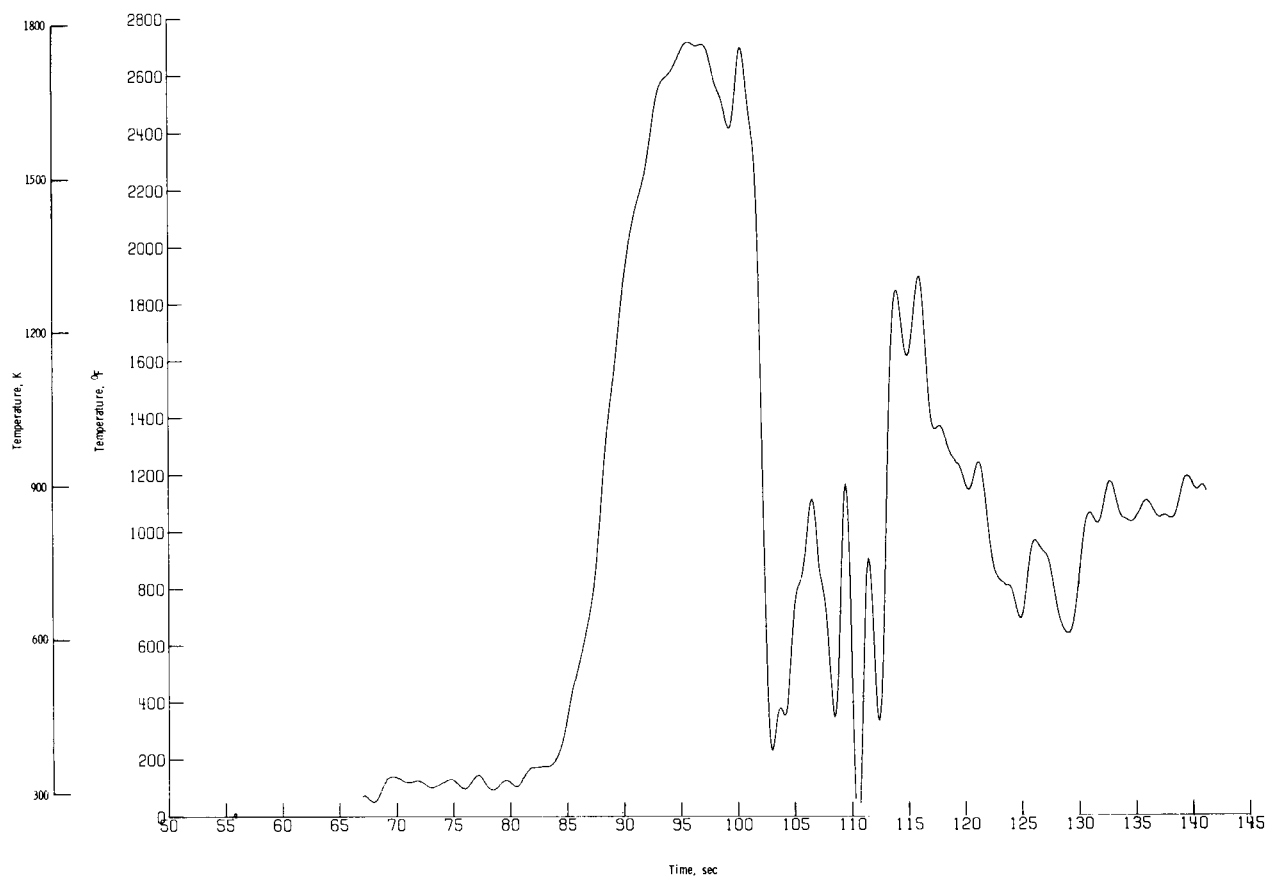
(c) Thermocouple P1-3.

Figure 20.- Continued.



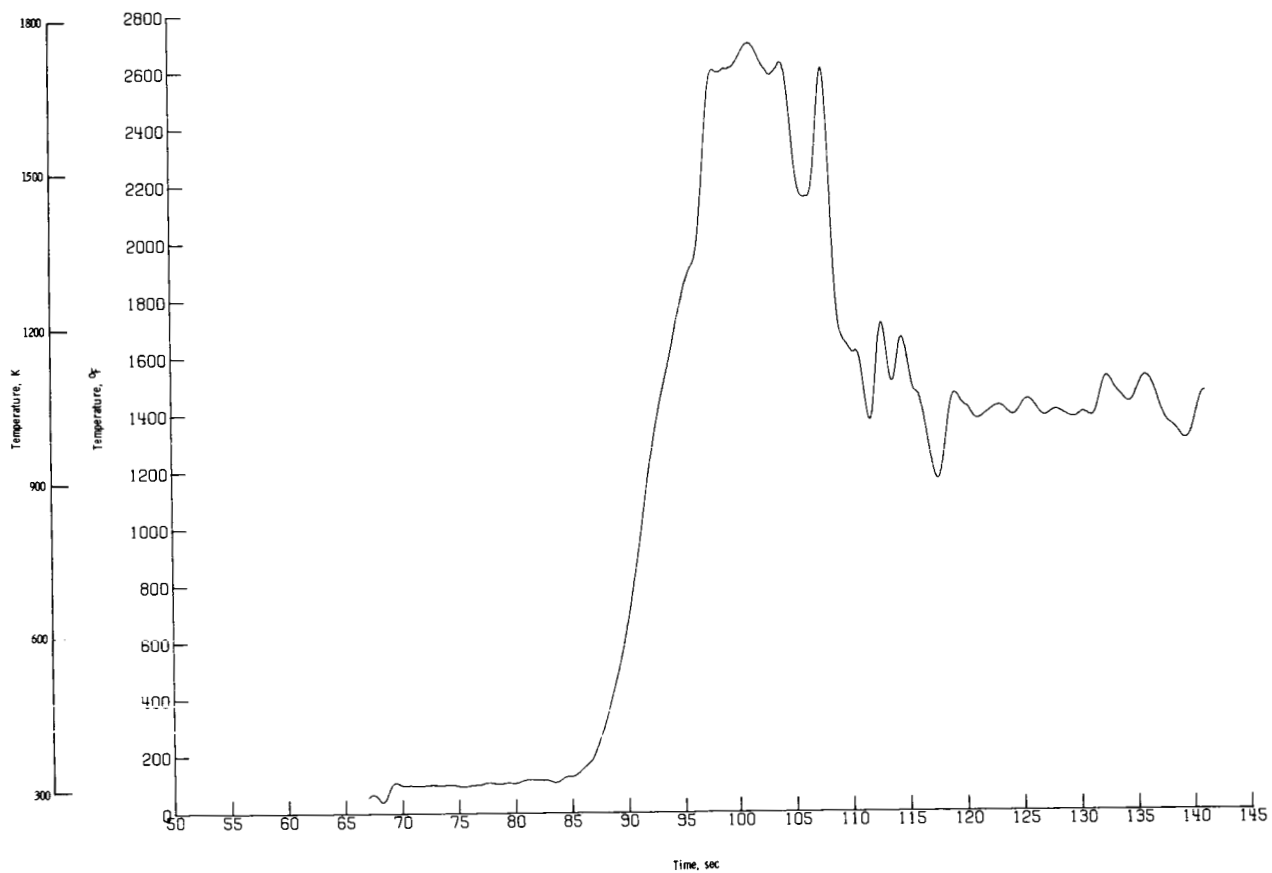
(d) Thermocouple P2-1.

Figure 20.- Continued.



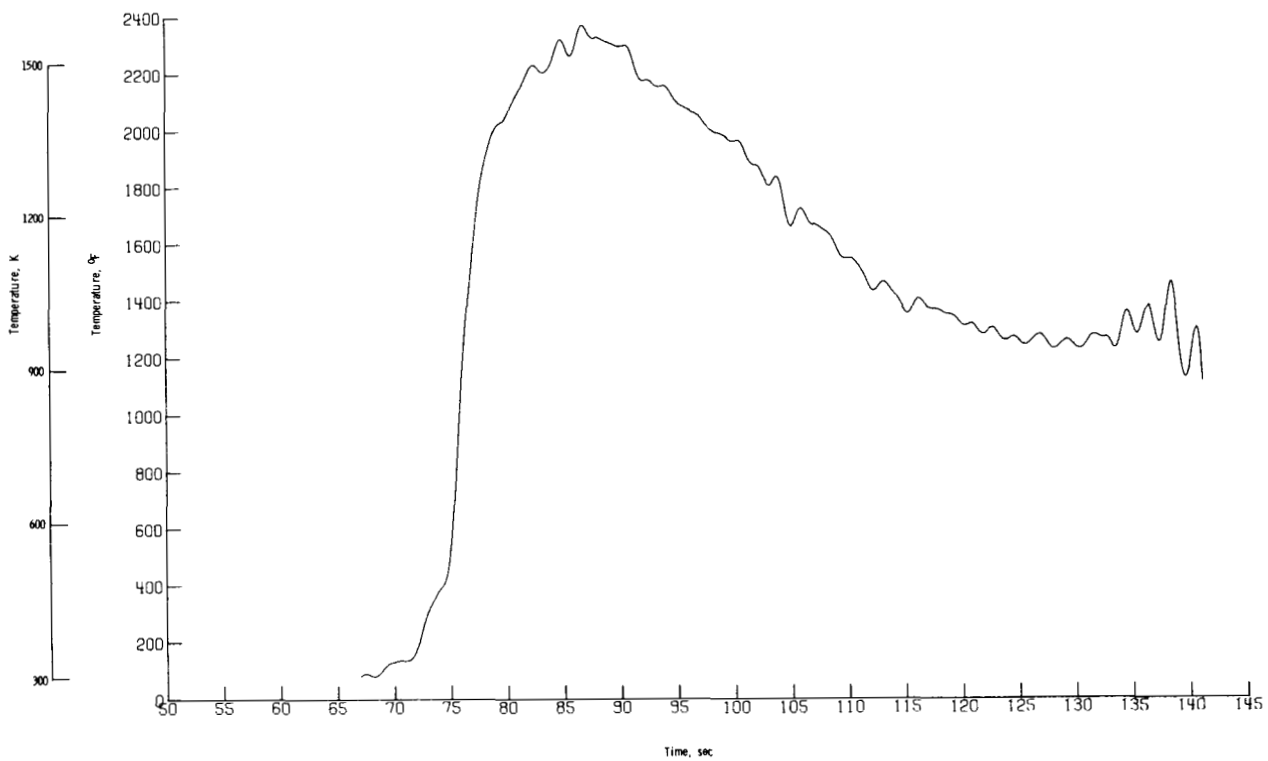
(e) Thermocouple P2-2.

Figure 20. - Continued.



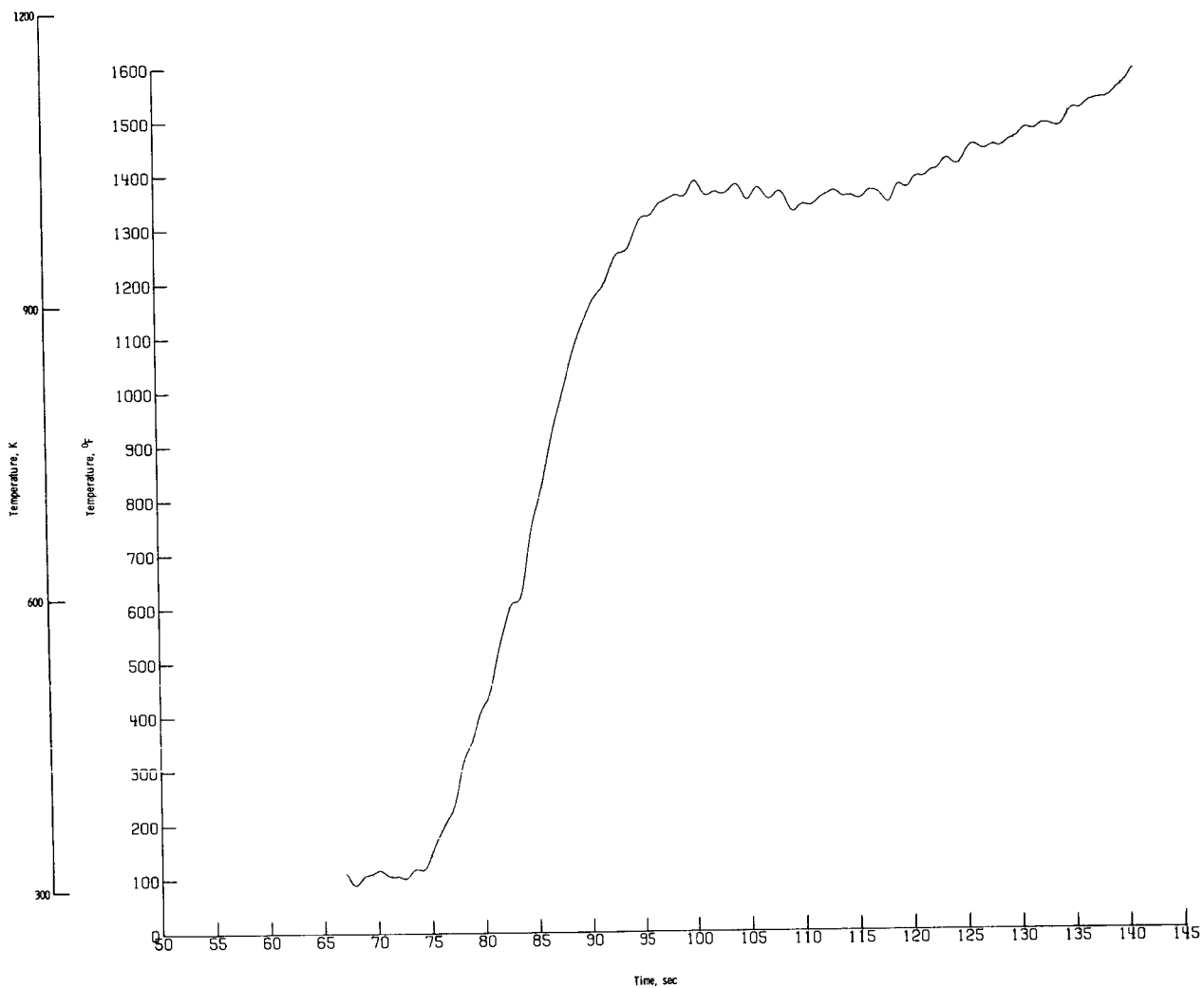
(f) Thermocouple P2-3.

Figure 20. - Continued.



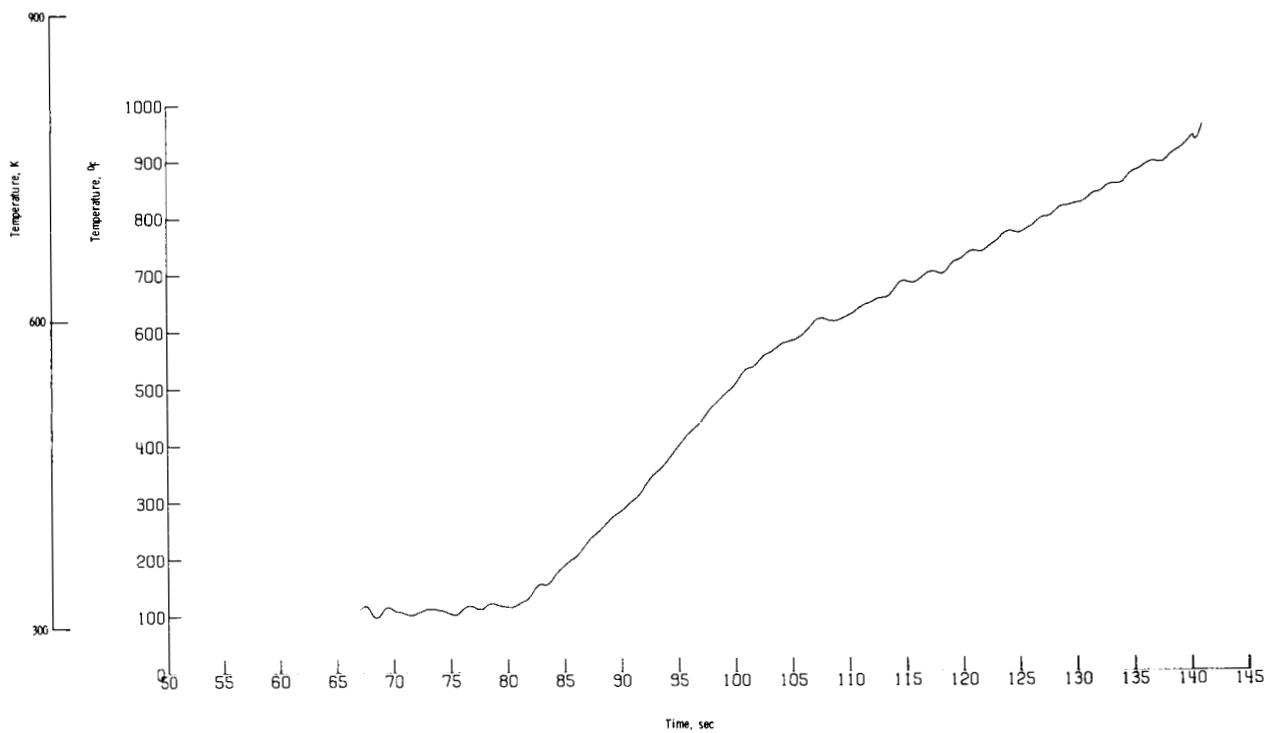
(g) Thermocouple P3-1.

Figure 20. - Continued.



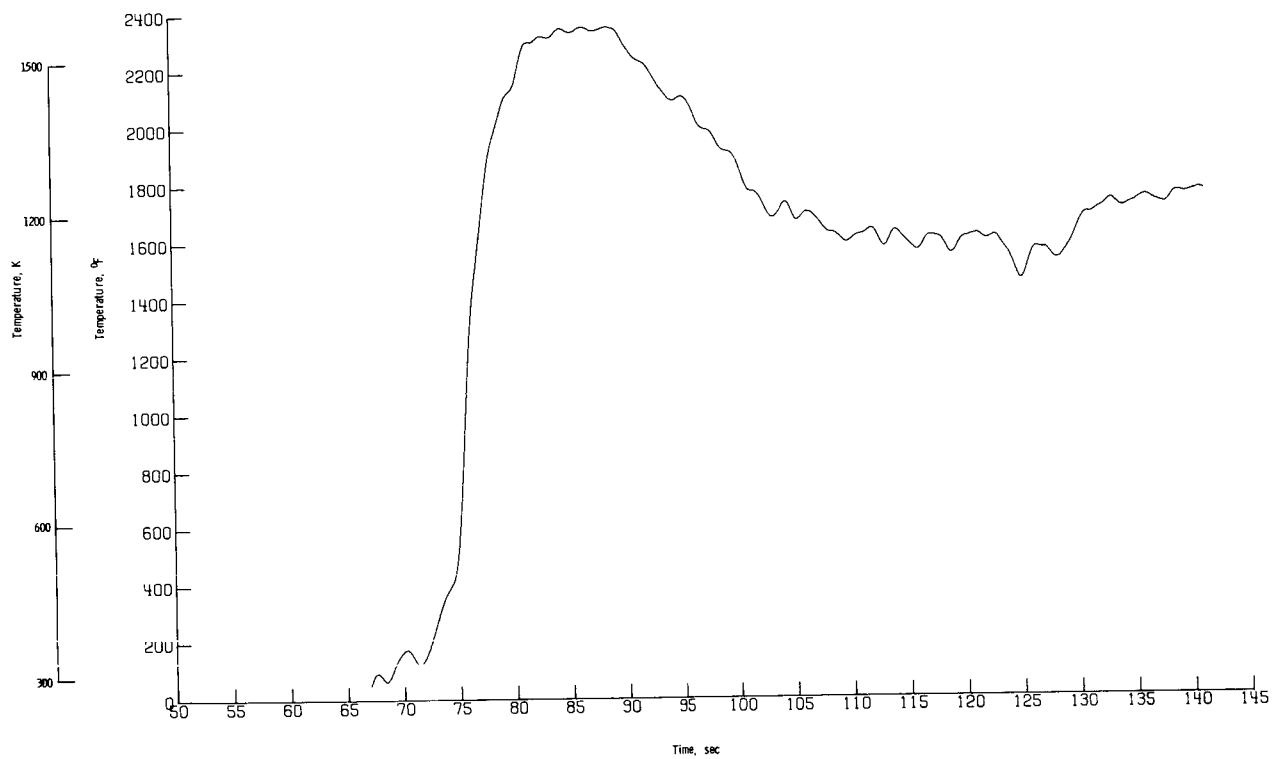
(h) Thermocouple P3-2.

Figure 20.- Continued.



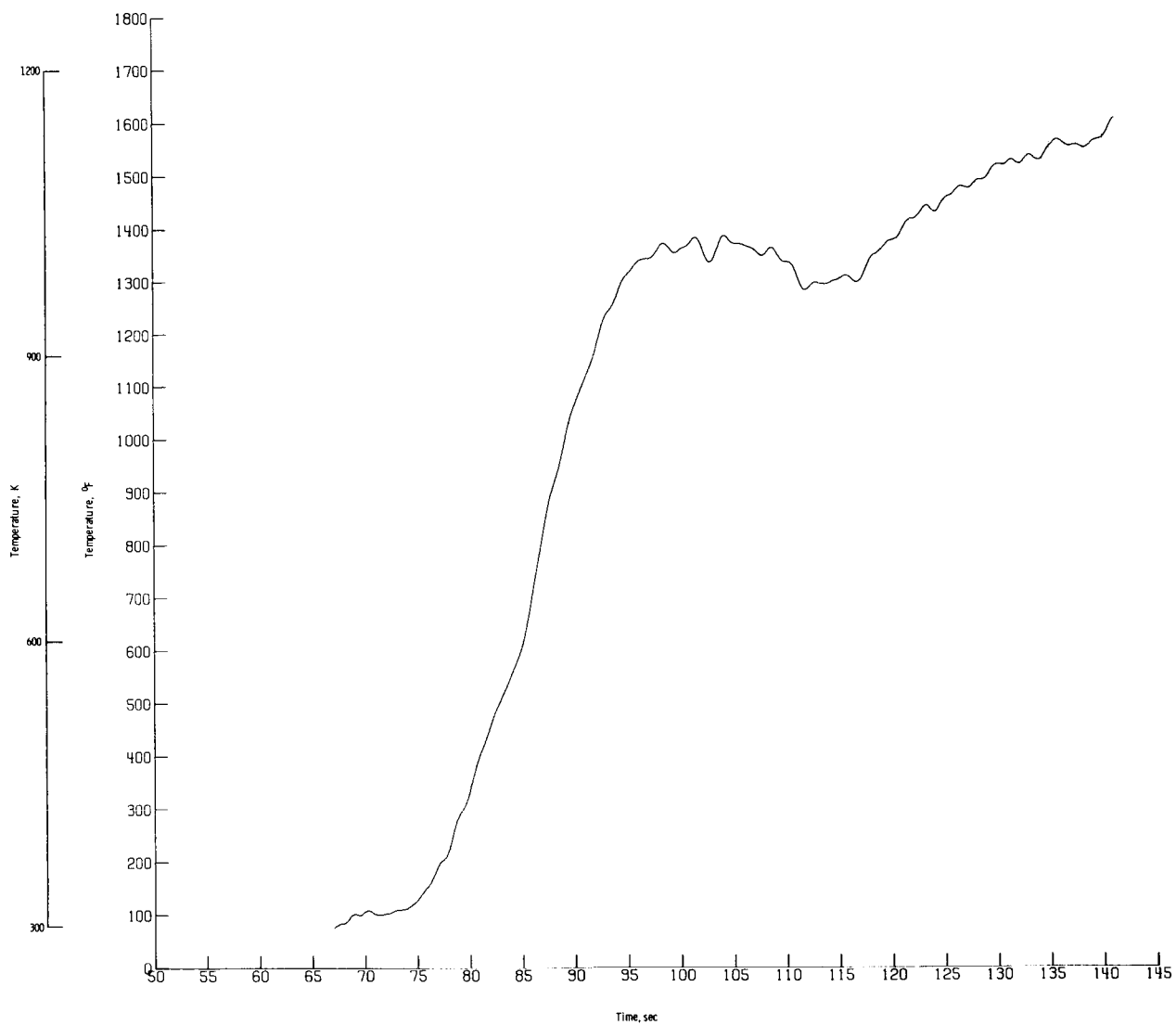
(i) Thermocouple P3-3.

Figure 20.- Continued.



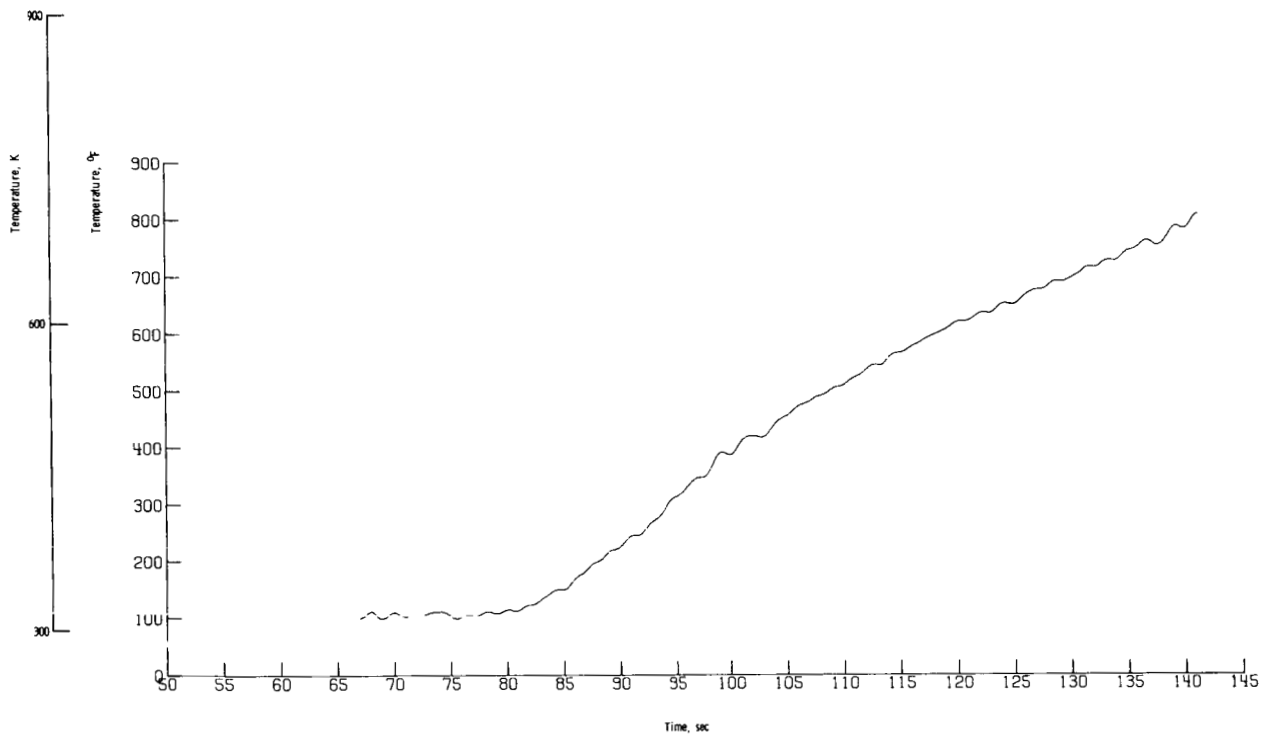
(j) Thermocouple P4-1.

Figure 20. - Continued.



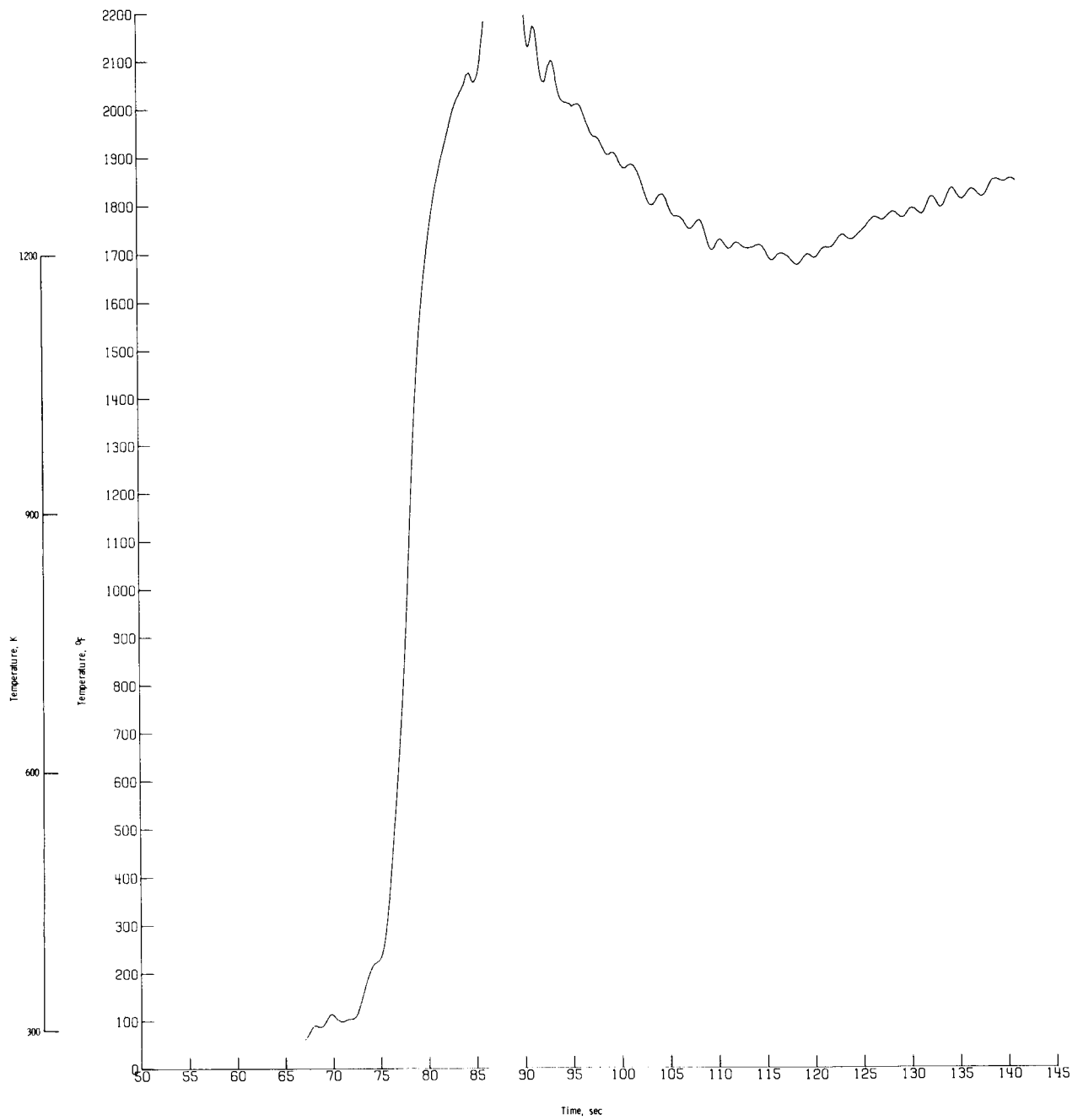
(k) Thermocouple P4-2.

Figure 20. - Continued.



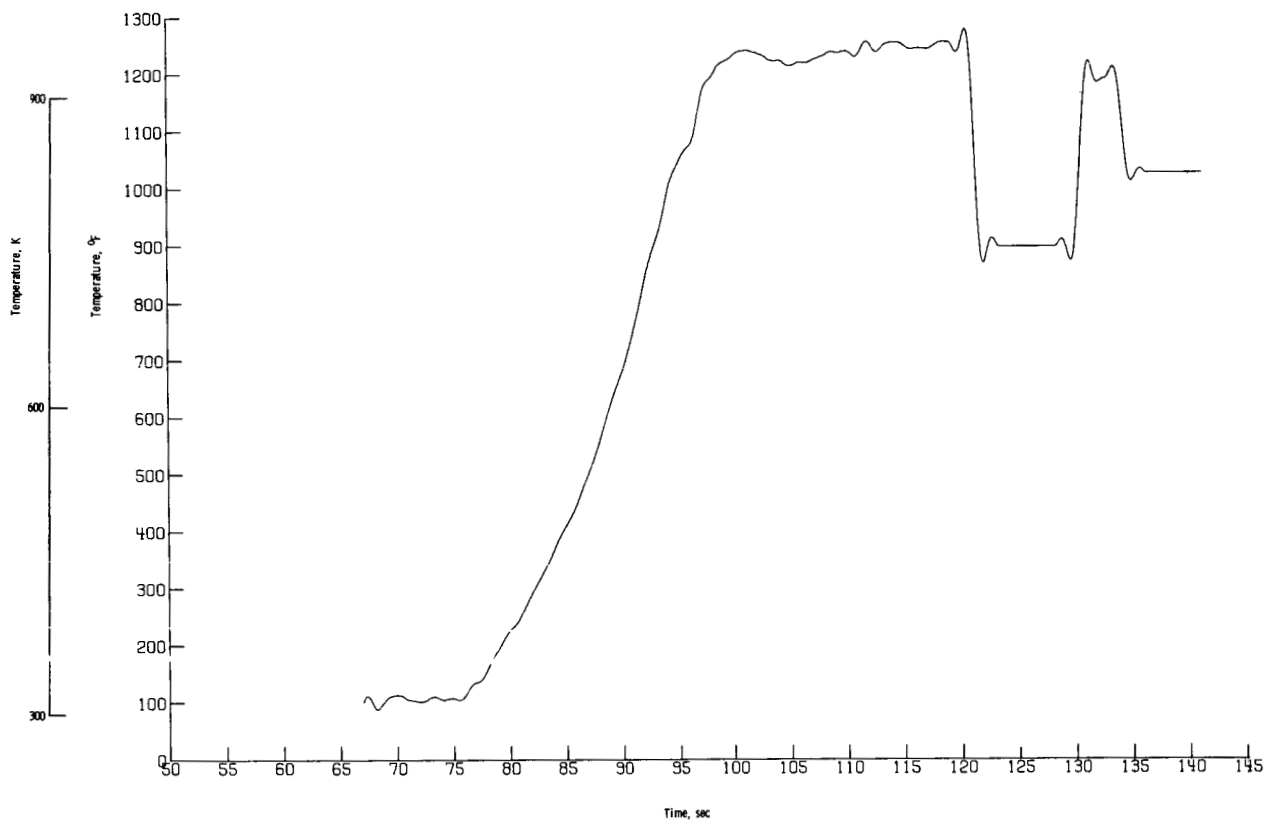
(1) Thermocouple P4-3.

Figure 20.- Continued.



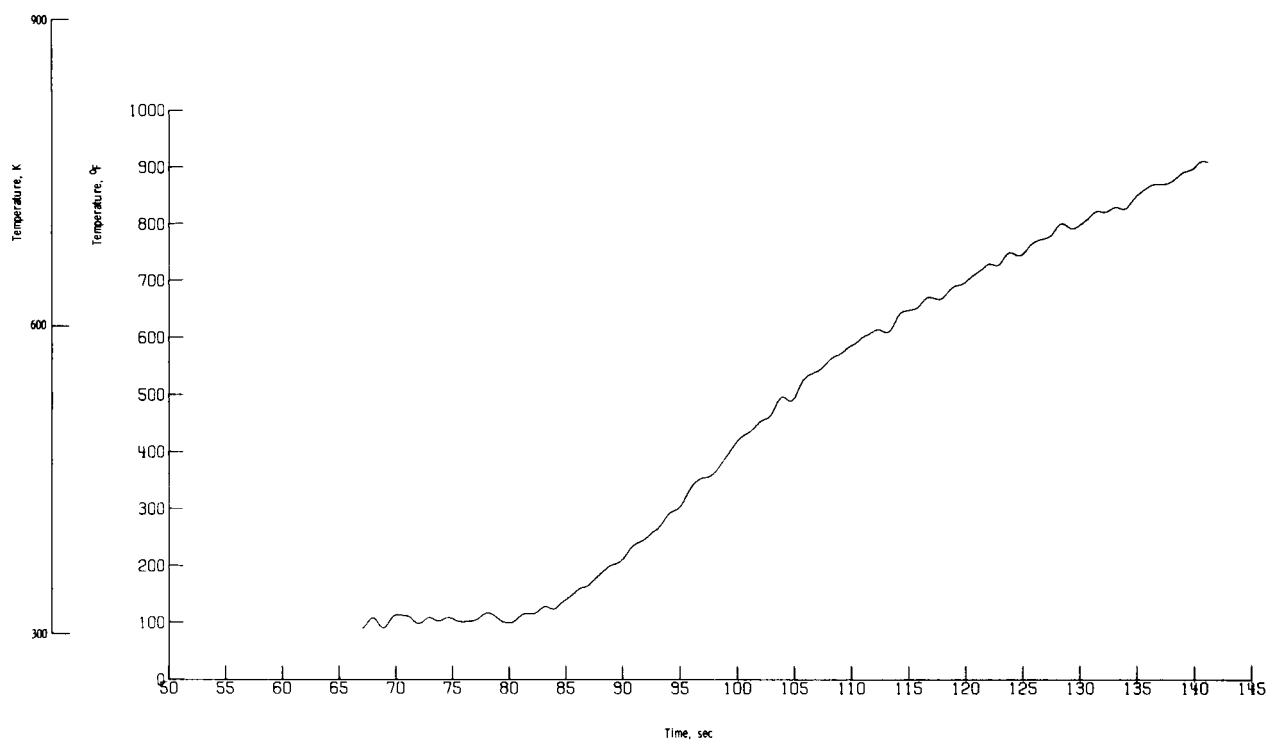
(m) Thermocouple P5-1.

Figure 20.- Continued.



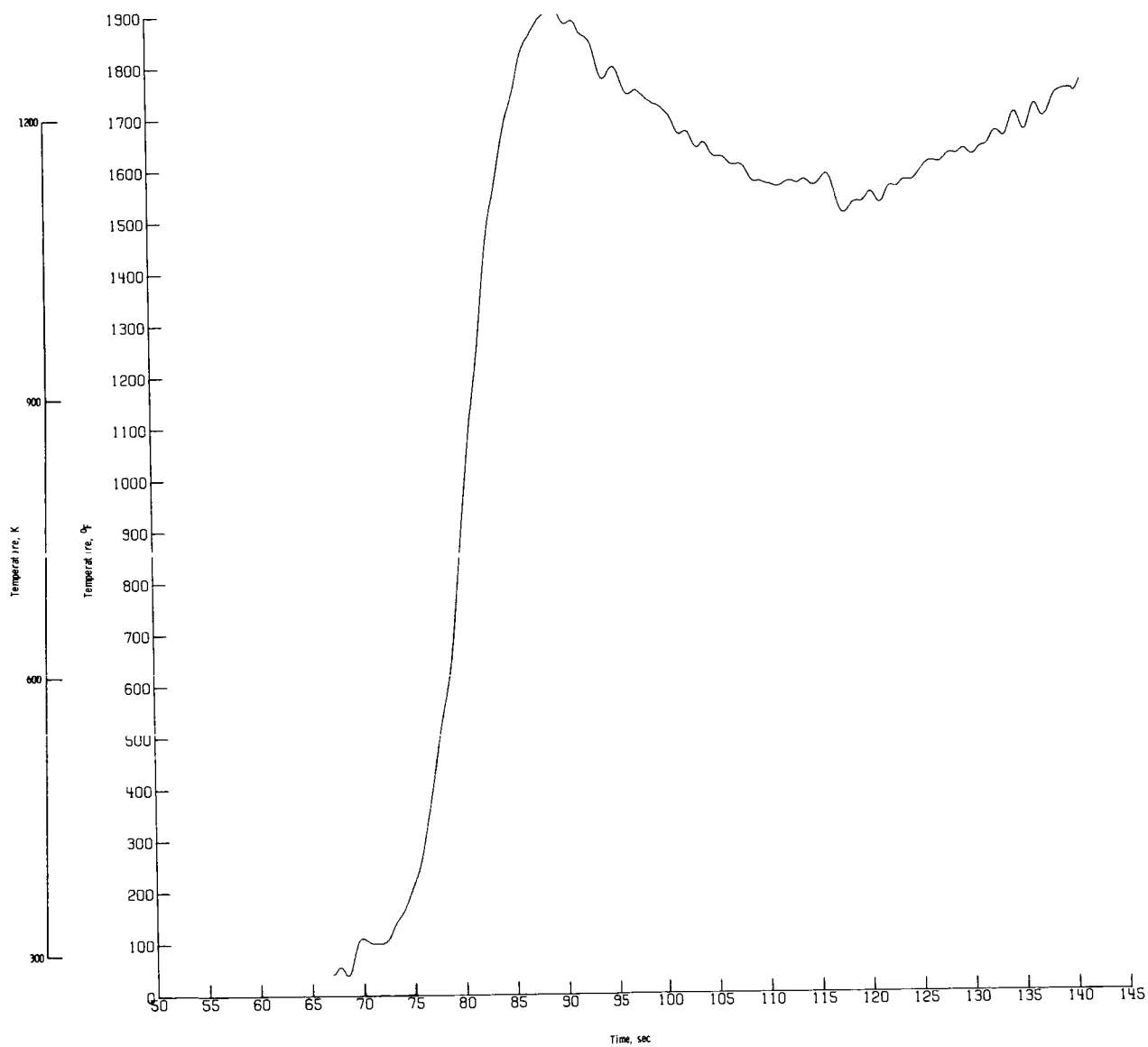
(n) Thermocouple P5-2.

Figure 20.- Continued.



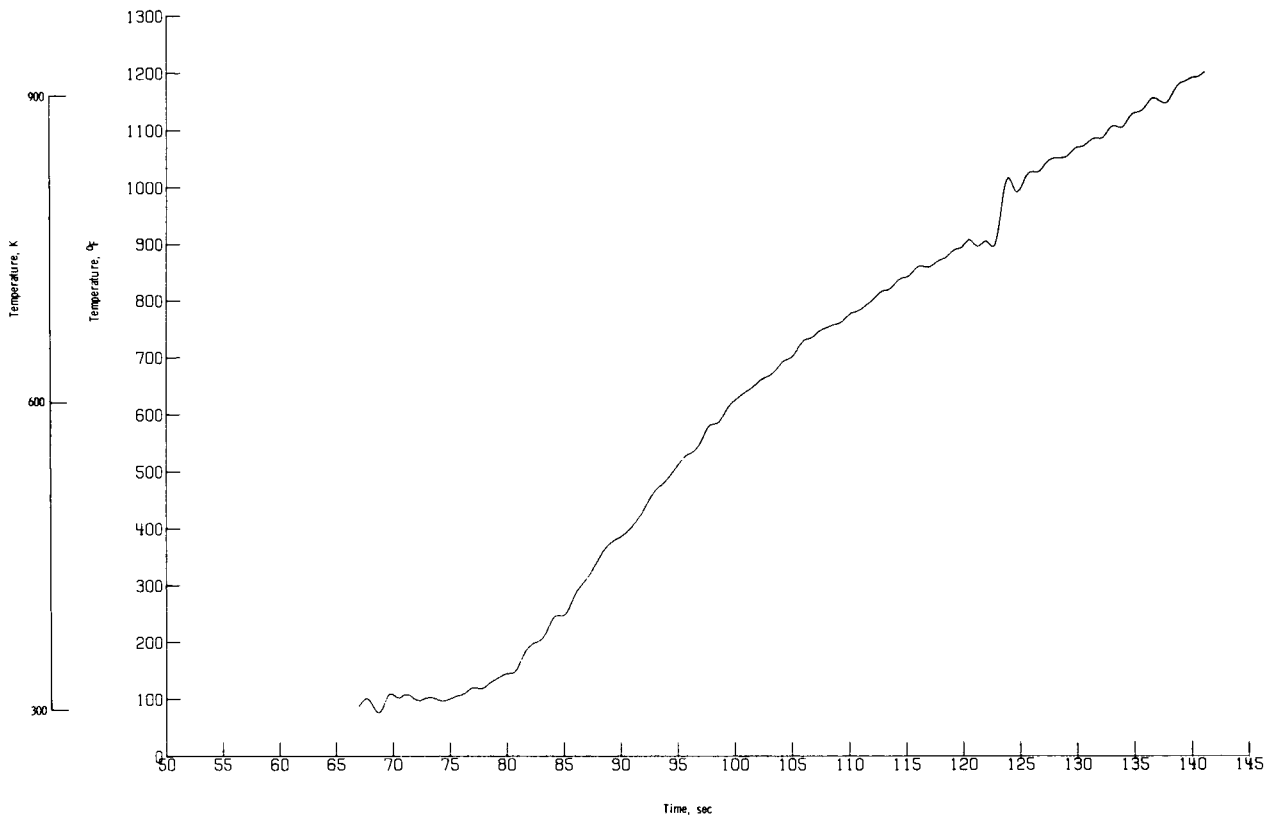
(o) Thermocouple P5-3.

Figure 20.- Continued.



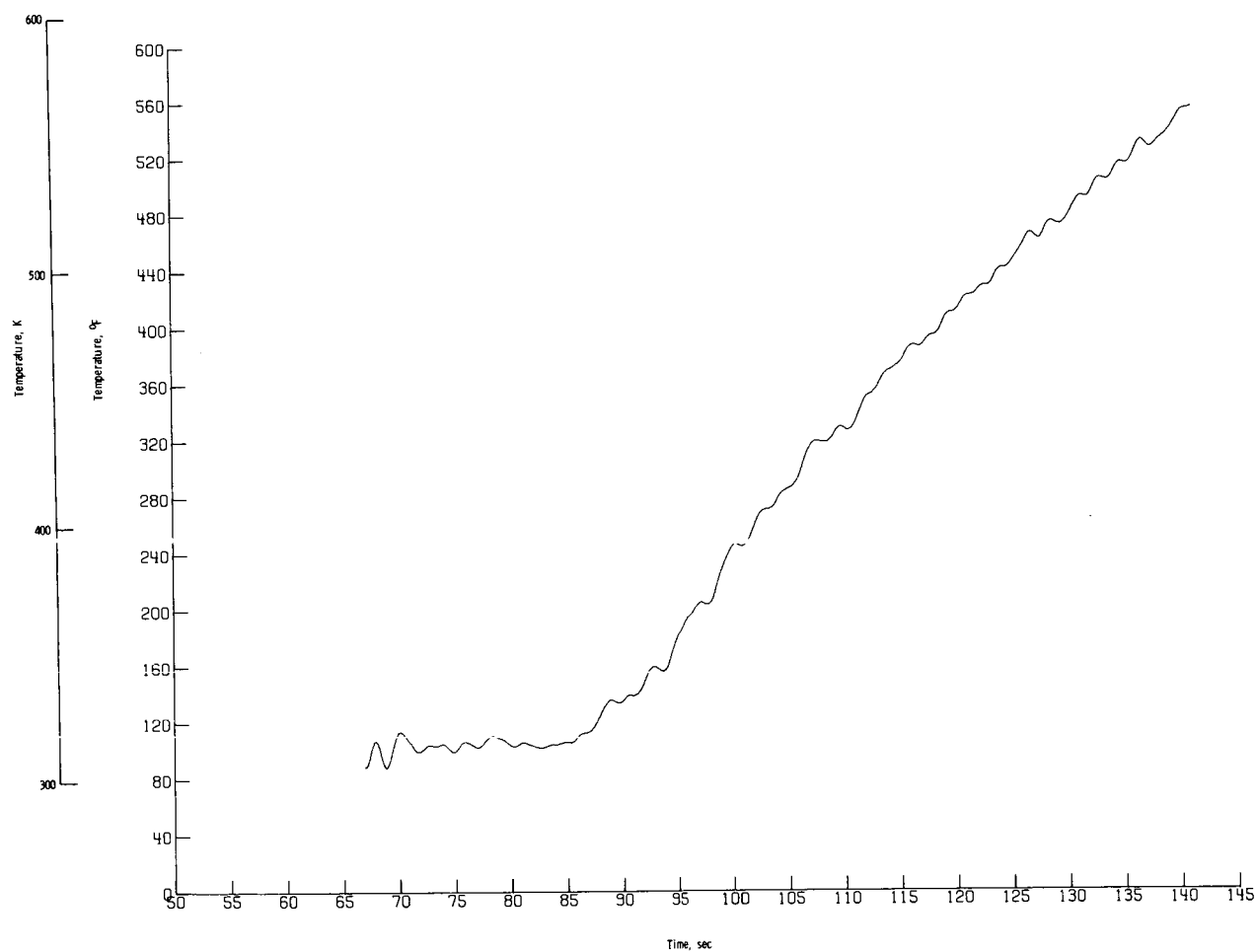
(p) Thermocouple P6-1.

Figure 20.- Continued.



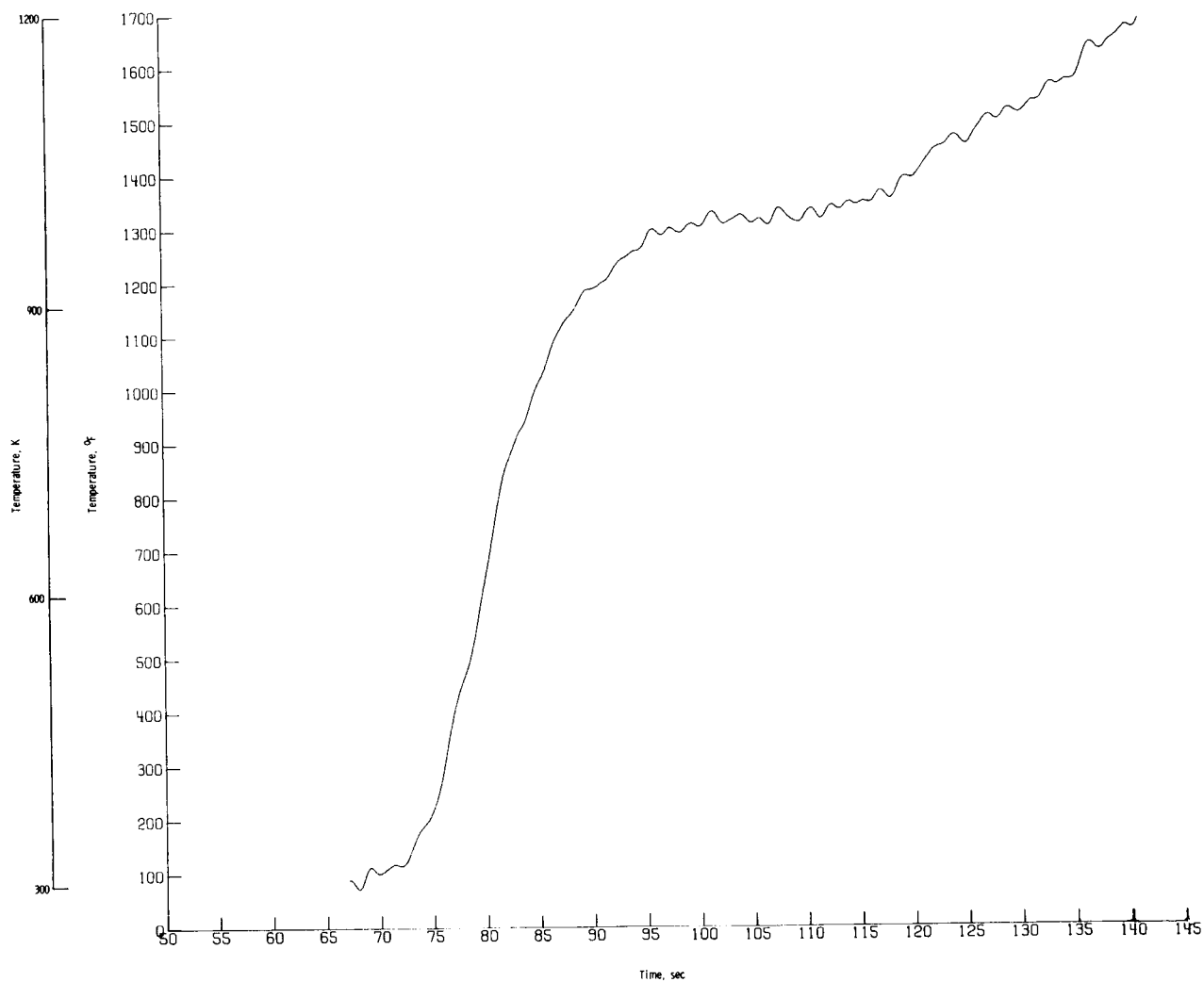
(q) Thermocouple P6-2.

Figure 20.- Continued.



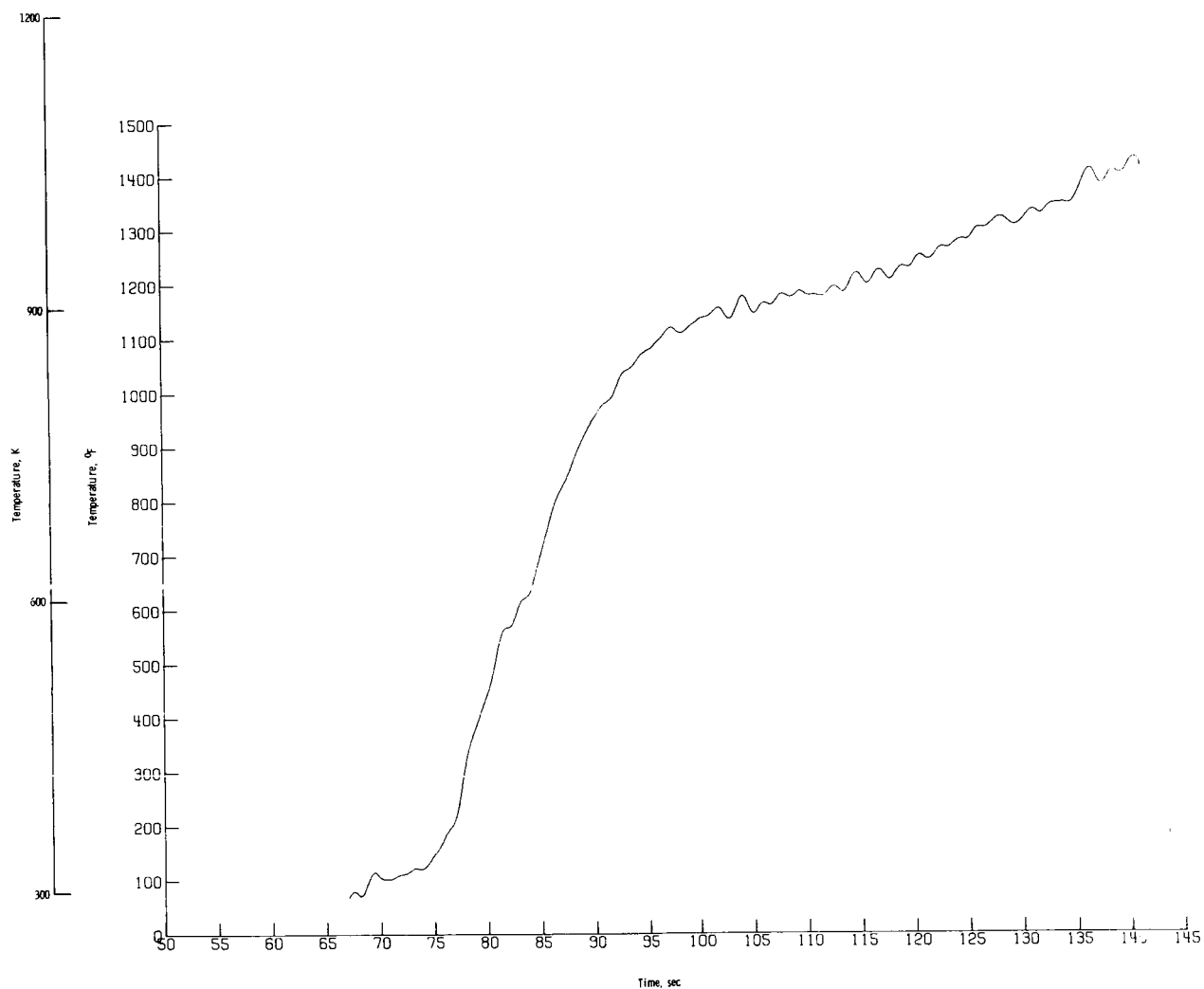
(r) Thermocouple P6-3.

Figure 20.- Continued.



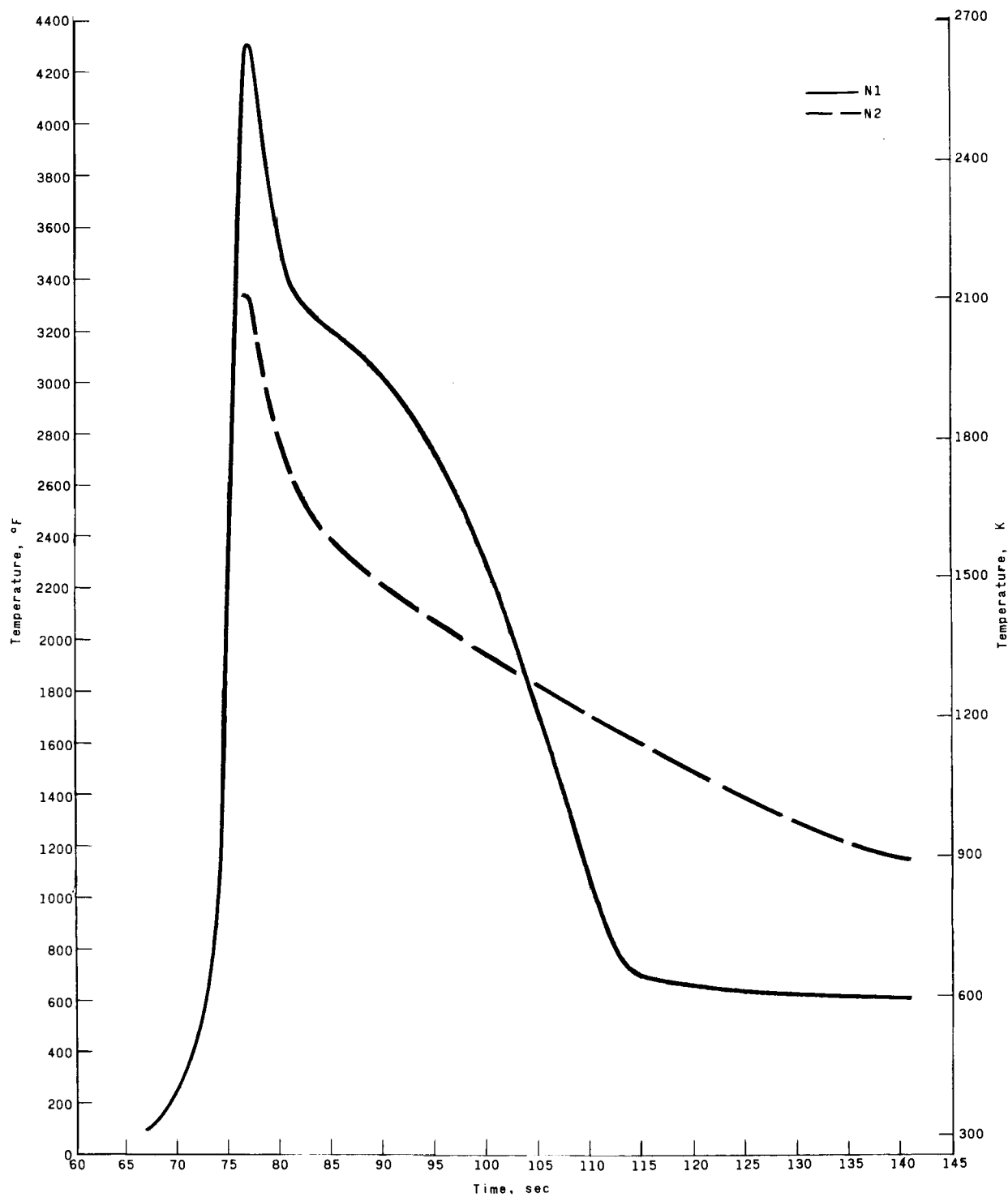
(s) Thermocouple P7-1.

Figure 20.- Continued.



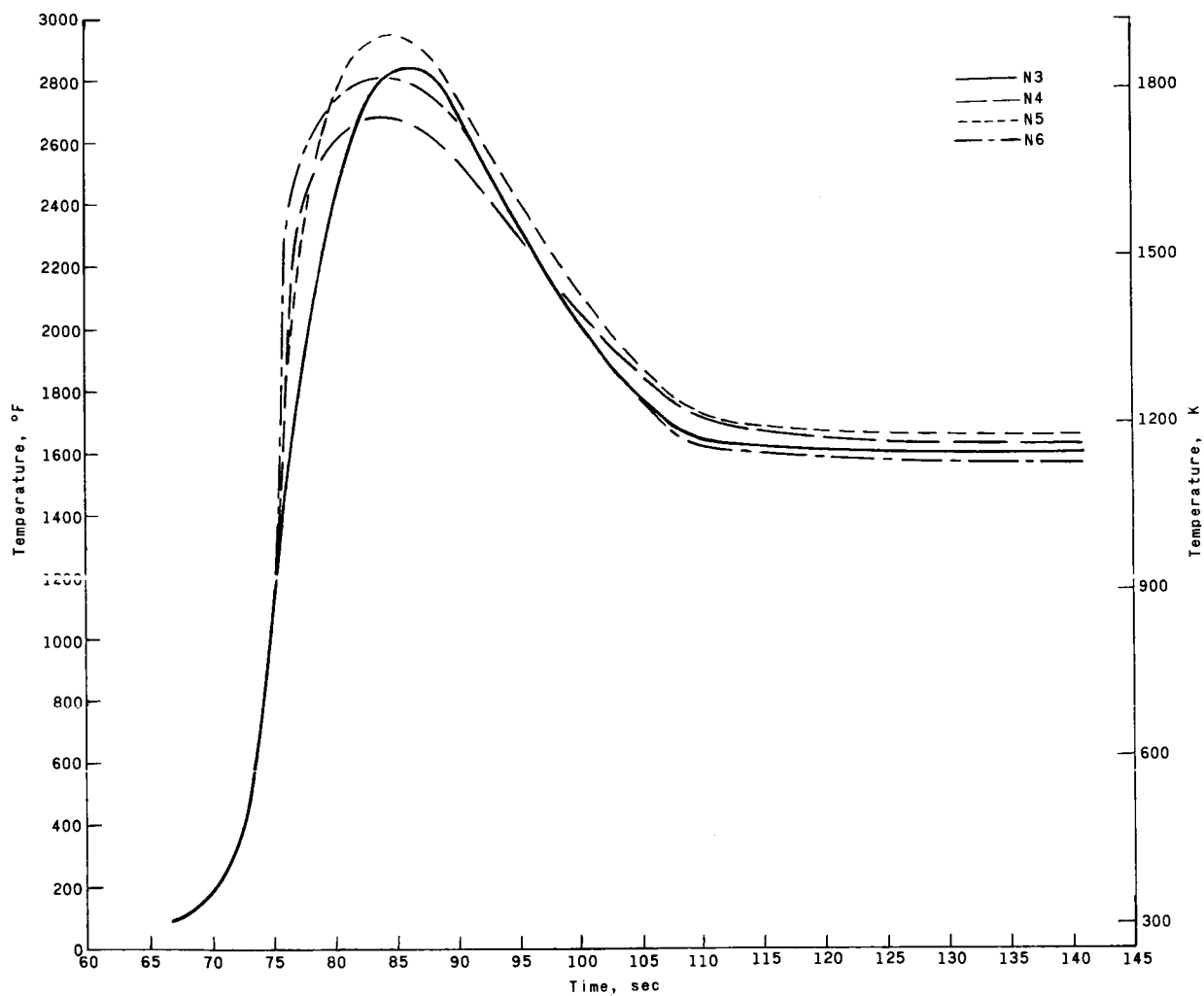
(t) Thermocouple P7-2.

Figure 20.- Concluded.



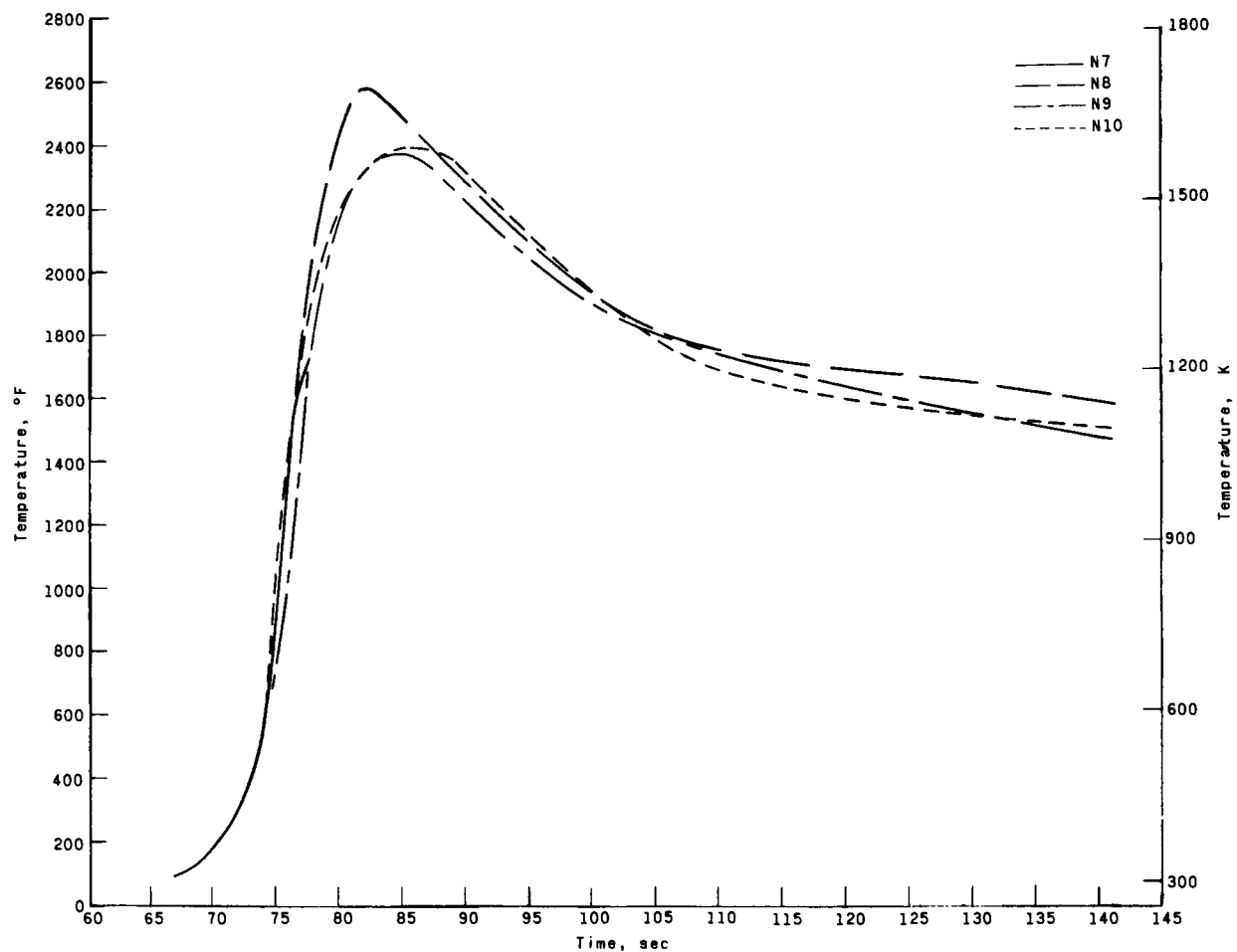
(a) Stations 45° and $67\frac{1}{2}^{\circ}$.

Figure 21.- Hand-faired surface temperature histories.



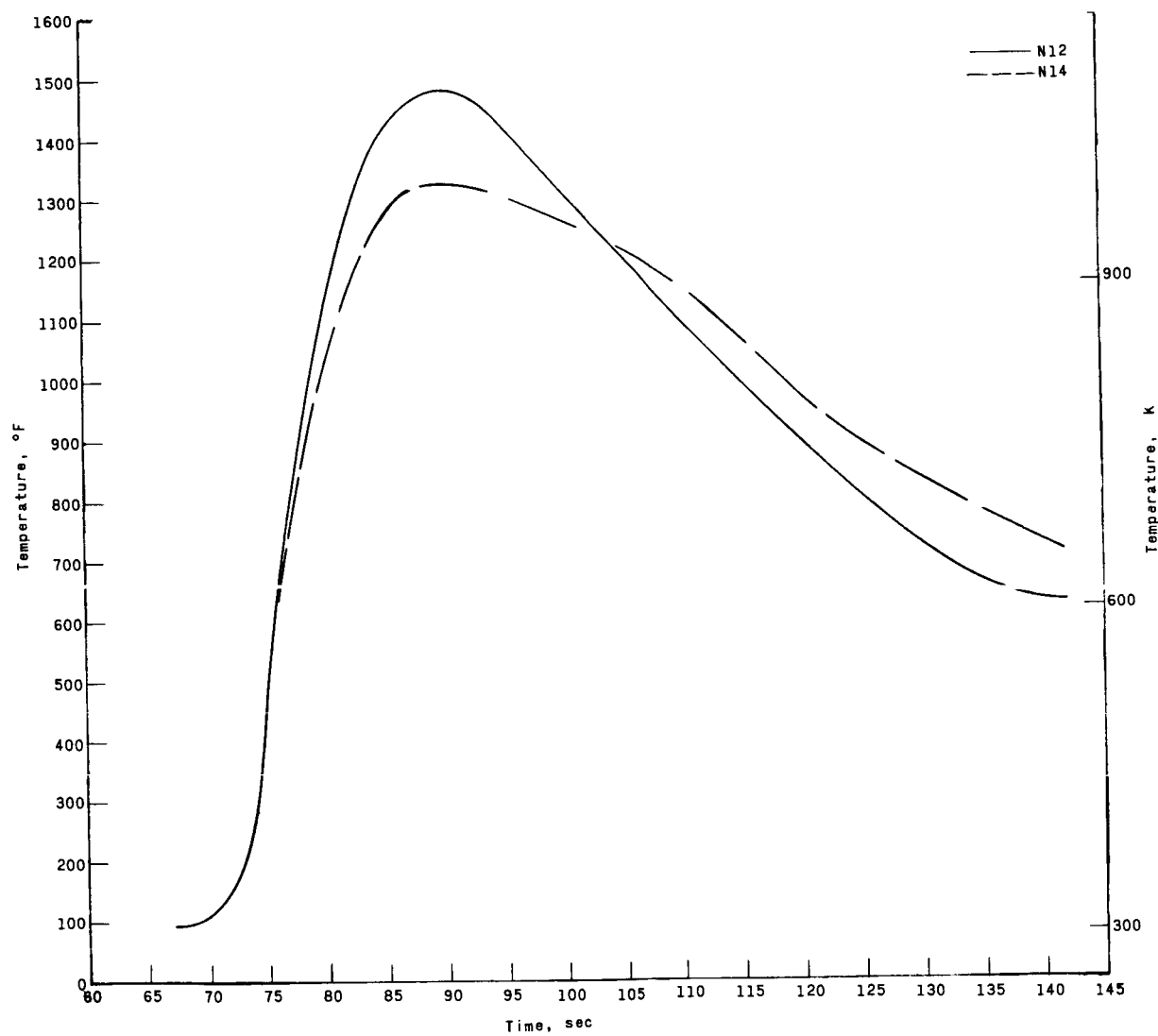
(b) Station B-B.

Figure 21.- Continued.



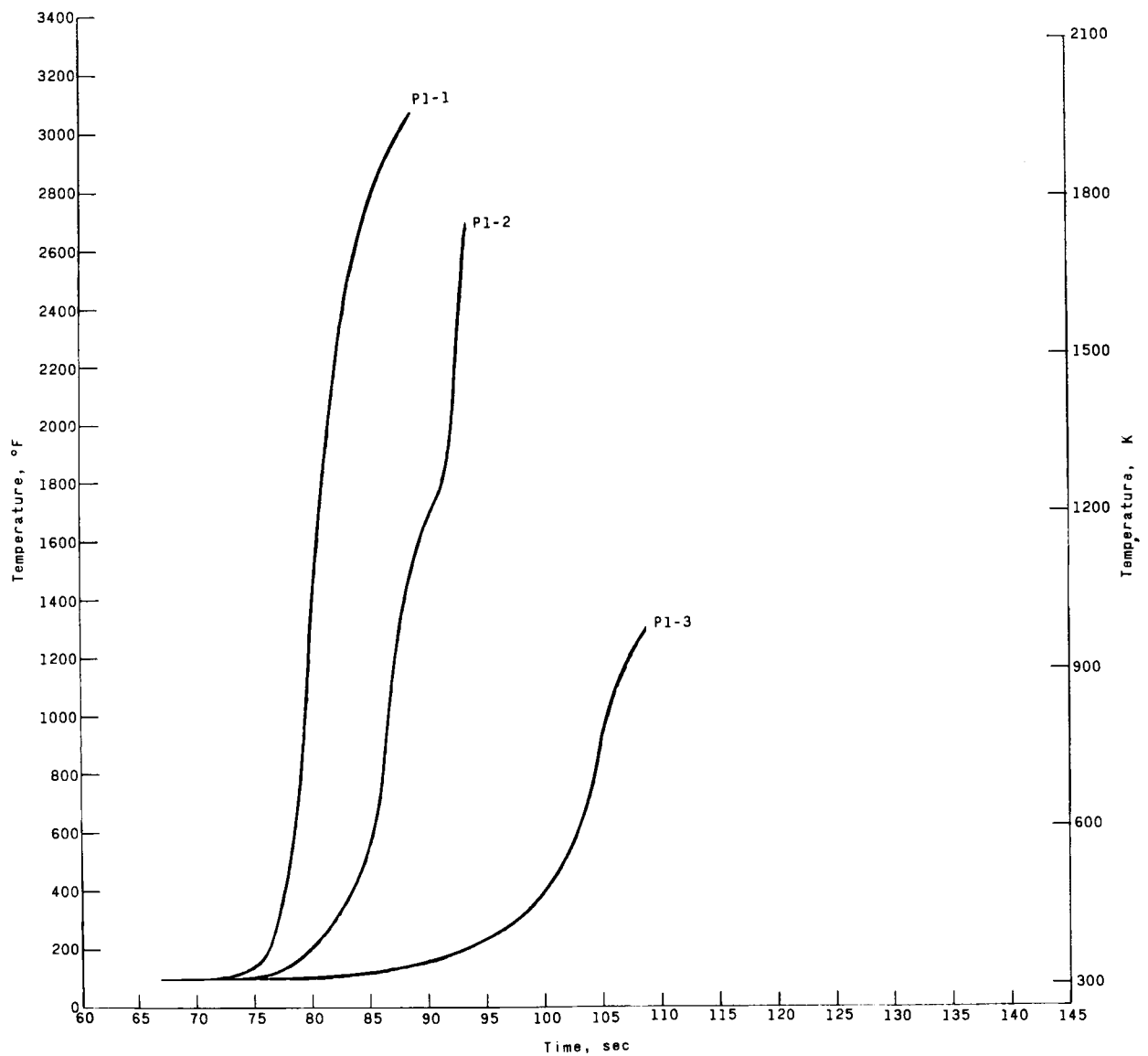
(c) Station D-D.

Figure 21. - Continued.



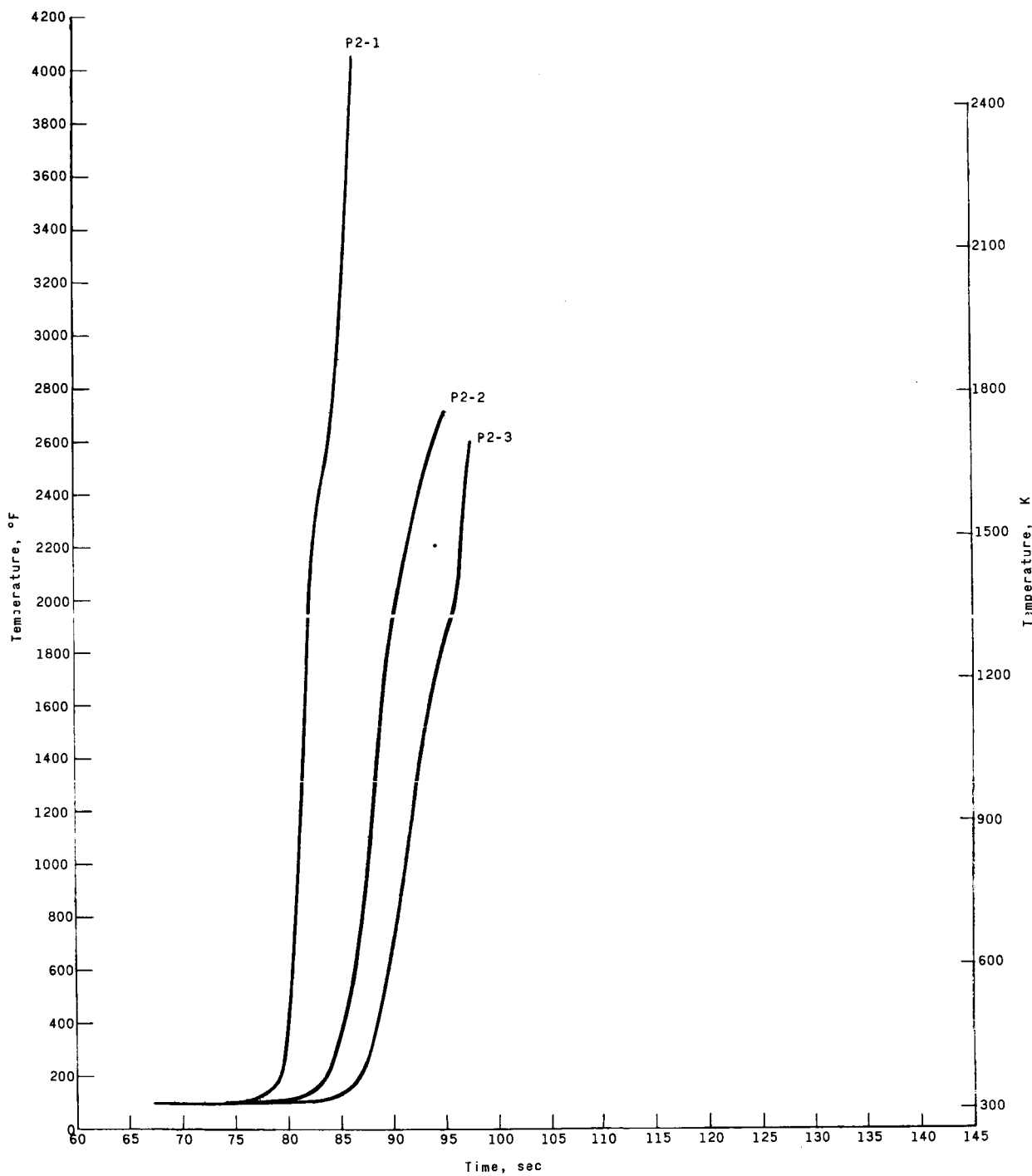
(d) Station F-F.

Figure 21.- Concluded.



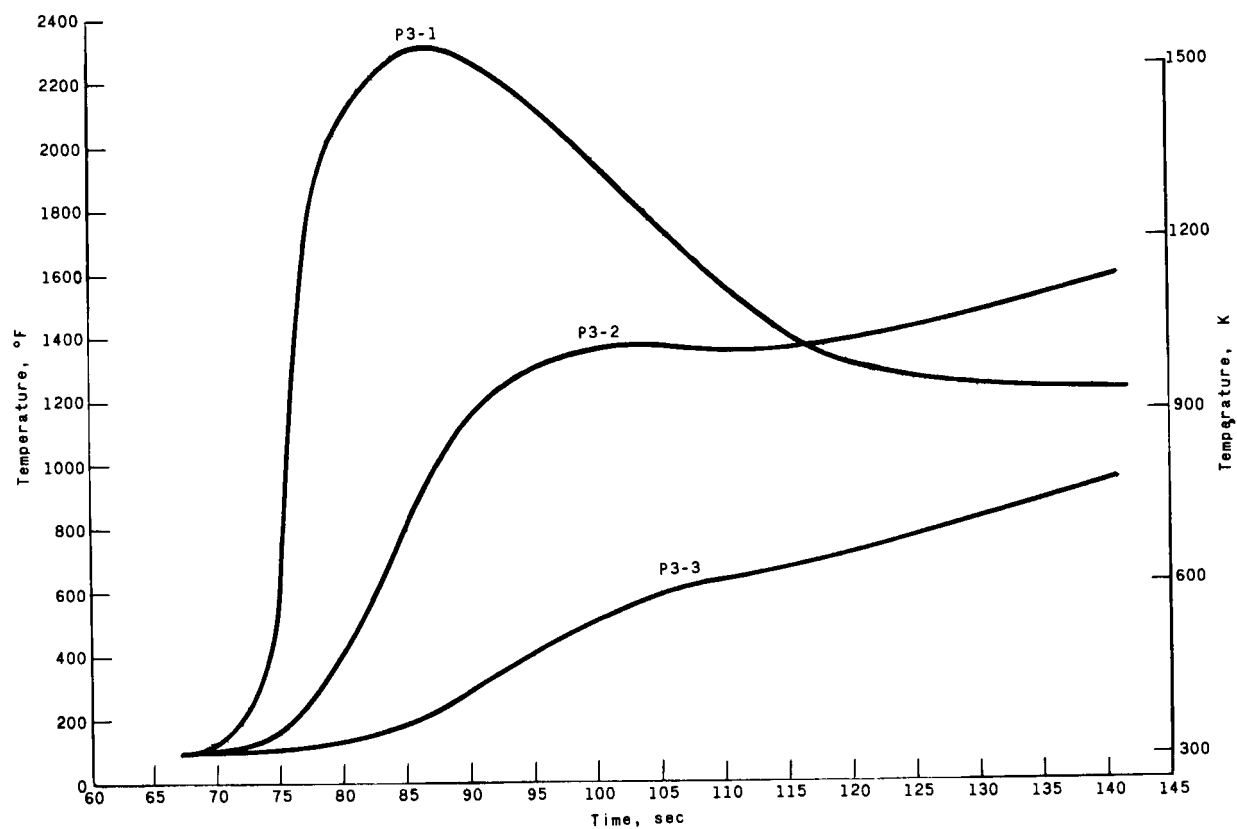
(a) Stagnation point.

Figure 22. - Hand-faired temperature histories obtained from in-depth thermocouples.



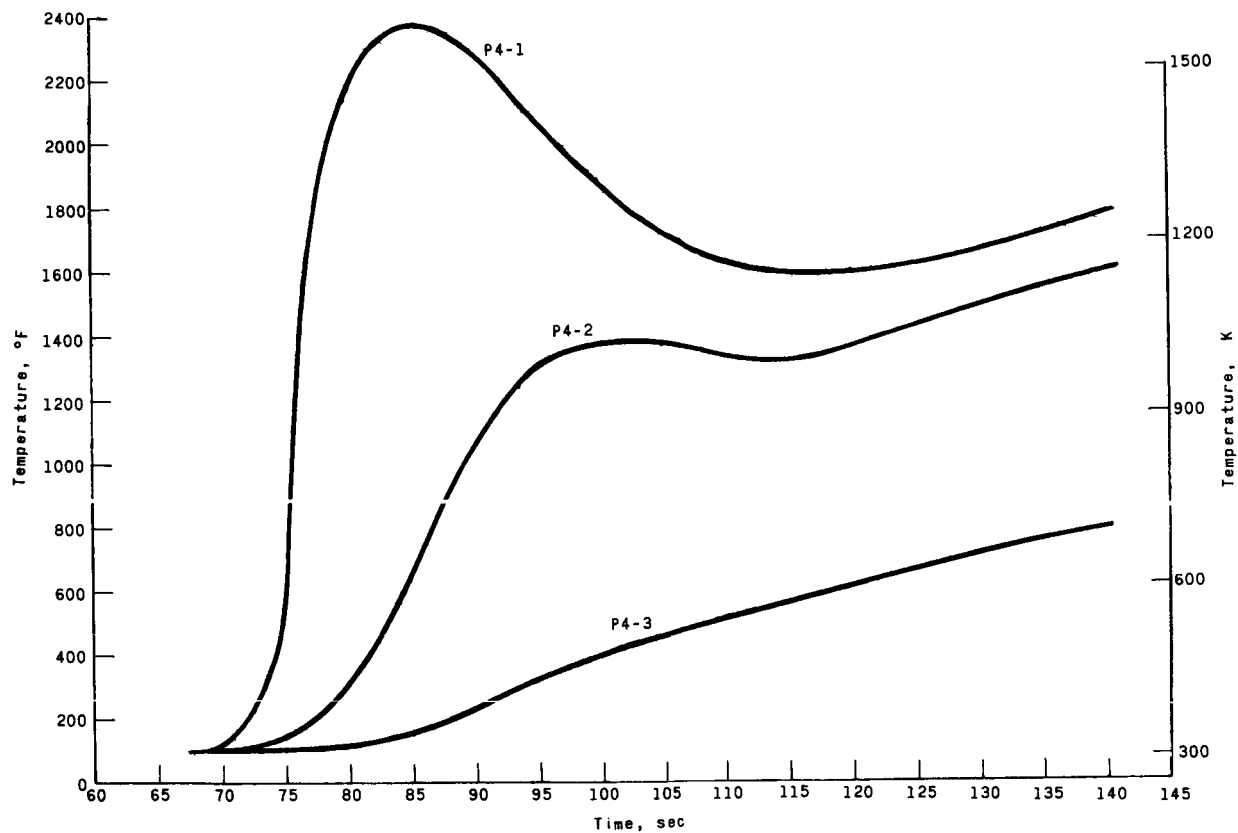
(b) Station 45°.

Figure 22.- Continued.



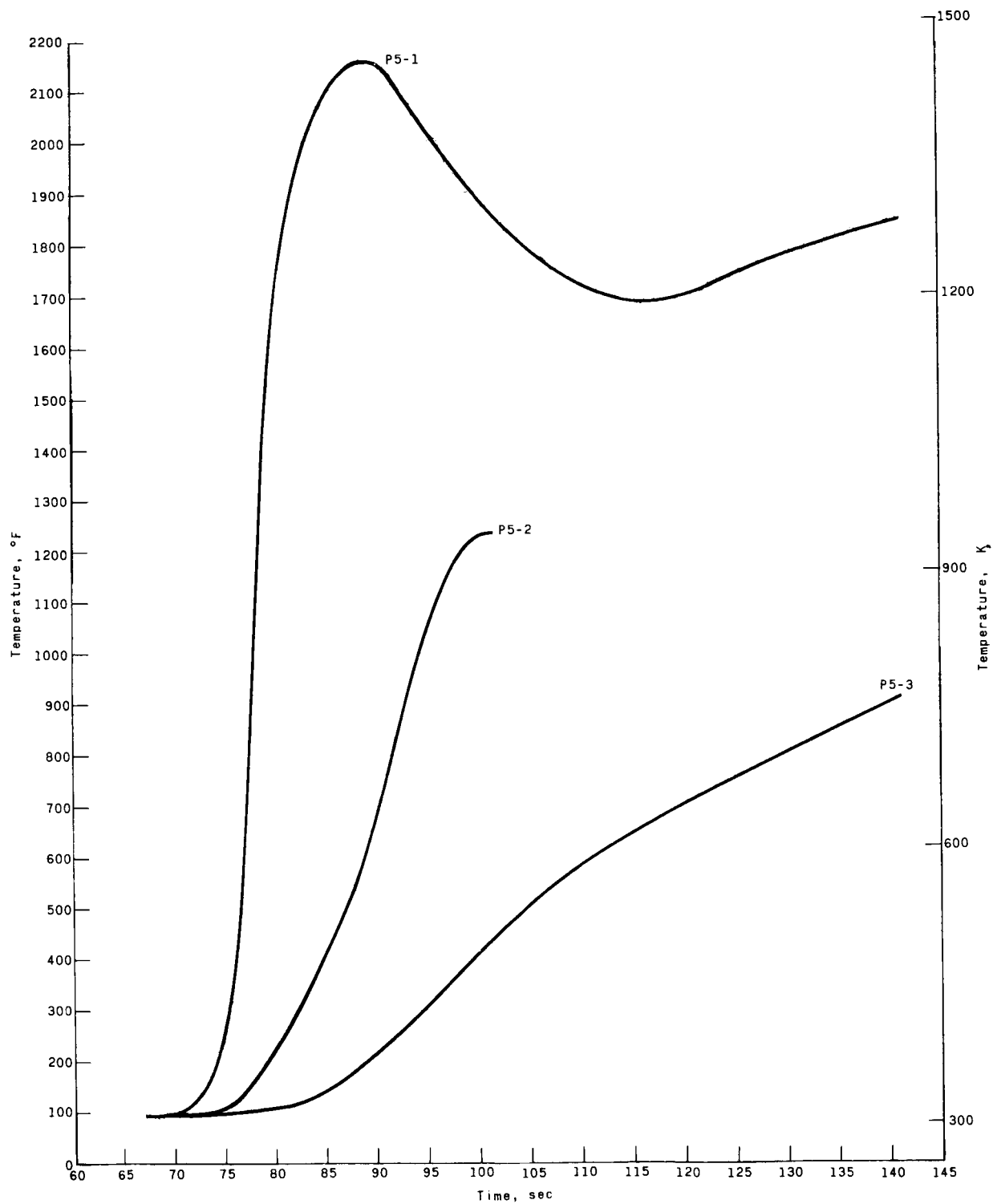
(c) Station C-C.

Figure 22. - Continued.



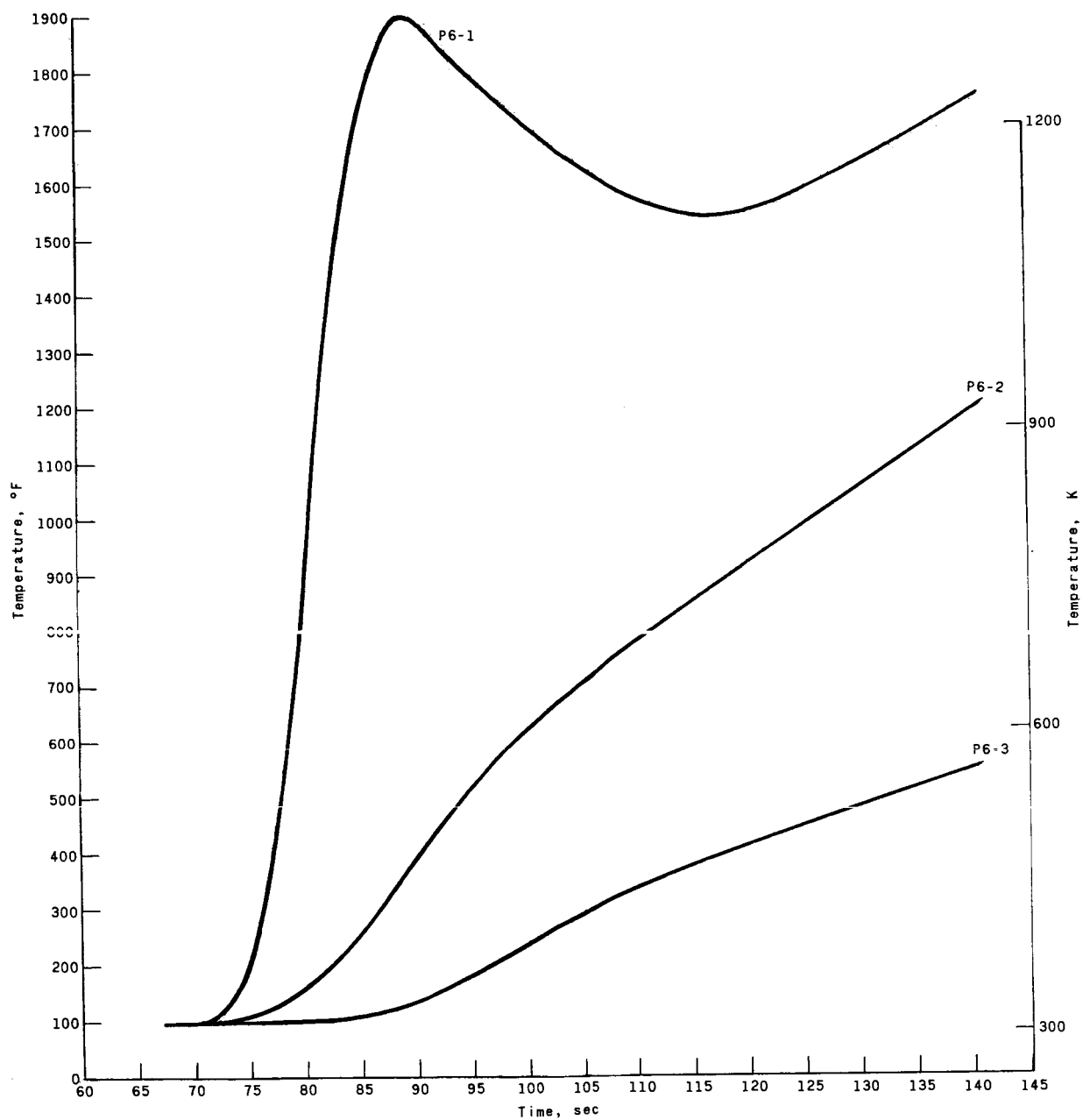
(d) Station C-C.

Figure 22.- Continued.

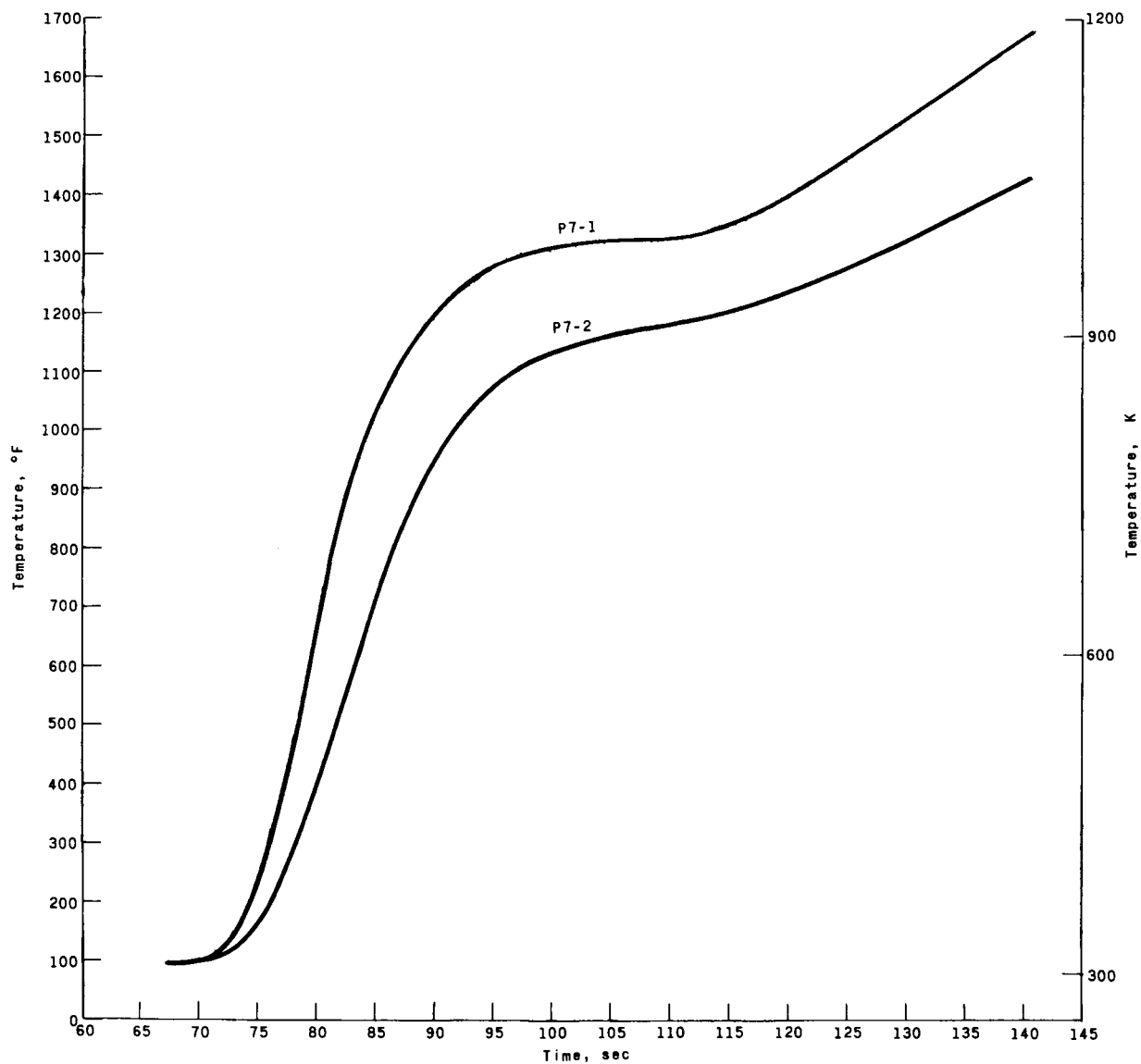


(e) Station C-C.

Figure 22. - Continued.

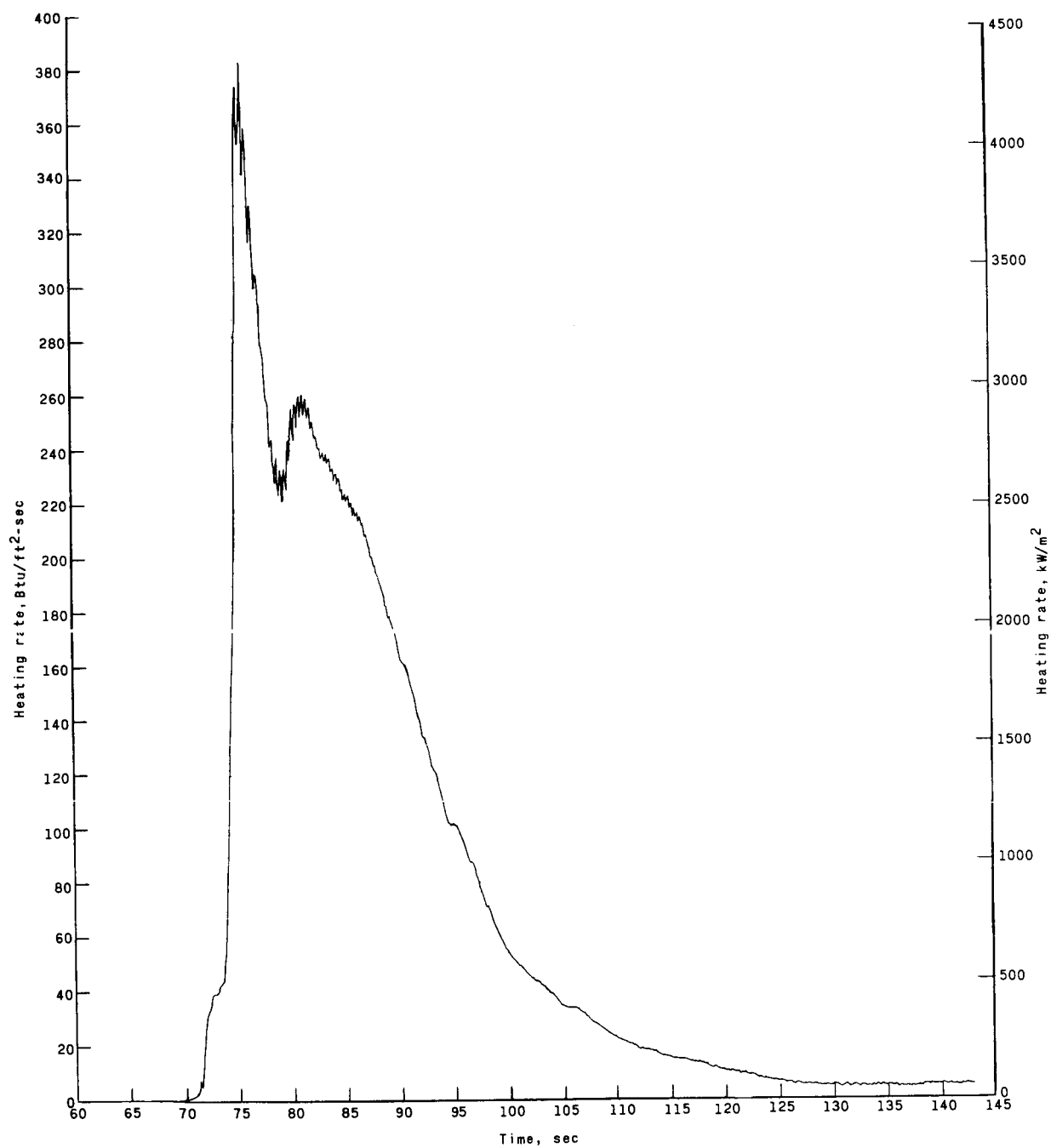


(f) Station C-C.
Figure 22. - Continued.



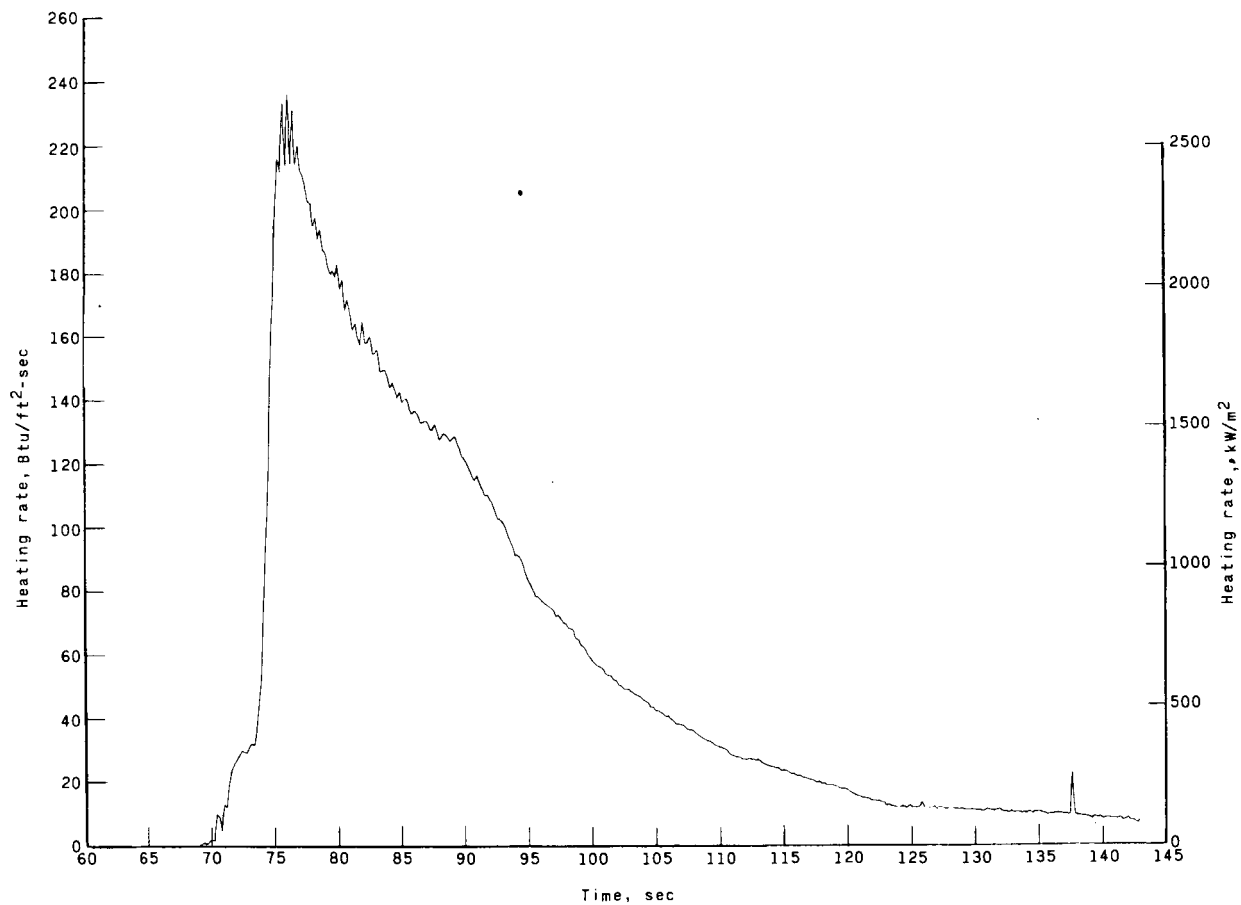
(g) Station E-E.

Figure 22. - Concluded.



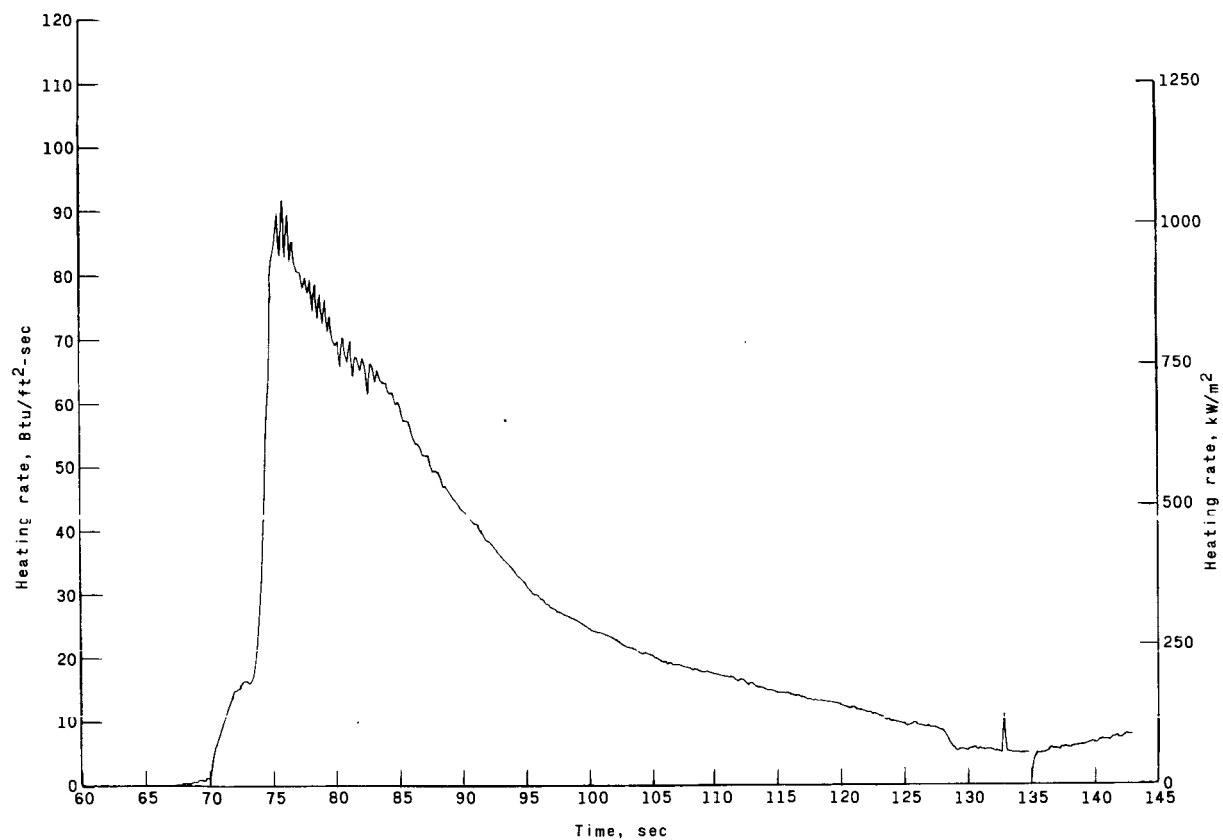
(a) Calorimeter C1 at station B-B.

Figure 23.- Measured heating-rate histories from calorimeters.



(b) Calorimeter C2 at station D-D.

Figure 23. - Continued.



(c) Calorimeter C3 at station F-F.

Figure 23. - Concluded.

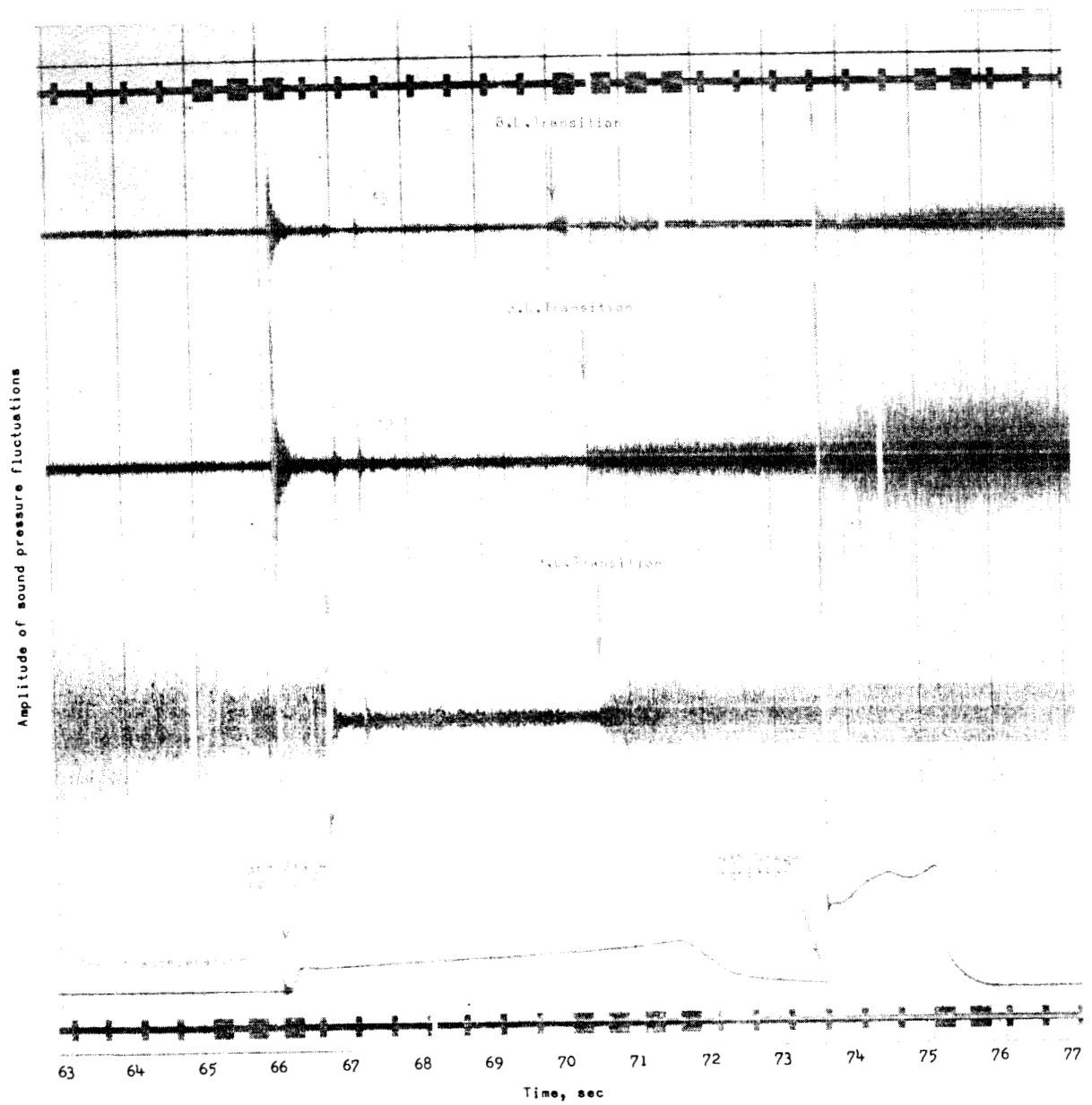
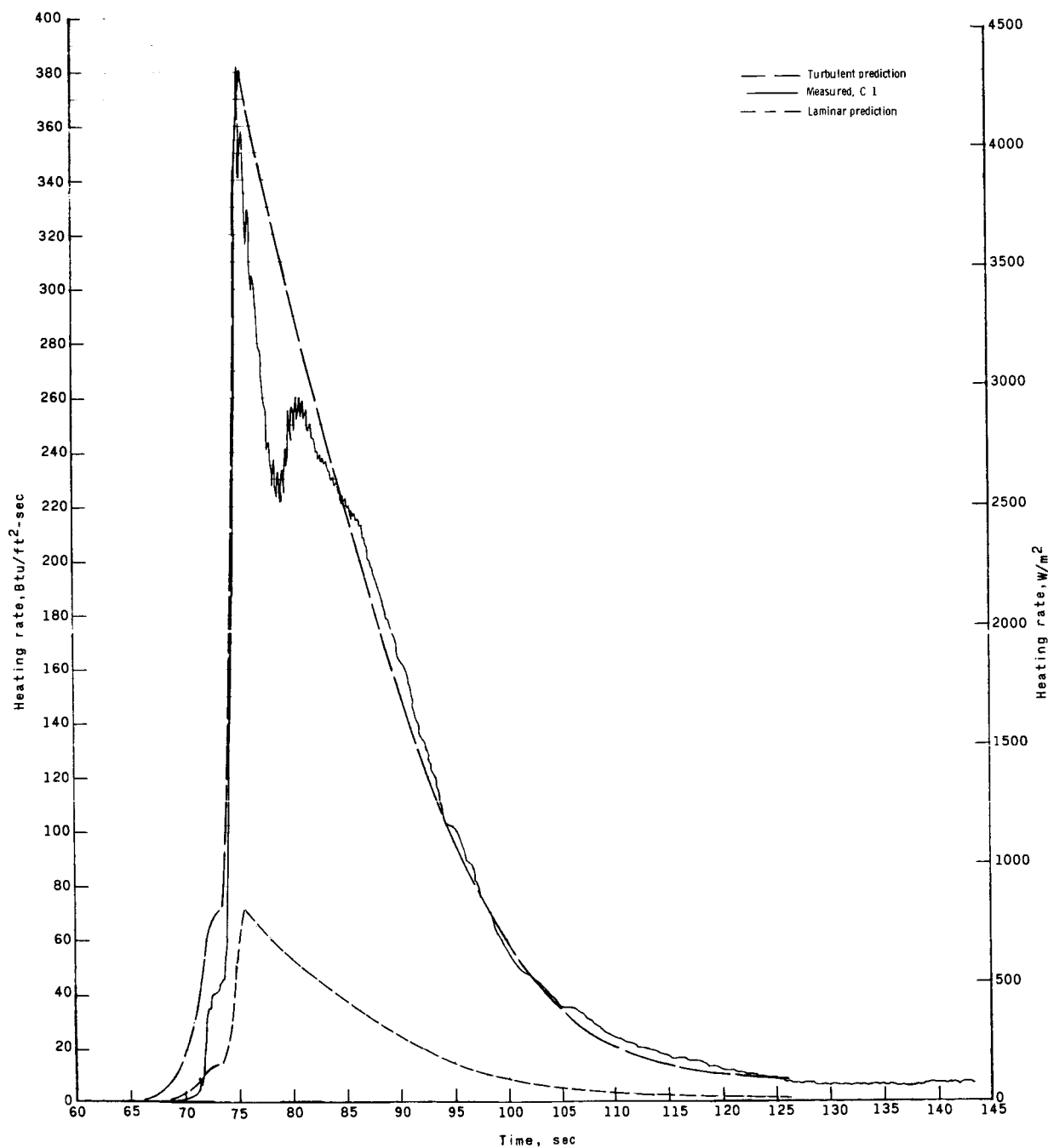
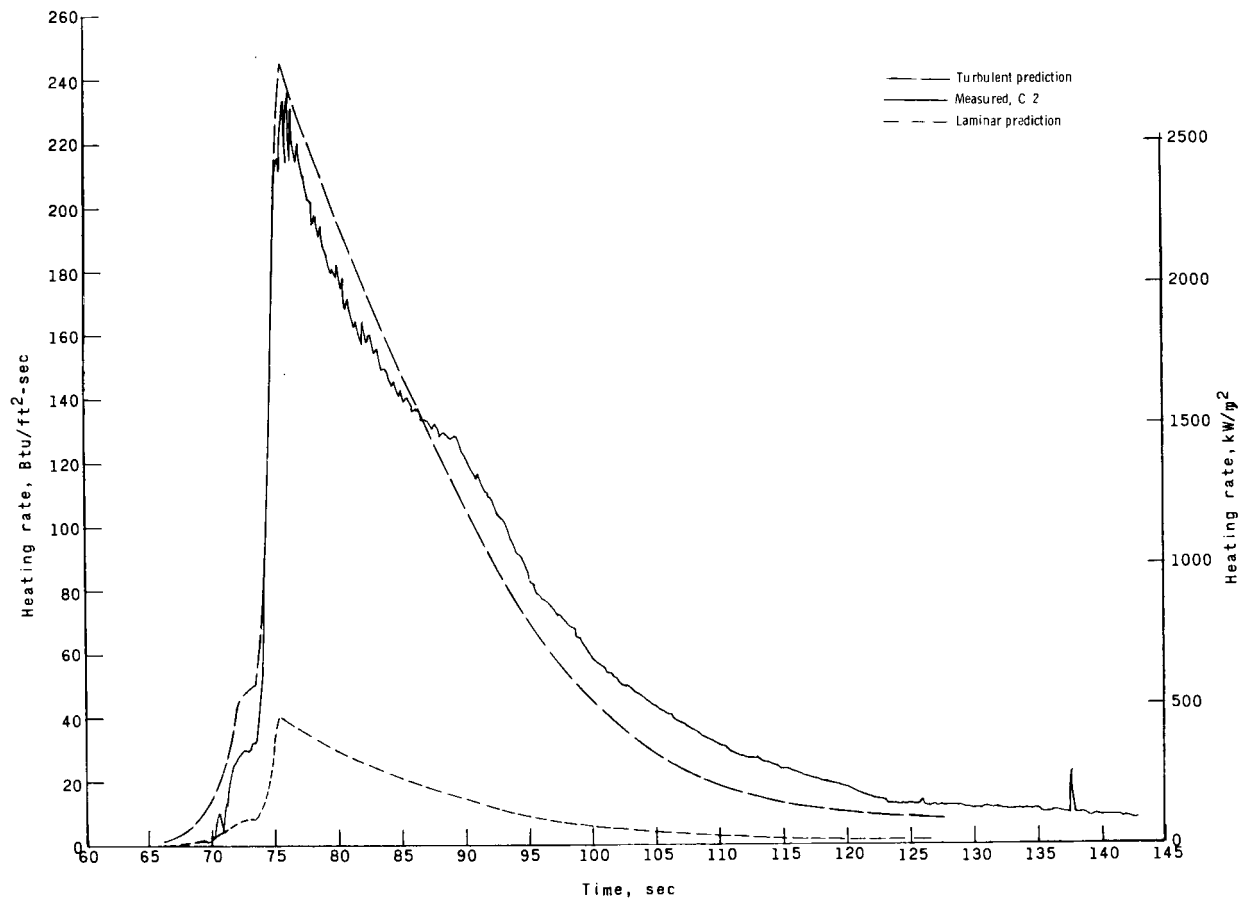


Figure 24.- Time histories of the boundary-layer (B.L.) sound-pressure fluctuations.



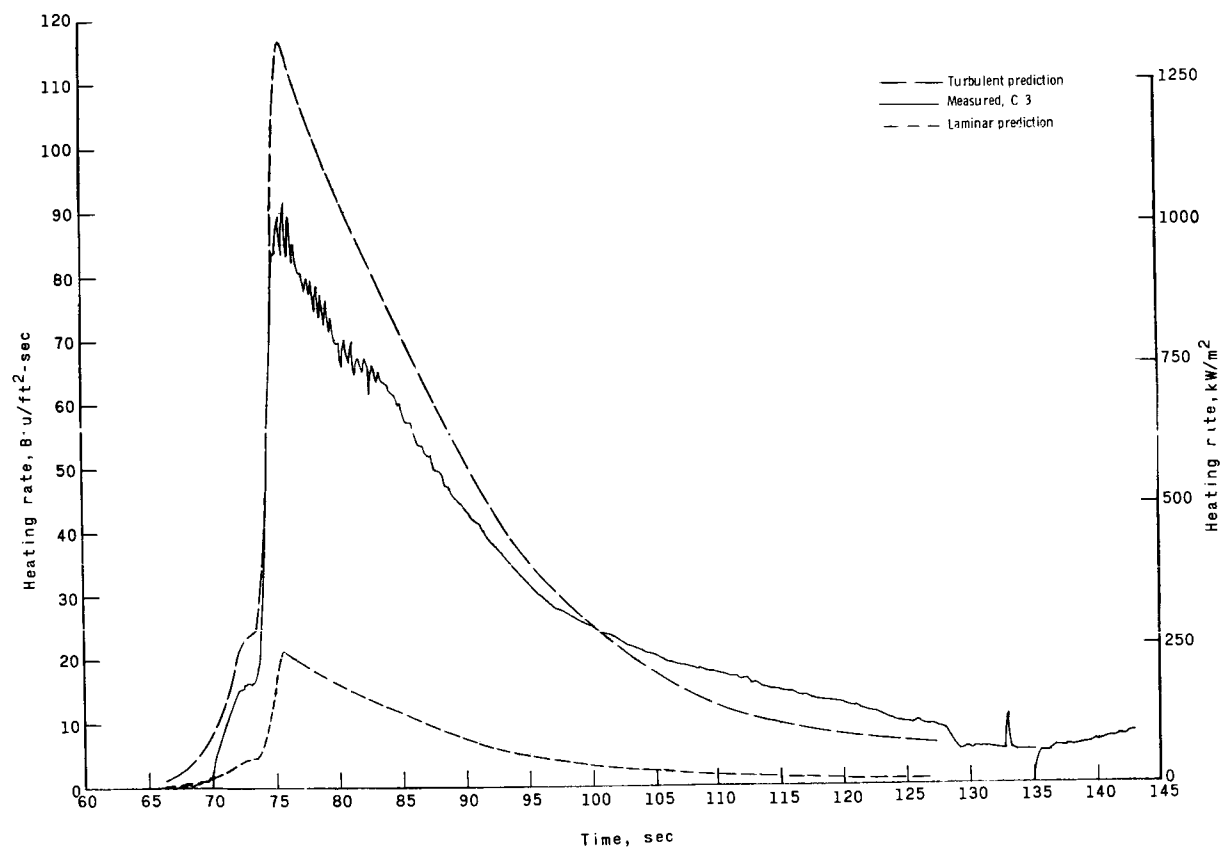
(a) Station B-B.

Figure 25.- Comparison of measured and computed heating rates.



(b) Station D-D.

Figure 25.- Continued.



(c) Station F-F.

Figure 25.- Concluded.

